Computational Thermodynamic and Kinetic Modeling and Characterization of Phase Transformations in Rapidly Solidified Aluminum Alloy Powders

A Dissertation

Submitted to the Faculty

of the

Worcester Polytechnic Institute

in partial fulfillment of the requirements for the

Degree of Doctor of Philosophy

in

Materials Science and Engineering

By

Kyle Tsaknopoulos

Kyle Tsaknopoulos

April 2019

Approved by

Professor Danielle L. Cote, Advisor

RD Sisson Jr

Professor Richard D. Sisson Jr., Department Head Materials Science and Engineering

Computational Thermodynamic and Kinetic Modeling and Characterization of Phase Transformations in Rapidly Solidified Aluminum Alloy Powders

---

Kyle Tsaknopoulos
Advisor: Danielle Cote
Committee Members: Richard Sisson, Adam Powell, Yu Zhong, Mei Yang, Victor Champagne

1 Table of Contents

2 Abstract

Cold Spray is a solid-state additive manufacturing process that uses metallic feedstock powders to create layers on a substrate through plastic deformation. This process can be used for the repair of mechanical parts in the aerospace industry as well as for structural applications. Aluminum alloy powders, including Al 6061, 7075, 2024, and 5056, are typically used in this process as feedstock material. Since this process takes place all in the solid state, the properties and microstructure of the initial feedstock powder directly influence the properties of the final consolidated Cold Spray part. Given this, it is important to fully understand the internal powder microstructure, specifically the secondary phases as a function of thermal treatment. This work focuses on the understanding of the internal microstructure of Al 6061, 7075, 2024, and 5056 through the use of light microscopy, scanning electron microscopy, transmission electron microscopy, energy dispersive x-ray spectroscopy, electron backscatter diffraction, and differential scanning calorimetry. Thermodynamic models were used to predict the phase stability in these powders and were calibrated using the experimental results to give a more complete understanding of the phase transformations during thermal processing.

3 Introduction

3.1 Motivation

This work is funded by the Army Research Lab and studies ways to improve the capabilities of both the individual soldier and battle readiness as a whole. One way that improvements are being made is through the use of additive manufacturing for repair or replacement of critical mechanical components of army transportation vehicles. The use of additive manufacturing can reduce the time for creation of new parts as the additive system could be used in the field. One such additive manufacturing system is Cold Spray, a solid state additive manufacturing process that uses metallic feedstock powder for repair and creation of vehicle parts. For example, this process can be used to repair helicopter gear box housings, which would typically make months to get repaired or replaced after being sent back from the field. With the use of an onsite cold spray unit, this repair time can be decreased to a few days. This would ensure that the soldiers can now use this downed helicopter much faster, and will ultimately save money and keep everyone safe[1,2].

Cold spray takes the metallic feedstock and is fed into a powder feeder which sends it through an inert heated gas stream that is below the melting temperature of the alloy [3]. This mixture of gas and powder if few through a converging-diverging nozzle at supersonic velocities and directed towards a substrate. At theses velocities, the powder hits the substrate and plastically deforms, adhering to the substrate. As this process continues, a layer of deformed powder is created, which can be used as either a coating at small thicknesses, or used as a bulk material when many layers are allowed to build up on the surface [3].

In order for this process to be even quicker, metal alloys that are already approved by the US Army are used to create the feedstock powder for these systems. This work focuses on the use of aluminum alloy powders, specifically 6061, 2024, 7075 and 5056. Since cold spray is a solid state additive process, the feedstock powders are not melting upon consolidation. This is unique when compared to other additive processes because the lack of melting means that the mechanical properties of the feedstock powder will directly influence the mechanical properties of the consolidated parts [3-6]. Literature has shown that parts that are deposited in a solid state from these powders can also have higher strength than their bulk counterparts [7]. Given this, it is important to understand and control the properties and microstructure of these powder in order to create the best possible cold spray layers.

3.2 Background

Aluminum alloys are divided into two classifications, wrought and cast. The chemical compositions of the powder used in this work fall under that wrought composition naming scheme. These wrought alloys use a four digit naming system. This work focuses on alloys in the 2xxx series, 5xxx series, 6xxx series, and 7xxx series [8]. These aluminum alloys have traditionally been used for many aerospace applications due to the significant difference in density when compared to that of steels [9].

For the 2xxx series alloys, copper is always the main alloying element, sometimes with significant use of magnesium. The alloy in this study, aluminum 2024, is an age-hardenable alloy that is widely used in the aircraft and aerospace industries for wrought components, coatings, and repair applications [10]. Many secondary phases can be seen in wrought and cast 2024 including: Al_7Cu_2Fe, $Al_{12}(Fe,Mn)_3Si$, Al_2CuMg, Al_2Cu, $Al_6(Fe,Cu)$, where the primary strengthening phases of 2024 are the S (orthorhombic Al_2CuMg) and θ (tetragonal Al_2Cu) phases [11,12],

In the 6xxx series, magnesium and silicon are the most abundant alloying elements. The alloy in this study is 6061, which is also an age-hardenable alloy. The observed constituent phases include Mg_2Si, $Al_{12}(Fe,Mn)_3Si$ [11]. The primary strengthening sequence is $\beta'' \rightarrow \beta' \rightarrow \beta$ (Mg_2Si), moving from needles, to rods, to equilibrium plates or cubes during treatment, respectively, where β'' is the primary strengthening phase [13,14].

The 7xxx series, zinc is the primary alloying element. The composition 7075 is used
Phases Al_7Cu_2Fe, $Al_{12}(Fe,Mn)_3Si$, $Al_6(Fe,Mn)$, Mg_2Si. $MgZn_2$ or η and its metastables are the primary phase in this alloy, where the η' phase contributes significantly to the strength of the alloy [11].

The last alloy series used is the 5xxx series, with a main alloying element of magnesium. This alloy is not age-hardenable due to the phase solubilities with the given composition. This work studies 5056, where the β phase (Al_3Mg_2) can be seen, but unlike the other heat treatable alloys, this primary phase does not contribute to the strength of the alloy [11].

For use in solid state additive manufacturing, such as cold spray, feedstock powder of the traditional alloying compositions mentioned above are created through gas atomization. During this process, the molten alloy is atomized using a gas stream and the produced droplets subsequently undergo rapid cooling, resulting in powder particles with an as-cast dendritic microstructure that inherently contain segregation of alloying elements. The processing parameters also affect the morphology of the resulting particles, all of which are primarily spherical, though the mixture contains a wide size distribution [15].

Since these powders are created using gas atomization, the metal undergoes very high cooling rates, which are classified under rapid solidification. Given this, it is expected that there will be non-equilibrium phases present in the as-atomized powders, which will differ from conventional cast or wrought aluminum [16].

A deeper understanding of the potentially different phases present in these aluminum alloy powders can be revealed using commercially available computation thermodynamic and kinetic software, such as Thermo-Calc. This software was initially created in the 1970s by Professor Mats Hillert and his graduate students; Bo Sundman, Bo Jansson, and John Ågren in the Division of Physical Metallurgy at the Royal Institute of Technology in Stockholm, Sweden. All three students needed access to thermodynamic data for their research, and when that was not available, they decided to create a software for thermodynamic calculations that could be used for many different alloy systems. Others who made early contributions to this software include: Lars Höglund, Jan-Olof Andersson, Bjorn Jönsson and Anders Engström [17].

In 1985, Sundman et al. released a paper about the capabilities of this new Thermo-Calc software. In the metallurgy industry, alloys with many different components are used, and it is important to understand the equilibrium states of these alloys for various processing procedures. Unfortunately, with a large number of components in the alloy, the experimental work to get this information is very challenging. This software predicts equilibrium states using a databank of binary or ternary data to allow for computer extrapolation in multi component systems [18]. Thermo-Calc was intended to be an all-encompassing software to calculate thermochemical systems that was easy to use for engineers in many industries. Thermo-Calc uses the CALPHAD method, or calculation of phase diagram, to extrapolate based upon the available thermodynamic experimental data from literature to calculate thermodynamic properties with limited data. This software is unique due to the rigorous data assessment and that is used to create the databank that gives such accurate results. This data is collected as part of international collaboration to ensure the best caliber data available through previous experiments.

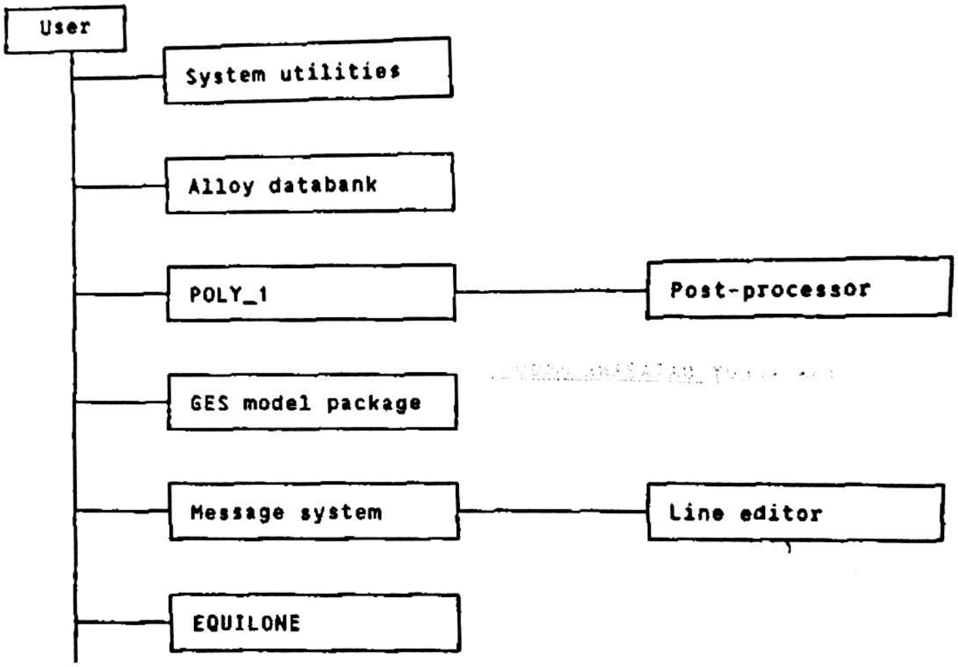

FIG. 4. The modular structure of Thermo-Calc. The postprocessor and the lined modules are local to the POLY_1 and MESSAGE module respectivly.

Figure 1: Structure of Thermo-Calc Modules as shown in the first Thermo-Calc paper from 1985 [18]

The Thermo-Calc software is broken down into modules and accessed through a command line. The different modules are found in Figure 1 above. The System utilities module is the first step to running a simulation and allows the user to set many global variables for their particular problem. The paper describes all the commands available from this starting module and beyond, including how to get help inside the software. In the Alloy databank module, the user defines the alloy system they are interested in including composition of the alloy and phases to be integrated into the calculations. After the system is defined, the user tells the software to collect the relevant thermodynamic data from the databank. The module for phase diagram calculations, or Poly_1, is where the user sets the simulation conditions for calculating an equilibrium diagram. The Post-processor module allows the use to plot and tabulate the calculated data into a useful format. The thermodynamic module, or GES (Gibbs Energy System) model, allows the user to amend the previously calculated data. The messages module allows for the user to communicate with the software creation team about any problems you are having with the software [18].

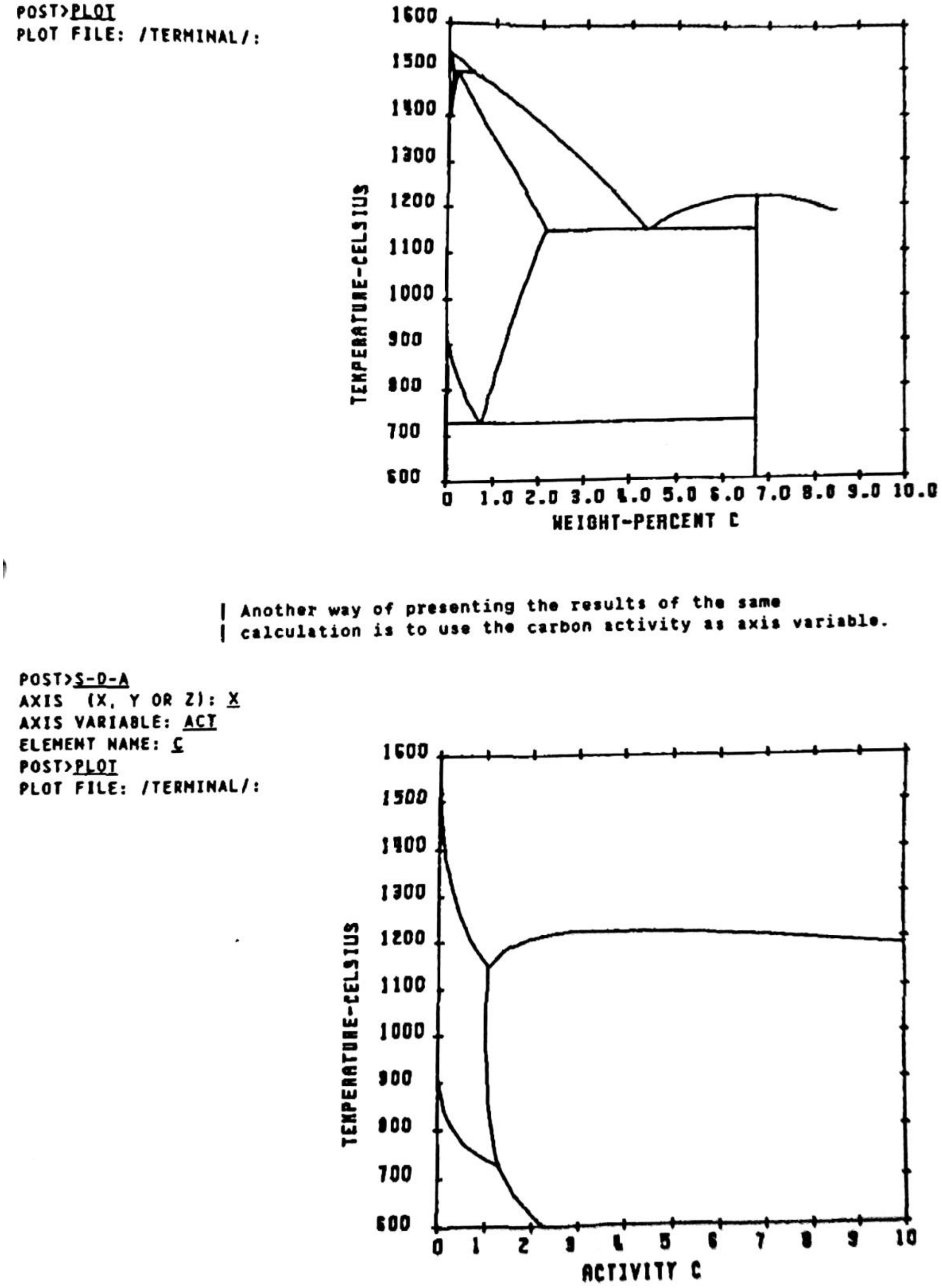

```
POST>PLOT
PLOT FILE: /TERMINAL/:
```

```
| Another way of presenting the results of the same
| calculation is to use the carbon activity as axis variable.

POST>S-D-A
AXIS  (X, Y OR Z): X
AXIS VARIABLE: ACT
ELEMENT NAME: C
POST>PLOT
PLOT FILE: /TERMINAL/:
```

Figure 2: Examples of Thermo-Calc Phase Diagram Outputs as shown in the first Thermo-Calc paper from 1985 [18]

Sundman et al. then described two examples of how a researcher could use the Thermo-Calc software and the exact commands that are to be used to accomplish the task. The first example uses a binary Fe-C system that would be useful for a steel researcher. The commands are presented to create a phase diagram as well as an activity diagram for the Fe-C system and the output is shown in Figure 2. The second example demonstrated how Thermo-Calc handles a more complicated system, a steel containing C, Si, Mn, Cr, Mo, W and V.

The work of one of the original graduate students, John Ågren, on diffusion controlled transformations led to the creation of DICTRA, the diffusion module in the Thermo-Calc software [17]. In 1982, Ågren published work on a numerical treatment of diffusional reactions in alloy systems [19]. This work first described the basic equations for the numerical methods he later used in computer simulations to begin the creation of DICTRA. The base equations form a system of equations that satisfy both conservation of mass and equilibrium. The following equation represents the composition of phase α:

$$\sum_k y_k^{s\alpha} = 1 \tag{1}$$

where, k is all components on s, the sublattice. Next the α/β interface equilibrium is described, where β is the dissolving phase. If both α and β have a sublattice, it results in the following equilibrium:

$$G_i^\alpha - G_{js}^\alpha = G_i^\beta - G_{js}^\beta \tag{2}$$

where js is the reference components in the sublattice. G_i^α is the partial Gibbs energy for component *i* in the alpha phase. Equation (1) becomes:

$$\frac{\partial G_m^\alpha}{\partial y_i^s} - \frac{\partial G_m^\alpha}{\partial y_{js}^s} = \frac{\partial G_m^\beta}{\partial y_i^t} - \frac{\partial G_m^\beta}{\partial y_{js}^t} \tag{3}$$

When components i and j are in the same sublattice, and must be the case for all components. G_m^α is the molar Gibbs energy of the phase α. When β is the reference phase:

$$G_m^\alpha + \sum_{si}\sum (\delta_{ijs} - y_i^s)\frac{\partial G_m^\alpha}{\partial y_i^s} = \sum_s a^s\, G_{js}^\beta \tag{4}$$

where a^s is the number of atoms on the sublattice per formula unit of the phase α. A mass balance at the α/β interface gives:

$$\frac{\upsilon^\alpha}{V_m^\alpha}\sum_s a^{s\alpha}\, y_k^{s\alpha} - \frac{\upsilon^\beta}{V_m^\beta}\sum_t a^{t\beta}\, y_k^{t\beta} = \sum_s J_k^{s\alpha} - \sum_t J_k^{t\beta} \tag{5}$$

where υ is a growth rate of a phase, and J is a diffusional flux of a component. When each component only dissolves in one sublattice Equation (5) becomes:

$$\frac{\upsilon^\alpha}{V_m^\alpha} a^{s\alpha} y_k^{s\alpha} - \frac{\upsilon^\beta}{V_m^\beta} a^{t\beta} y_k^{t\beta} = J_k^{s\alpha} - J_k^{t\beta} \tag{6}$$

When molar volume V_m is assumed constant:

$$J_k^s = -\sum_{ti}\sum D_{ki}^{st}\frac{a^t}{V_m}\nabla y_i^t \tag{7}$$

When combined, equations 6 and 7 become:

(8)

$$\frac{a^s}{V_m}\frac{\partial y_k^s}{\partial t} = -\frac{1}{x^m}\frac{\partial}{\partial x}(x^m J_k^s)$$

where m is an integer that signifies the geometry of the phase: planar, cylindrical, or spherical. Ågren then applied a numerical method that followed these base calculations. These numerical calculations follow the Galerkin method for finite element analysis, and were later used in the computer program that would become DICTRA [19]. From Equation (8, several functions were applied to arrive at:

$$\frac{a^s}{V_m}\sum_{i=1}^{n}\frac{\partial y_{ki}^s}{\partial t}\int_{x_1}^{x_n} x_m\, \Phi_i \Phi_j dx = -\{x_n^m J_k^{sn}\, \Phi_j(x_n) - x_1^m J_k^{s1}\, \Phi_j(x_1)\} + \int_{x_1}^{x_n} x_m\, J_k^s \frac{\partial \Phi}{\partial x} \quad (9)$$

Equation (9 is the general case and becomes a system of ordinary differential equations. It can then be applied to the diffusion problem to yield a final equation:

$$\left(\frac{a}{V_m}A - \frac{\Delta t}{2}B_k^s\right)Y_k^s(t+\Delta t) = \frac{\Delta t}{2}\big(R(t+\Delta t) + R(t)\big) + \Delta t\sum_{t=1}^{L}\sum_{l=1}^{n_t} C_{lk}^{ts}\, Y_l^t(t) + \left(\frac{a^s}{V_m}A + \frac{\Delta t}{2}B_k^s\right)Y_k^s \quad (10)$$

where R is a vector encompassing the boundary conditions, and A, B_k^s, and C_{lk}^{ts} are matrices. This equation coupled with Equations (1(6 can be solved simultaneously to yield the numerical calculation of a diffusion problem [19].

Later in 1990, Andersson et al. released a paper with an initial introduction to the new software DICTRA [20]. The paper described that DICTRA had been integrated into the Thermo-Calc system and could solve systems of diffusion equations to investigate a moving interface. They stressed the importance of the software's use for practical engineering problems with many components, rather than simple problems that cannot be used for scale up. The paper emphasized that the work from Ågren described above [19], was the first of its kind to combine numerical models for diffusion with thermodynamic data calculations. This paper by Andersson et al., is the first to demonstrate DICTRA's usefulness to practical applications and agreement with models and experimental results through several examples including dissolution of cementite in an Fe-Cr-C system. The experiments and computation yielded results demonstrating that there was good correlation between the two data sets [20]. The models described in this paper paved the way for more advances in both the software and the capabilities for more practical problems through additional developments in the thermodynamic and kinetic databases.

These models can be used in conjunction with experimental observations in order to gain a more complete understanding of the internal microstructure of aluminum alloy powders.

3.3 Dissertation Layout

This document contains seven chapters. Chapter 4 contains an investigation into the chemical segregation suspected to be present at the grain boundaries of as-atomized aluminum alloy powder particles, which lead to the development of the four subsequent chapters. Chapter 5 includes analysis of aluminum alloy 2024 powder and the evolution of the internal microstructure as a function of thermal treatment. Chapters 6 and 7 explore the identification of secondary phases in aluminum 6061 powder for both the as-atomized and thermally treated conditions. Chapter 6 focuses on the identification of Mg-rich phases, while Chapter 7 focuses on the Fe-rich phases present in the microstructure. Chapter 8 includes an investigation of the phase transformations of aluminum alloy 7075 powder while Chapter 9 includes a similar investigation into the phase transformations in aluminum alloy 5056 powders. Chapters 5-9 all use computational modeling to guide the experimental process. Chapter 10 explores the dissolution and growth of secondary phases with the use of diffusional modeling to further understand the phase transformations seen in these alloys through thermal treatments.

3.4 References

1. Belsito, D. L. (2014). Application of Computational Thermodynamic and Solidification Kinetics to Cold Sprayable Powder Alloy Design. Retrieved from https://digitalcommons.wpi.edu/etd-dissertations/28
2. D. Belsito, B. McNally, L. Bassett, V. Champagne, Jr., R.D. Sisson, Jr., “Through-process Modeling for Cold Spray Alloy Optimization,” Proceedings MS&T 2013, Montreal, Quebec, Canada.
3. Champagne, V. K. *The cold spray materials deposition process : fundamentals and applications*. (Woodhead, 2007). p. 1
4. Rokni, M. R., Widener, C. A., Champagne, V. K., Crawford, G. A., & Nutt, S. R. (2017). The effects of heat treatment on 7075 Al cold spray deposits. *Surface and Coatings Technology*, *310*, 278-285.
5. Rokni, M. R., Nutt, S. R., Widener, C. A., Champagne, V. K., & Hrabe, R. H. (2017). Review of relationship between particle deformation, coating microstructure, and properties in high-pressure cold spray. *Journal of thermal spray technology*, *26*(6), 1308-1355.
6. Rokni, M. R., Widener, C. A., Champagne, V. K., & Crawford, G. A. (2015). Microstructure and mechanical properties of cold sprayed 7075 deposition during non-isothermal annealing. *Surface and Coatings Technology*, *276*, 305-315.
7. P. D. Eason, J. A. Fewkes, S. C. Kennett, T. J. Eden, K. Tello, M. J. Kaufman and M. Tiryakioğlu, *Mater. Sci. Eng., A*, 528, 8174 (2011)
8. E.L. Rooy, Introduction to Aluminum and Aluminum Alloys, *Properties and Selection: Nonferrous Alloys and Special-Purpose Materials*, Vol 2, *ASM Handbook*, ASM International, 1990, p 3–14
9. G.E. Totten, Hardening, Annealing, and Aging, *Handbook of Aluminum: Vol. 1: Physical Metallurgy and Processes*. (CRC Press, 2003), p. 1-31
10. V. Champagne and D. Helfritch, *Mater. Sci. Technol.*, 31, 627 (2015)
11. G.E. Totten, Hardening, Annealing, and Aging, *Handbook of Aluminum: Vol. 1: Physical Metallurgy and Processes*. (CRC Press, 2003), p. 123-195.

12. C. Badini, F. Marino and E. Verné, *Mater. Sci. Eng., A*, 191, 185 (1995)
13. Chakrabarti, D. . & Laughlin, D. E. *Prog. Mater. Sci.,* 49, 389 (2004).
14. Matsuda, K. *et al. Mater. Sci. Eng. A,* 262, 232 (1999).
15. E. J. Lavernia, J. Ayers and T. S. Srivatsan, *Int. Mater. Rev.*, 37, 1 (1992)
16. Walde, C., Cote, D., Champagne, V. et al. J. of Materi Eng and Perform (2018). https://doi.org/10.1007/s11665-018-3550-0
17. *Thermo-Calc Software: History*. [cited 2017 10/27]; Available from: http://www.thermocalc.com/our-company/history/.
18. Sundman, B., B. Jansson, and J.-O. Andersson, *The thermo-calc databank system.* Calphad, 1985. **9**(2): p. 153-190.
19. Ågren, J., *Numerical treatment of diffusional reactions in multicomponent alloys.* Journal of Physics and Chemistry of Solids, 1982. **43**(4): p. 385-391.
20. Andersson, J.O., et al., *Fundamentals and Applications of Ternary Diffusion, ed. by GR Purdy*. 1990, Pergamon Press, New York. p. 153-163.

4 Chemical Segregation in Aluminum Alloy Powders

4.1 Modeling Homogenization of Chemical Segregation

4.1.1 Thermo-Calc Models

Computational modeling can be used to guide experimental characterization of metallic alloy systems. The Scheil solidification diagram created using Thermo-Calc, Figure 1a, is representative of rapid solidification processes, and is therefore applicable to the gas atomized powders in this study. The as-atomized powders will follow the solidification path set forth by the diagram and this has helped to guide phase identification in the powders. Figure 1b is an example of an Equilibrium diagram that shows the amounts of each phase as a function of increasing temperature. This was used to understand phase stability given each allow composition as well as how to choose a solutionization temperature while still avoiding incipient melting of the alloy. This process is further explained in Chapters 5-9. These figures were calculated in Thermo-Calc using the composition for Al 6061, which will be used for the example models in this section. The solutionization temperature chosen for this alloy was 530C, to be held for 1 hour. These diagrams were used as the first step in understanding the internal microstructure of the powers.

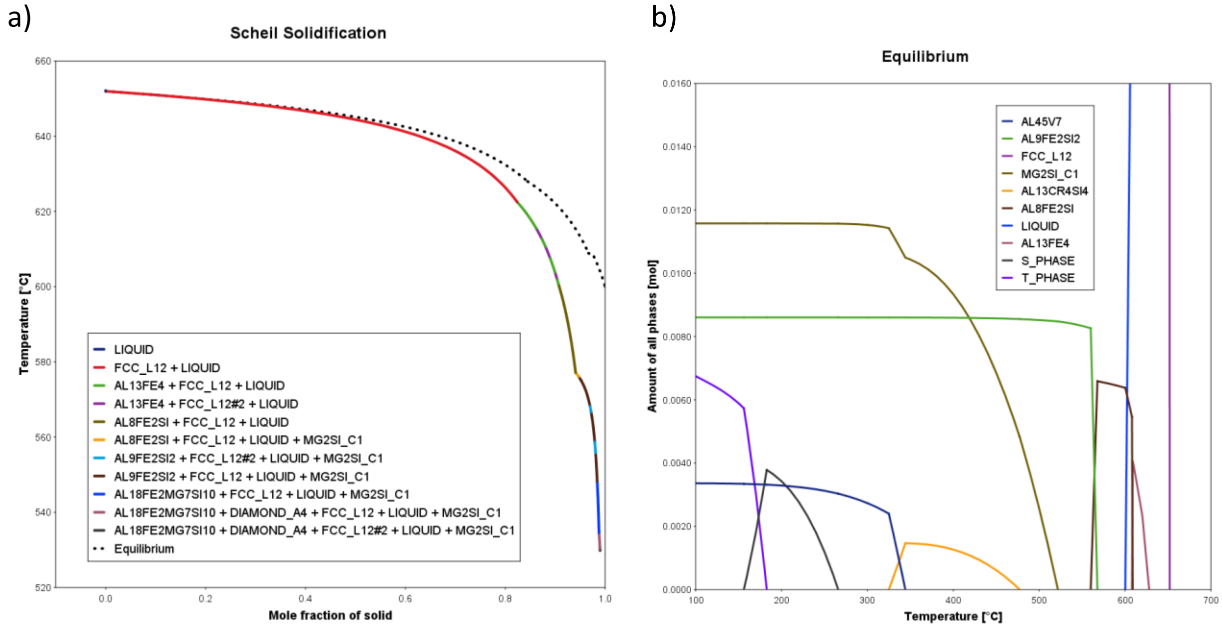

Figure 1: a) Scheil Solidification Diagram b) Equilibrium Diagram, both for Al 6061 created by Thermo-Calc.

4.1.2 DICTRA: Homogenization Model

The diffusion module of Thermo-Calc, DICTRA, was used to model the homogenization of the apparent solute segregation at the grain boundaries of a 6061 powder particle cross- section seen in Figure 2a. Figures 2b,c show the elemental EDS maps for Mg and Si, demonstrating the concentration of the alloying elements at the boundaries. The homogenization model in DICTRA is completed in two steps; the Scheil calculation, and the homogenization model. The Scheil calculation Estimates the solidification range of an alloy, assuming; the liquid is always homogeneous, the diffusivity in solid is zero and can be disregard for selected components. This model uses the thermodynamic database for aluminum (TCAL4) and includes inputs of temperature, phases present, composition of the alloy. The homogenization model simulates long-range diffusion of elements in a single region of a single phase (in the case the FCC aluminum matrix) at a given temperature assuming; multiphase mixture, local equilibrium holds at each node, and that no diffusion in Mg_2Si phase (as there is no data available in Al database). The homogenization model uses both the thermodynamic database (TCAL4) and the mobility database (MOBAL3) for calculations with inputs of phases present, simulation time, width of the region (grain size or SDAS), and temperature.

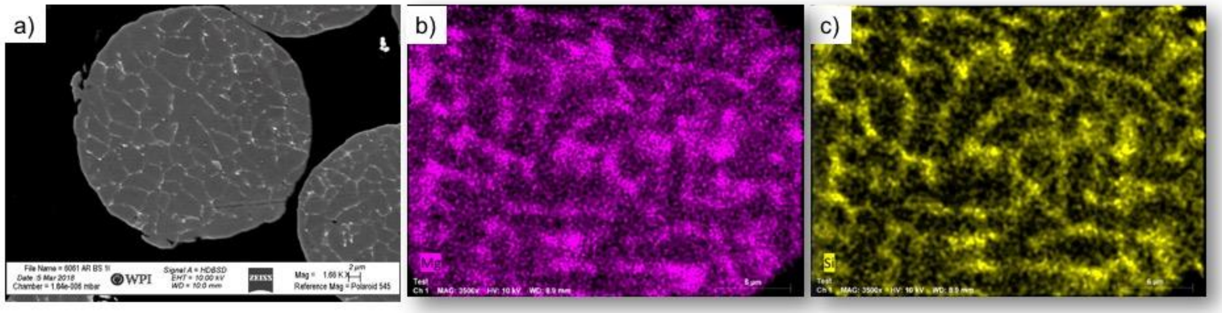

Figure 2. a. SEM BSE image of Al 6061 powder cross-section, b,c. EDS map of elemental Mg,Si respectively in Al 6061 powder particle cross-section

An example of this simulation was done for an Al 6061 powder particle. To simplify the initial calculations, the system was simplified to a ternary system, Al, Mg, Si. The initial Scheil output for this system is shown in Figure 3.

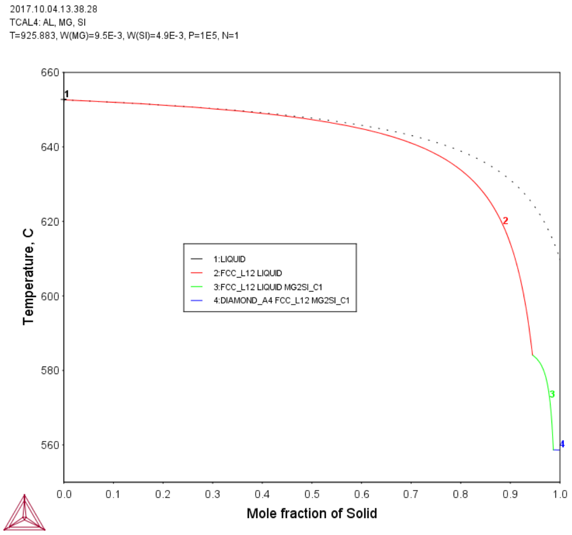

Figure 3. Scheil solidification diagram from simplified Al-Mg-Si system from Thermo-Calc.

Figures 4 and 5 show the output of the homogenization model, where the weight percent of Mg and Si respectively are shown as a function of the distance from the middle of a grain boundary (boundary shown as spike in solute concentration at 1um distance) for varying times. The model was run for constant heating at 530°C as this was chosen for the solutionization temperature for this alloy. Figure 4 shows that by 30 seconds, the solute segregation has dissolved away. To find out exactly how long this segregation takes to dissolve, Figure 5 demonstrates a shorter timeline where the solute segregation has completely dissolved after 3 seconds.

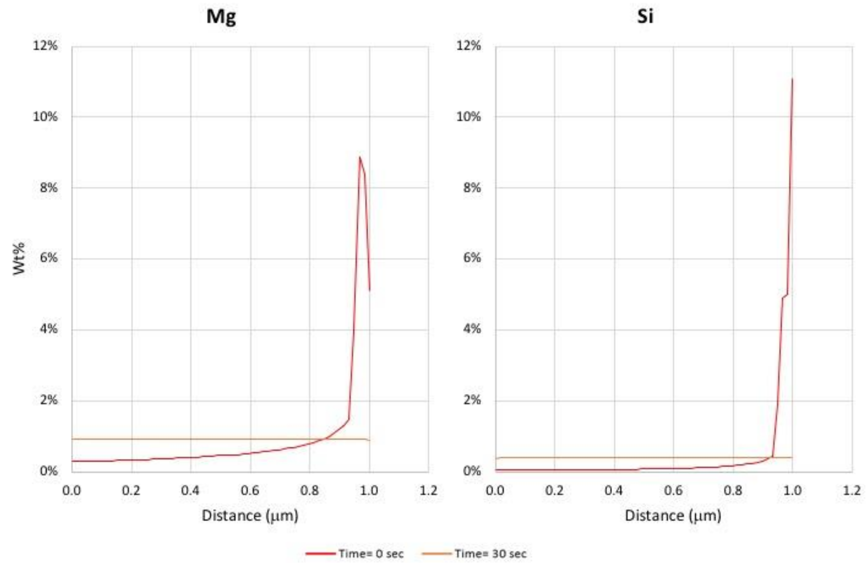

Figure 4. DICTRA Homogenization Model Output for Constant Heating at 530C for Mg and Si elemental segregatoin at a grain boundary for time 0 seconds to 30 seconds.

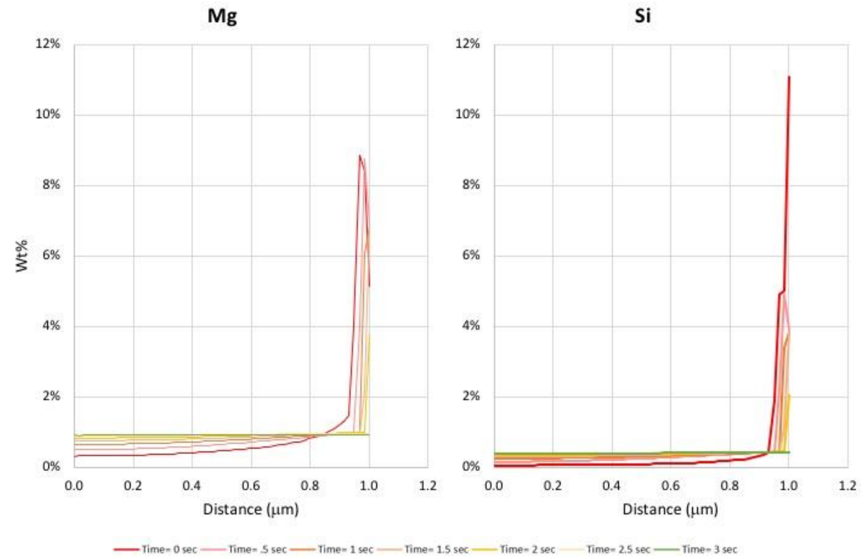

Figure 5. DICTRA Homogenization Model Output for Constant Heating at 530C for Mg and Si elemental segregatoin at a grain boundary for time 0 seconds to 3 seconds.

A second iteration of this model was completed using a heating rate of 50°C/min up to 530°C and held for 1 hour was used to mimic the heat treatment process of the experimental process, instead of using constant heating where instantaneous heating was assumed at 530°C. These results are found in Figures 6 and 7. Figure 6 shows the same weight percent of Mg and Si shown as a function of the distance from the middle of a grain boundary for times between 0 and 10 minutes. The homogenization seemed to happen quickly between 9 and 10 minutes, so Figure 7 demonstrates an increased number of time increments between those times. These figures display that the homogenization of the solute segregation at the grain boundaries should not dissolve until after 9-10 minutes has passed.

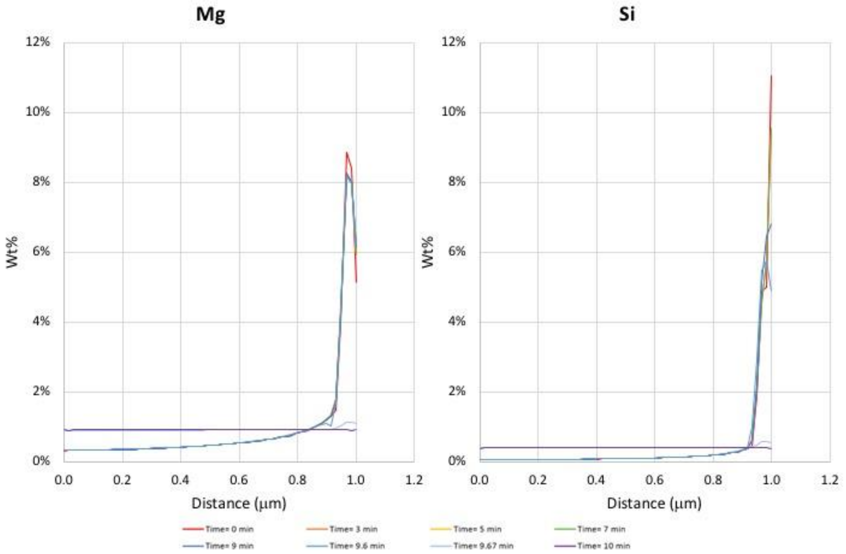

Figure 6. DICTRA Homogenization Model Output for Heating Rate of 50C/min up to 530C help for 1 hour, for Mg and Si elemental segregatoin at a grain boundary for time 0 to 10 minutes.

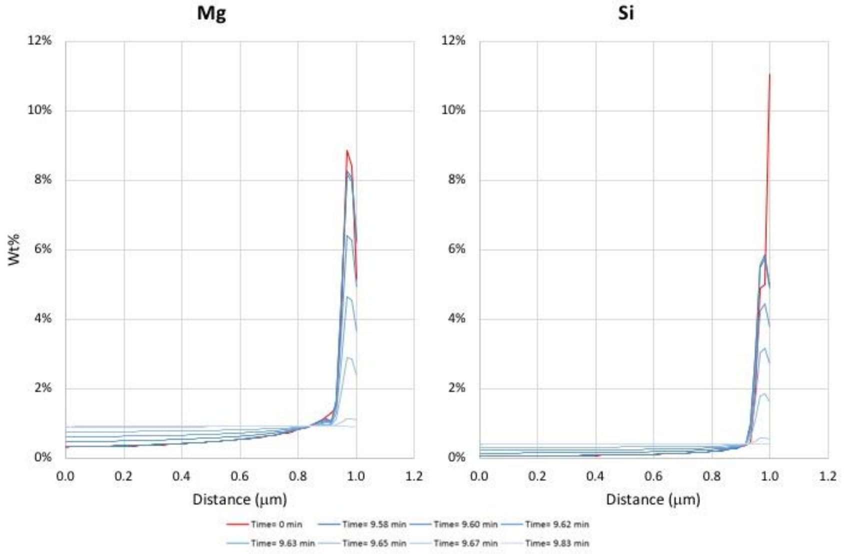

Figure 7. DICTRA Homogenization Model Output for Heating Rate of 50C/min up to 530C help for 1 hour, for Mg and Si elemental segregatoin at a grain boundary for time 9.5 to 10 minutes.

SEM EDS line scans at the boundaries of these powder particles were completed to experimentally verify these models. Figure 8 demonstrates and overlay of the modeling and experimental data. This graph shows a discrepancy between the modeling and experimental values, where there is no drastic solute peak at the grain boundary. Upon further investigation, this was attributed to the large interaction volume of the EDS scan in the SEM. Given this, more accurate line scans were completed using TEM EDS, where there is a much smaller interaction volume. Figure 9 depicts line scans across two different grain boundaries, which were assumed to be the same with solute segregation at each. Figure 9a. shows the line scan with the distinct solute peak at the grain boundary, where Figure 9b shows no peak in the solute concentration. Upon closer exploration, one boundary has a very bright contrast along the boundary and the other does not. This suggested that there is no solute segregation at these grain boundaries, rather a phase with a discrete composition. The following section will further investigate this theory.

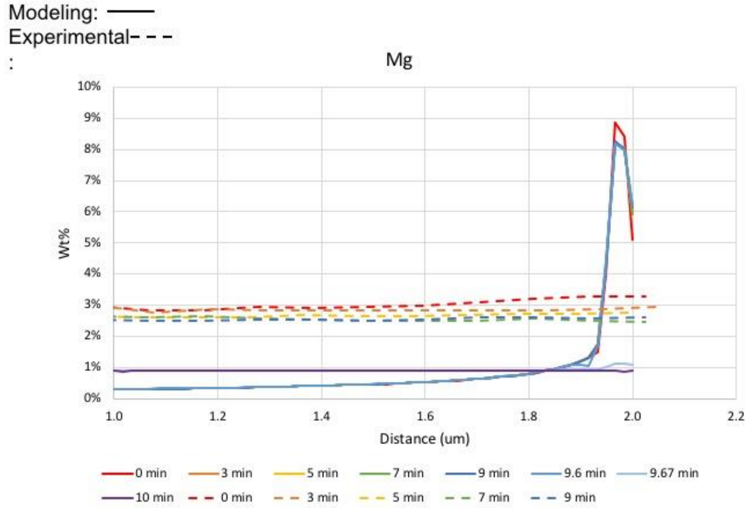

Figure 8. Overlay of Homogenization Model and Experimental SEM EDS line scans for grain boundary solute segregation.

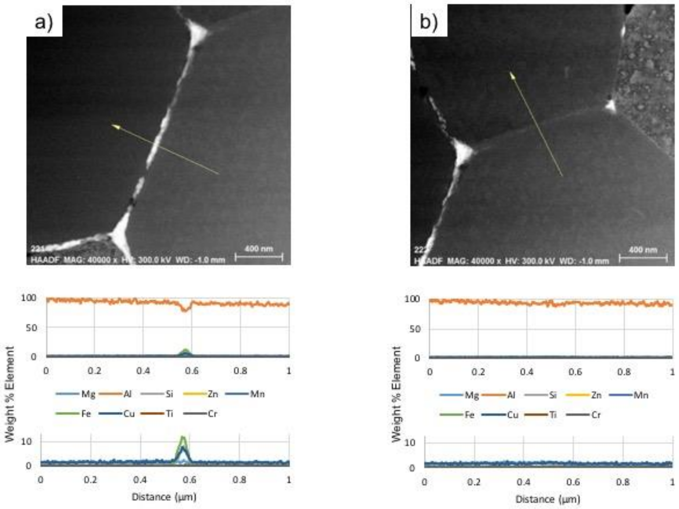

Figure 9. TEM EDS line scans across a grain boundary in an Al 6061 powder particle.

4.2 Experimentally Disproving Chemical Segregation in Aluminum Alloy Powders

Understanding the Non-Equilibrium Microstructure of Gas Atomized Aluminum Alloy Powders

Kyle Tsaknopoulos[1], Victor Champagne, Jr. [2], Danielle Cote[1*]

[1]Worcester Polytechnic Institute, Worcester, MA 01609
[2]US Army Research Laboratory, Aberdeen Proving Ground, MD 21005-5069
* Corresponding author; dlcote2@wpi.edu

Under Review

4.2.1 Abstract

Metallic feedstock powder is used for many additive manufacturing (AM) processes, including the solid state AM process, cold spray. In previous cold spray literature, characterization of the internal microstructure of the metallic feedstock powder, primarily aluminum alloys, has been performed. Said research suggested the presence of chemical solute segregation at the grain boundaries of these aluminum alloy powders. The work presented here will argue that there is not, in fact, chemical segregation within gas atomized Al powder particles. Instead, any initial chemical segregation from the atomization process immediately forms network phases at the grain boundaries and this is what is observed, despite having the appearance of chemical segregation. Analysis was performed on Al 2024, Al 6061, and Al 7075 using scanning electron microscope (SEM), transmission electron microscope (TEM), electron dispersive x-ray spectroscopy (EDS), and x-ray diffraction (XRD). The use of computational thermodynamic and diffusion models were employed. Based on these models and experimental results, the presence of S-phase and Al_2Cu in Al 2024, T-Phase and Al_7Cu_2Fe phases in 7075, and Mg_2Si and an AlFe intermetallic in Al 6061 were identified in the regions previously believed to be chemical segregation along the particle grain boundaries.

4.2.2 Introduction

Metallic powders have been formed using various approaches including physical milling, chemical formation, and atomization. The most common technique is gas atomization; gas atomization was created in the 1930s and produced metal powders for a variety of applications with a size distribution of 1 to 200 um. A metallic liquid melt is exposed to high pressure gas streams, forming discrete powder particles which rapidly solidify upon contact [1]. Rapid solidification and high cooling rates can lead to: increased solid solubility in the matrix, increase in non-equilibrium phases, decrease in grain size, and reduced chemical segregation [2-4]. The microstructural features in gas atomized powders differ greatly from traditional cast microstructures, which is expected due to the orders of magnitude difference in cooling rates, less than 102 K/s and approximately 107 K/s for cast and powders, respectively [5].

In the 1980s, many researchers began looking more closely at rapid solidification of metallic alloy systems. In 1984, research by Zindel et al. investigated the microstructure of rapidly solidified aluminum alloys using laser surface melting and melt spinning [6]. This paper evaluated secondary phases present in the rapidly solidified alloy. An article by Schaefer et al. used TEM and XRD to identify phases in a melt spun material [7]. Additional work also discussed the rapid solidification of metal powders using gas atomization techniques. These papers observed the microstructure, size distribution, and morphology of the powders. The characterization of the microstructure typically categorized the grain structure as cellular or dendritic. In 1986, Gayle et al. investigated Al-Li-Zr powders to modify the Al3Li phase to increase fracture toughness and ductility and allow for more commercial applications of the alloy [8]. In general, minimal phase identification was done for powders due to the small size of the phases. Some research chemically extracted the grain boundaries in order to perform XRD for identification purposes [9].

At this time, very little attention was paid to the internal microstructure of the powder; in most applications the powders were melted, leading to a new and different microstructure. In recent years, new attention has been given to solid state additive manufacturing processes such as cold spray and additive friction stir, where the internal microstructure of the powder is critical as it directly impacts the consolidated material properties. Initially, powder characteristics of interest to these processes were chemical composition, particle diameter, and morphology [10]. Recently, more attention is being given to the internal microstructure of the powders again, as it can influence the behavior of the powder in the AM processes. In the cold spray consolidation process, phases are retained and grain morphology is uniformly changed upon impact, contributing to the significance of full understanding the initial powder microstructure [12]. Most cold spray research with aluminum alloy feedstock powder refers to solute chemical segregation at the grain boundaries within these rapidly solidified powder particles [12-18].

Recent work by Rokni et al. on the properties of cold sprayed materials used SEM to describe the internal microstructure of as-atomized aluminum alloy powder particles for Al 7075 [12-14, 17]. These works used backscatter SEM imagine to conclude that there was solute segregation at the grain boundaries within the powder particles [12-14]. Similar work by Rokni et al. was conducted on Al 6061 gas atomized powder concluding using SEM EDS that the difference in chemical composition between the grain boundaries and the matrix was evidence to prove that this was chemical segregation at the boundaries [17]. No additional work was conducted by the authors to further analyze these boundaries.

Ajdelsztajn et al. studied aluminum alloy 2618 powder suggesting the presences of phases along the grain boundaries using SEM EDS [15]. Sebard et al. also suggested the presence of solute atoms at eh grain boundaries in Al 7075 powder particles [16]. EMPMA-WDS was used to show the solute segregation within the boundaries for this alloy.

Further research presented here suggests that this is indeed not chemical segregation as some others has suggested, rather multiple discrete phases in these aluminum alloy powders. This idea is explored below using electron microscopy and x-ray diffraction in combination with computational thermodynamic and diffusion modeling tools to guide in the process.

4.2.3 Experimental Methods

4.2.3.1 Materials:

The powder under consideration is gas-atomized Aluminum 2024, 7075, 6061 Aluminum powder from Valimet Inc. which was atomized in a nitrogen gas environment. The powder was mechanically sieved to size ranges of 28-33 μm, and 34-45 μm. The powder compositions of each alloy were determined using direct current plasma emission spectroscopy (ASTM E 1097-12) [19]. Compositions for each alloy powder are found in Table 1.

Table 1. Compositions of Al 2024, 7075, and 6061 Powder. All compositions in weight%.

Alloy	2024	7075	6061
Al	93.904	89.625	97.86
Mg	1.51	2.5	0.95
Si	0.13	0.15	0.49
Fe	0.065	0.17	0.27
Cu	3.83	1.59	0.25
Cr	0.0051	0.2	0.087
Zn	0.013	5.71	0.035
Mn	0.54	0.026	0.034
Ti	0.0029	0.029	0.024

4.2.3.2 Microstructural Analysis:

The microstructure of the as atomized powders were characterized using scanning and transmission electron microscopy (SEM and TEM), as well as energy dispersive x-ray spectroscopy (EDS) and x-ray diffraction (XRD). For SEM the powder samples were mounted in 2-part epoxy, Buehler EpoxiCure 2, and mechanically polished using a Struers Tegramin-20 Automatic polisher down to ¼ um using colloidal silica. SEM was done using a tungsten SEM, Zeiss EVO MA 10, at 10 kv using secondary electron (SE) and back scatter electron (BSE) modes. A silicon drift Xflash Detector 630M, Bruker, (Billerica, MA) EDS detector was used for chemical analysis of the microstructure.

For TEM, samples were prepared using a gallium focus ion beam (FIB) (FEI Helios Nanolab 660 dual beam FIB) to a thickness of about 300nm. The powder was sectioned by milling a powder particle perpendicular to the top surface to obtain a slice of the middle of the powder particle [20]. This slice was attached to a Mo-omni-grid and thinned to the final thickness of 300nm. TEM/STEM images were taken using a Probe-corrected FEI Titan Themis 300 S/TEM with ChemiSTEM technology using an accelerating voltage of 300kV. EDS was done using a Super-X EDS system at 300kV.

XRD was conducted using a Panalytical Empyrean using monochromatic Cu-Kα radiation over a 2θ range of 20-100 degrees at 40kV and 40mA.

4.2.3.3 Modeling Methods

Gas atomization is a rapid solidification technique; Scheil solidification theory can be utilized to predict the microstructure of rapidly solidified materials, making it an ideal tool for phase prediction in gas atomized powders. Thermo-Calc Software 2018a, TCAL5 Aluminum Database (Solna, Sweden) was used to calculate both Scheil solidification and equilibrium diagrams for each powder composition for comparison to demonstrate the possible phases present in all three alloys. These calculations were used to guide in the identification of the phases present in the alloy powders.

4.2.4 Results and Discussion

4.2.4.1 Modeling

In order to the Identify phases present in the aluminum alloy powders, used Thermo-Calc Equilibrium Diagram and Scheil Solidification Diagram were calculated to understand the potential phases that could be present in the alloys. The most abundant phases found in both diagrams were extracted and listed in Table 2.

Table 2: Most abundant phases present in Al 2024, Al 6061, and Al 7075 in both equilibrium and non-equilibrium conditions from Thermo-Calc data.

Alloy	Equilibrium Phases	Scheil Phases
2024	1. S-Phase (Al,Mg,Cu)	1. S-Phase (Al,Mg,Cu)
	2. Al_6Mn	2. Al_2Cu
	3. Al_2Cu	3. Al_6Mn
	4. Mg_2Si	4. $Al_{15}Si_2Mn_4$
	5. $Al_{12}Mn$	5. Mg_2Si
6061	1. Mg_2Si	1. Mg_2Si
	2. $Al_9Fe_2Si_2$	2. $Al_{13}Fe_4$
	3. T-Phase (Al,Mg,Cu,Zn)	3. Al_8Fe_2Si
	4. $Al_{45}Cr_7$	4. $Al_9Fe_2Si_2$
	5. $Al_{13}Fe_4$	5. Q-AlCuMgSi
7075	1. C14-Laves (Mg, Zn, Cu)	1. T-Phase (Al, Mg, Cu, Zn)
	2. T-Phase (Al, Mg, Cu, Zn)	2. S-Phase (Al,Mg,Cu)
	3. $Al_{45}Cr_7$	3. V-Phase (Al, Cu, Si, Mg)
	4. $Al_9Fe_2Si_2$	4. $Al_{13}Fe_4$
	5. Mg_2Si	5. Al_7Cu_2Fe

4.2.4.2 SEM

SEM micrographs were used to understand the internal microstructure of the as-atomized powders. Figure 1 reveals what appears to be chemical solute segregation at the grain boundaries in all three alloys using both SE and BSE modes. This is representative of what has been seen in literature for other aluminum alloy powders [12-18]. Elemental EDS in SEM was used to confirm the solute elements present at the grain boundaries (Figure 2). Figures 2a and b show the segregation of the Zn, Cu and Mg in Al 2024 and Al 7075, whereas Figure 2C shows elemental segregation of Si and Mg.

While the SEM EDS gives insight into the elements present at the grain boundaries of these powder particles, the SEM interaction volume is too large (about 1 μm^2) in comparison to the width of grain boundary (about 200nm). Therefore, SEM EDS cannot be used to accurately determine the chemical mapping of the internal microstructural for these powder particles. TEM must be used to more accurately gather information about the internal chemical microstructure.

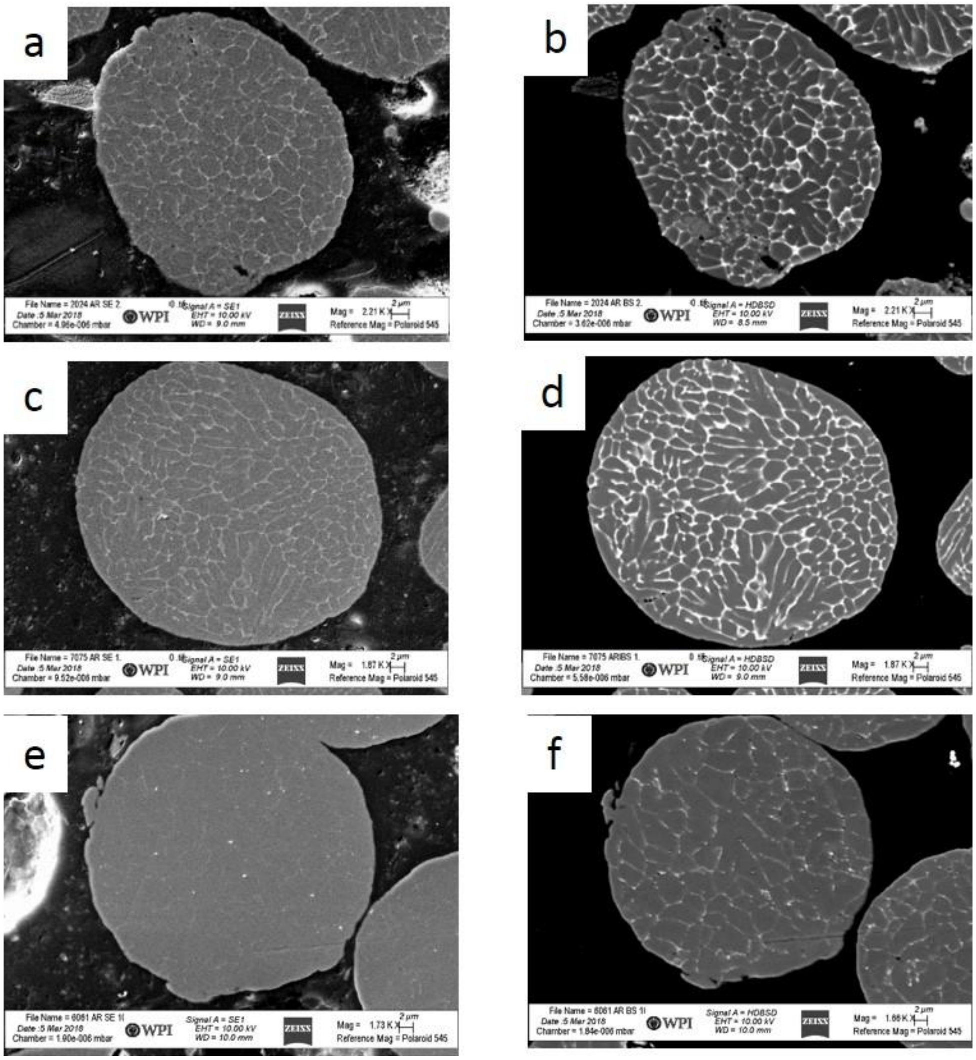

Figure 1. Microstructure of as atomized Al alloys a,b) 2024, c,d) 7075 and e,f) 6061 in SEM at 10kv SE (left column) and BS (right column).

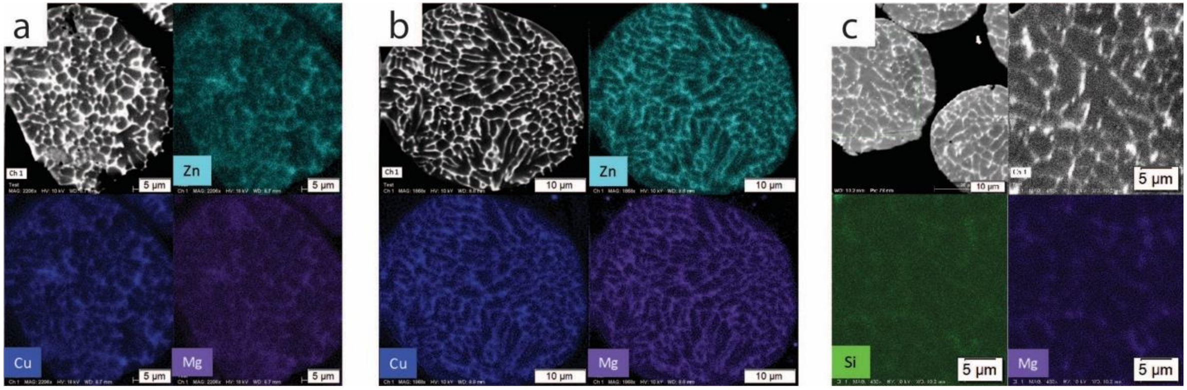

Figure 2. SEM EDS for a) 2024, b) 7075, and c) 6061 showing "elemental segregation" of major alloying elements.

4.2.4.3 TEM

4.2.4.3.1 Al 7075 Powder

The internal microstructure of the Al 7075 powder in TEM is found in Figure 3. While more detail can be seen than in the SEM, a connected network along the grain boundaries is still present. The appearance of chemical segregation is still observed, though parts of the micrograph resemble a network of solid phase instead. To obtain greater insight into the composition at these grain boundaries, TEM EDS line scans were conducted. Figure 4 displays STEM EDS line scans at the grain boundaries in the Al 7075 sample. Figure 4a,b. shows a line scan along a grain boundary, while Figure 4c.d. shows a line scan across a grain. Figure 4a. depicts major peak changes along the grain boundary, suggesting the presence of multiple different phases along a single boundary despite no visible phases discerned. Based on the line scan, the presence of T-phase and an AlFeCuSi phase are suspected, which is consistent with the phases predicted by the Scheil solidification Thermo-Calc models. Figure 4c shows distinct peaks at both grain boundaries, with no solute segregation across the center of the grain, further verifying the presence of discrete phases at the boundaries.

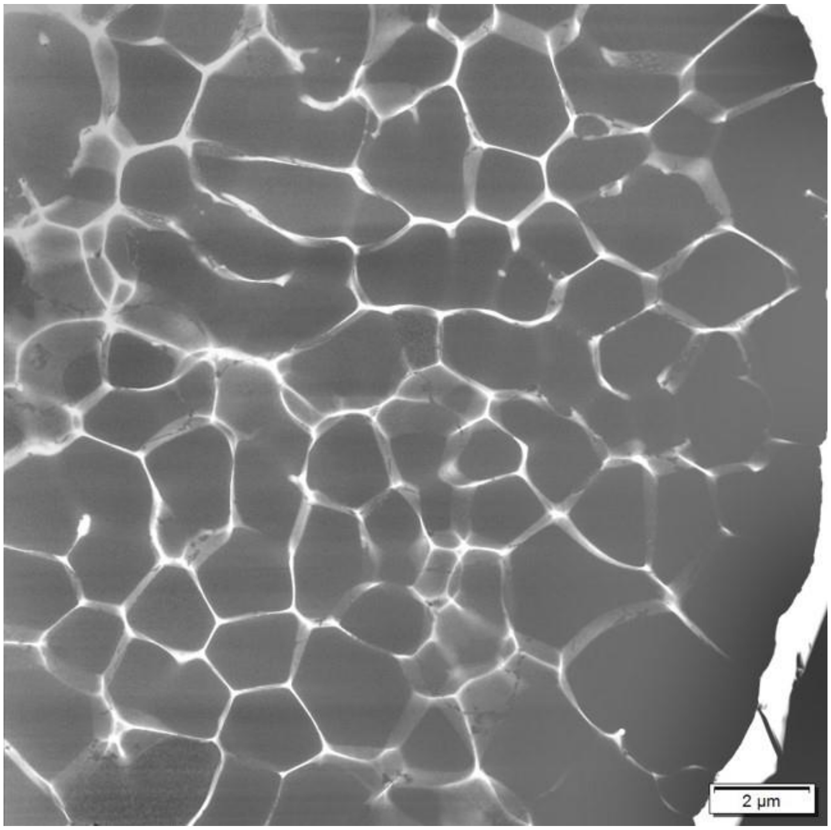

Figure 3. Overview STEM photo of 7075 powder microstructure.

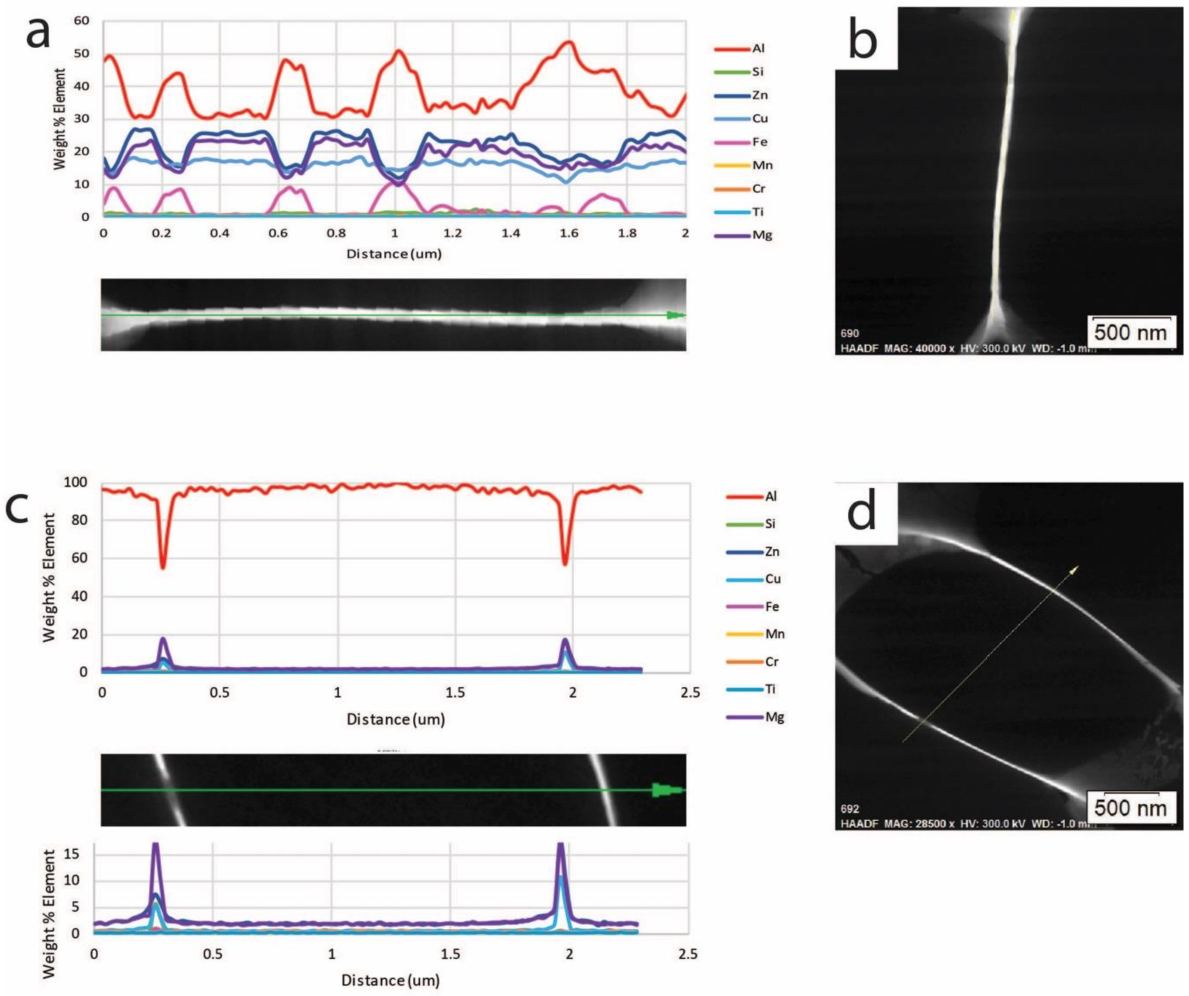

Figure 4. TEM EDS line scan in Al 7075 powder particle (A) Along a grain boundary, (B) across a grain.

4.2.4.3.2 Al 2024 Powder

Figure 5 demonstrates the microstructure in the Al 2024 powder in the as atomized condition. Figure 5a shows an overview of the microstructure. Figure 5b displays the location of a line scan across a grain boundary where Figure 5c contains the corresponding EDS data. The chemical composition at the grain boundary suggests the AlCuMg S-phase is present. This is consistent with Scheil solidification model predictions for Al 2024.

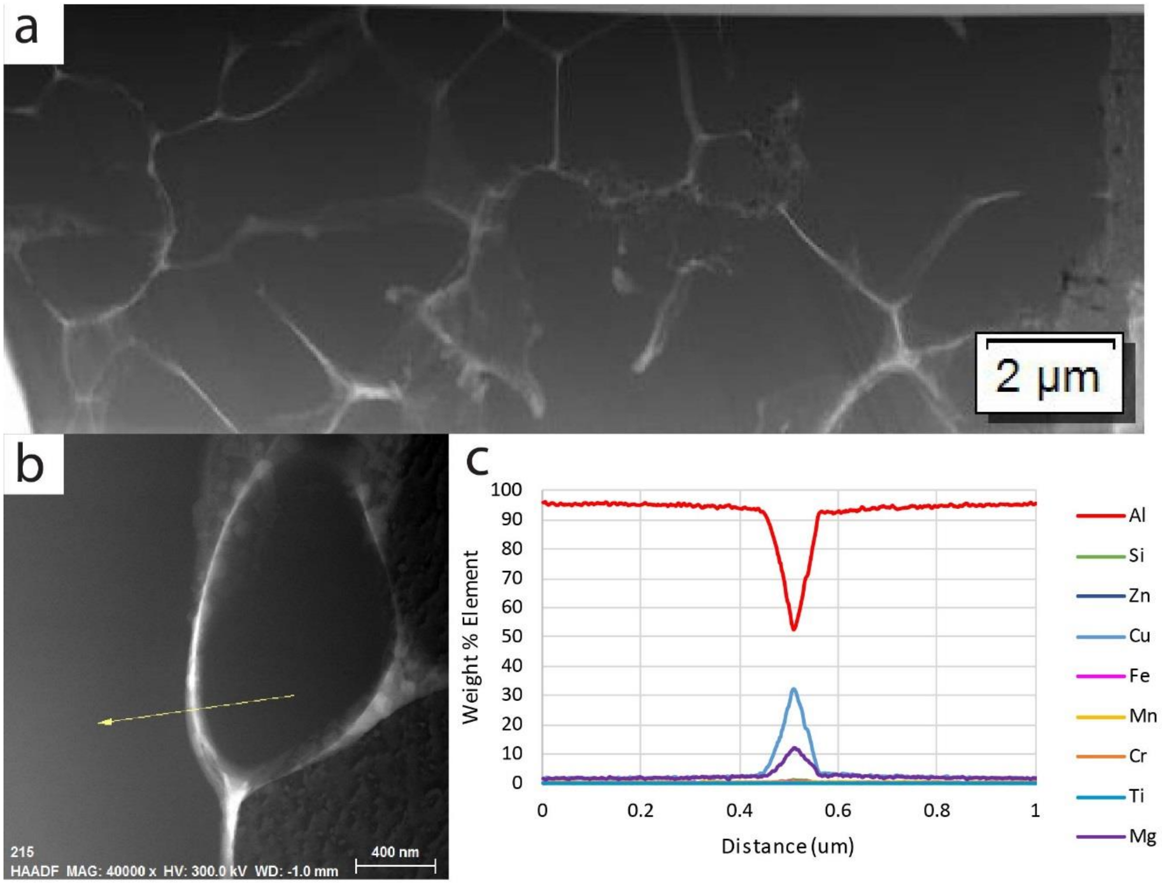

Figure 5. a) Overview STEM image of 2024 microstructure, b) magnified area for STEM EDS line scan, c) STEM EDS line scan data across a grain boundary.

4.2.4.3.3 Al 6061 Powder

The typical microstructure of an Al 6061 powder particle in the as-atomized condition is found in Figure 6. This shows distinct light and dark contrasting alternating layers at the grain boundaries, suggesting the presence of phases rather than segregation.

Figure 7 displays two line scans across grain boundaries in Al 6061 powder. Figure 7a shows the scan where the boundary is light in color, while Figure 7b shows a darker boundary. Figure 7a shows a spike in solute elements at the grain boundary, (Al, Fe, Cu, Si), consistent with the AlFe phases predicted by the Scheil solidification diagram. Figure 7b shows no spike in solute elements, demonstrating no chemical segregation at the grain boundary.

Figure 8 reveals two different orientations of the phases found at the grain boundaries in Al 6061 powder. Figure 8a illustrates what appears to be separate discrete phases along a thin boundary. The elemental EDS maps suggest that these phases are a MgSi phase (likely Mg_2Si) and an AlFe phase ($Al_{13}Fe_4$, Al_8Fe_2Si, or $Al_9Fe_2Si_2$) alternating. Figure 8b shows a dendritic-like structure of the same phases along a different grain boundary. The structure found in Figure 8b has been revealed as a different orientation perpendicular to the structure revealed in Figure 8a. The red line in Figure 8b demonstrates where a cross section could have been taken to see the structure found in 8a in the perpendicular direction. The elemental EDS maps are consistent with those found in Figure 8a, further proving that they are indeed the same phase of different orientations.

As a result of this work, the secondary phases present in this as-atomized alloy have been further investigated and concretely identified with additional TEM investigation by Tsaknopoulos et al. [21].

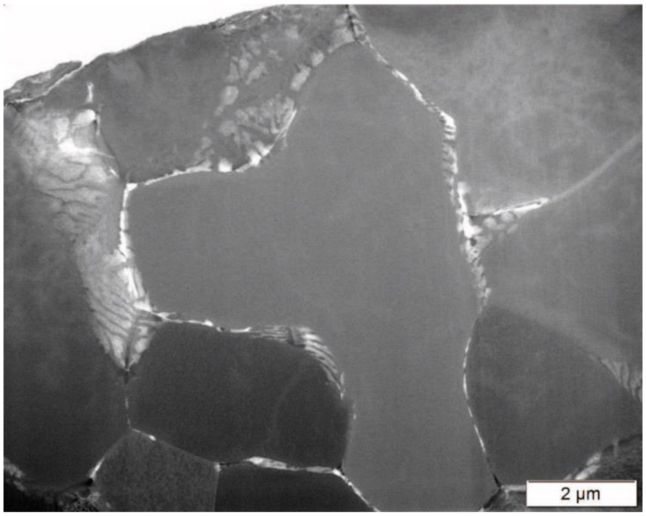

Figure 6. TEM of 6061 internal microstructure.

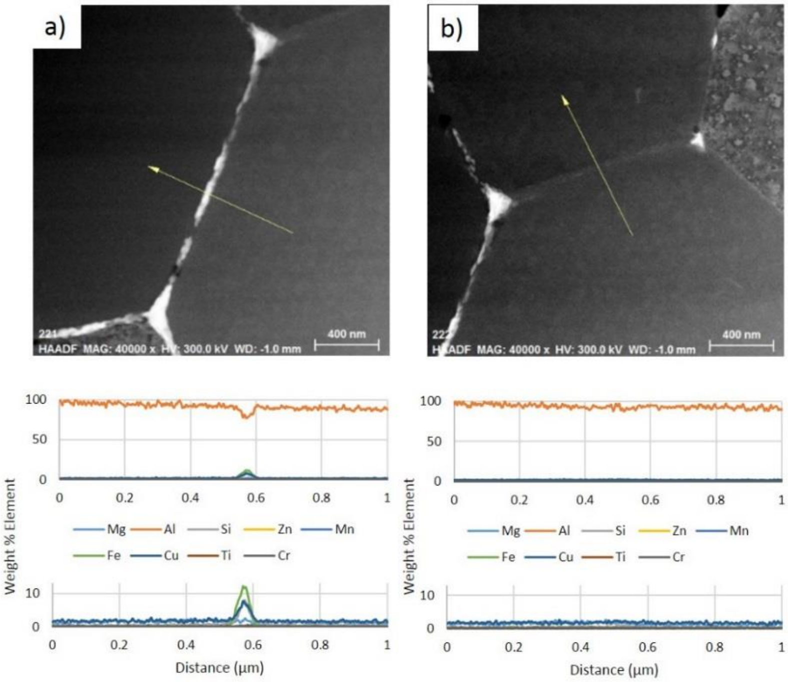

Figure 7. a. line scan across bright colored grain boundary. b. line scan across darker colored grain boundary.

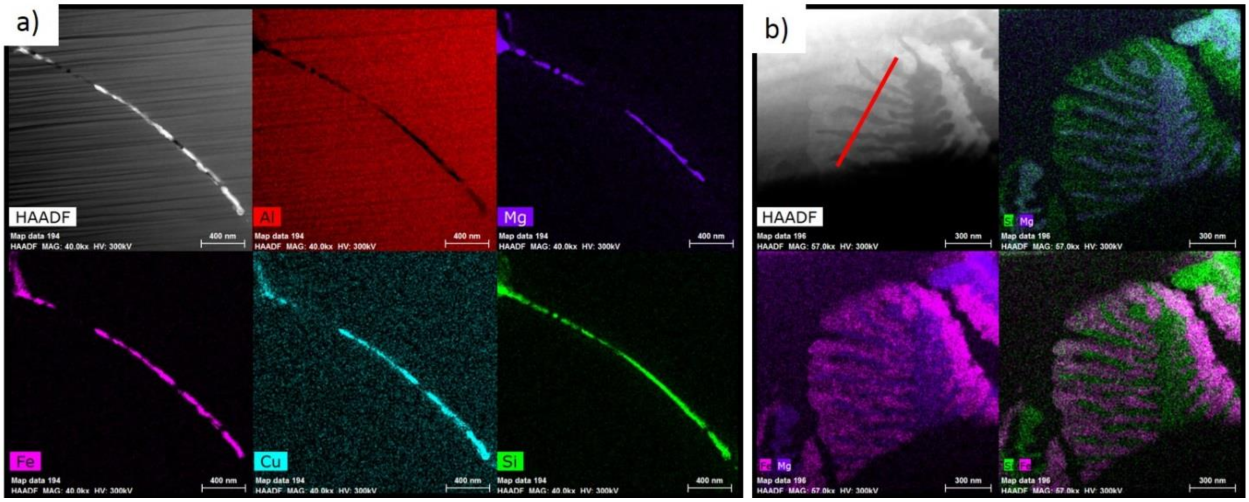

Figure 8. Two different view of the Al 6061 microstructure. Figure a. is a cross-section of figure b.

4.2.4.3.4 XRD

X-Ray diffraction was conducted on loose as-atomized aluminum alloy powders to identify the secondary phases present and support the TEM analysis. Figure 9a displays the initial XRD results revealing aluminum matrix peaks. Figure 9b shows a magnified view of Figure 9a to highlight the presence of low intensity peaks corresponding to some secondary phases in the alloys. The phase in Table 2 were used as a guide to identify the lower intensity peaks in the XRD patterns. In Al 7075, the Al_7Cu_2Fe phase was identified. In Al 2024, Al_2Cu was identified, and in Al 6061, Mg_2Si was identified. Some additional phases predicted by the Thermo-Calc models had overlapping peaks with the high intensity aluminum peaks, and were therefore unable to be uniquely identified.

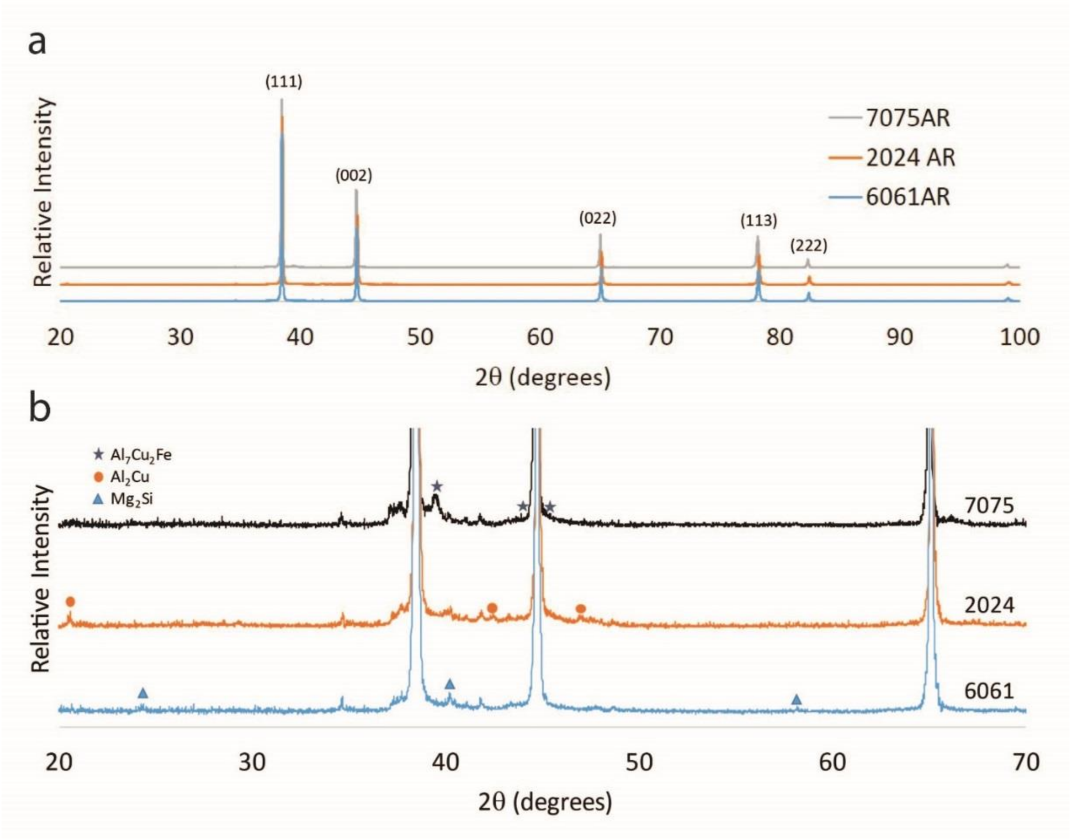

Figure 9. a) XRD of Al 7075, 2024, and 6061, b) increased magnification of a).

4.2.5 Conclusions

For Al alloys 2024, 6061, and 7075 in the as-atomized condition, the grain boundaries, which were previously believed to be chemical solute segregation, proved instead to consist of discrete secondary phases. SEM analysis has been misleading when making conclusions about the internal microstructure of the aluminum alloy powder particles. TEM analysis alone also did not reveal discrete secondary phases. Instead, TEM coupled with EDS and XRD analysis provided evidence to the support the presence of the secondary phases, which were also predicted by the Thermo-Calc models. The preliminary identification suggests that the Scheil solidification model more accurately predicts the phase present in these as-atomized aluminum alloy powders than the equilibrium model results. Based on the current evidence, phases expected to be present in these alloys include:

- Al 7075: T-Phase, Al_7Cu_2Fe
- Al 2024: S-Phase, Al_2Cu
- Al 6061: β (Mg2Si), AlFe phase ($Al_{13}Fe_4$, Al_8Fe_2Si, or $Al_9Fe_2Si_2$)

More in-depth phase analysis will be conducted on these and other Al alloy powders in future work.

4.2.6 Acknowledgements

This work was funded by the United States Army Research Laboratory, grant #W911NF-15-2-0024.

This work was performed in part at the *Kostas Advanced Nano-Characterization Facility in Kostas Research Institute at Northeastern University* and at the *Center for Nanoscale Systems (CNS)*, a member of the National Nanotechnology Coordinated Infrastructure Network (NNCI), which is supported by the National Science Foundation under NSF award no. 1541959.

4.2.7 References

1. Adam, C.M. Rapid Solidification Processing Methods. In *Mechanical Behavior of Rapidly Solidified Materials: Proceedings of a symposium at the AIME Annual Meeting*, Sastry, S.M. L., MacDonald, B.A., Eds.; A Publication of The Metallurgical Society, Inc.: Warrendale, PA, 1986, pp. 21-40.
2. Looft, D.J.; van Reuth, E.C. Rapid Solidification Processing: An Overview. In *Rapid Solidification Processing: Principles and Technologies: Proceedings of the International Conference on Rapid Solidification Processing*, Mehrabian, R.; Kear, B.H.; Cohen, M., Eds.; Claitor's Publishing Division, Baton Rouge, LA, 1978, pp. 1-8.
3. Sater, J.M.; Sanders Jr., T.H.; Garrett Jr., R.K. Characterization of Rapidly Solidified Materials. In *Rapidly Solidified Powder Aluminum Alloys: A symposium sponsored by ASTM Committee B-9 on Metal Powders and Metal Powder Products: SPT 890,* Fine, M.E., Starke, E.A., Eds.; ASTM International, Philadelphia, PA, 1986, pp. 83-117.
4. Grant, N.J. Rapid Solidification Technology: Progress and Problems. In *Powder Metallurgy in Defense Technology: Proceedings of the P/M in Defense Technology Seminar at David Taylor Naval Ship Research & Development Center,* Ullrich, W.J. Ed.; Metal Powder Industries Federation, Princeton, NJ, 1987, Volume 7, pp. 85-102.
5. Cohen, M.; Kear, B.H.; Mehrabian, R. Rapid Solidification Processing: An Outlook. In *Rapid Solidification Processing: Principles and Technologies, II: Proceedings of the Second International Conference on Rapid Solidification Processing*, Mehrabian, R., Kear, B.H., Cohen, M., Eds.; Claitor's Publishing Division, Baton Rouge, LA, 1980, pp. 1-23.
6. Zindel, J.W.; Stanley, J.T.; Field, R.D.; Fraser, H.L. Microstructures of Rapidly Solidified Aluminum Alloys. In *Rapidly Solidified Metastable Materials: Materials Research Society Symposia Proceedings*, Kear, B.H., Giessen, B.C., Eds.; Elsevier Science Publishing Co., Inc., New York, New York, 1984, Volume 28, pp. 317-322.
7. Schaefer, R.J.; Shechtman, D.; Biancaniello, F.S. Rapid Solidification Microstructure and Precipitation in Al-Mn Alloys. In *Rapidly Solidified Metastable Materials: Materials Research Society Symposia Proceedings,* Kear, B.H., Giessen, B.C., Eds.; Elsevier Science Publishing Co., Inc., New York, New York, 1984, Volume 28, pp. 323-328.
8. Gayle, F.W.; Vander Sande, J.B. Al3Li Precipitate Modification in an Al-Li-Zr Alloy. In *Rapidly Solidified Powder Aluminum Alloys: A symposium sponsored by ASTM Committee B-9 on Metal Powders and Metal Powder Products: SPT 890,* Fine, M.E., Starke, E.A., Eds.; ASTM International, Philadelphia, PA, 1986, pp. 137-153.
9. VanStone, R.H.; Rizzo, F.J.; Radavich, J.F. Microstructures of Gas Atomized Rene' 95 Powder. In *Rapid Solidification Processing: Principles and Technologies, II: Proceedings of the Second International Conference on Rapid Solidification Processing*, Mehrabian, R., Kear, B.H., and Cohen, M., Eds.; Claitor's Publishing Division, Baton Rouge, LA, 1980, pp. 260-272.
10. Brodmann, F.J. Cold spray process parameters: powders. In *The CS Materials Deposition Process*, Champagne, V.K., Ed.; Woodhead Publishing Ltd., Cambridge, England, 2007, pp. 105-116.
11. Karthikeyan, J. The advantages and disadvantages of the cold spray coating process. In *The CS Materials Deposition Process,* Champagne, V.K., Ed.; Woodhead Publishing Ltd., Cambridge, England, 2007, pp. 62-71.

12. Rokni, M.R.; Nutt, S.R.; Widener, C.A.; Champagne, V.K.; Hrabe, R.H. Review of relationship between particle deformation, coating microstructure and properties in high-pressure cold spray. *Journal of Thermal Spray Technology* **2017**, 26, 1308-1355.
13. Rokni, M.R.; Widener, C.A.; Champagne, V.K.; Crawford, G.A. Microstructure and Mechanical Properties of Cold Sprayed 7075 Deposition During Non-isothermal Annealing. *Surf. Coat. Technol*. **2015**, 276, 305-315.
14. Rokni, M.R.; Widener, C.A.; Crawford, G.A. Microstructural Evolution of 7075 Al Gas Atomized Powder and High-pressure Cold Sprayed Deposition*. Surf. Coat. Technol.* **2014**, 251, 254-263.
15. Ajdelsztajn, L.; Zuniga, A.; Jodoin, B.; Lavernia, E.J. Cold Gas Dynamic Spraying of a High Temperature Al Alloy. *Surf. Coat. Technol.* **2016**, 201, 2109-2116.
16. Sabard, A.; de Villiers Lovelock, H. L.; Hussain, T. Microstructural Evolution in Solution Heat Treatment of Gas-Atomized Al Alloy (7075) Powder for Cold Spray. *Journal of Thermal Spray Technology* **2018**, 27, 145-158.
17. Rokni, M.R.; Widener, C.A.; Crawford, G.A., West, M.K. An investigation into microstructure and mechanical properties of cold sprayed 7075 Al deposition. *Materials Science and Engineering: A* **2015**, 625, 19-27.
18. Rokni, M.R.; Widener, C.A.; Champagne, V.R. Microstructural stability of ultrafine grained cold sprayed 6061 aluminum alloy. *Applied Surface Science* **2014**, 290, 482-489.
19. ASTM E1097-12, ASTM International, West Conshohocken, PA, 2017.
20. Ernst, A.; Wei, M.; Aindow, M. FIB Milling strategies for TEM Sample Preparation of Spheroidal Powder Particles. *Microscopy and Microanalysis* **2018**, 24, 826-827.
21. Tsaknopoulos, K.; Walde, C.; Champagne, V.K., Cote, D. Gas-Atomized Al 6061 Powder: Phase Identification and Evolution During Thermal Treatment. *JOM* **2019**, 71, 435-443. https://doi.org/10.1007/s11837-018-3175-7

5 Microstructural Evolution in Al 2024 Powder

The Microstructural Evolution of Rapidly Solidified Powder Aluminum 2024 during Thermal Processing

Caitlin Walde[1], Kyle Tsaknopoulos[1], Victor Champagne, Jr. [2], Danielle Cote[1*]

[1]Worcester Polytechnic Institute, Worcester, MA 01609
[2]US Army Research Laboratory, Aberdeen Proving Ground, MD 21005-5069
* Corresponding author; dlcote2@wpi.edu

Journal: Metallography, Microstructure and Analysis

Online March 29, 2019

https://doi.org/10.1007/s13632-019-00535-2

5.1 Abstract

Gas-atomized metallic powders are commonly used in solid state deposition processes, such as Cold Spray and Additive Friction Stir. While their post-process consolidated properties are widely studied, there is little research on the properties of the powders before processing. Understanding the powder characteristics before use in additive manufacturing could lead to fine-tuning properties of additively manufactured materials. This research studied the effect of various thermal treatment processes on the characteristics and microstructural evolution of powder aluminum alloy 2024. Treatment times and temperatures were guided by thermodynamic modeling. Light microscopy, scanning electron microscopy, transmission electron microscopy, energy dispersive x-ray spectroscopy, electron backscatter diffraction, and differential scanning calorimetry were used to evaluate each condition. Thermodynamic models were used to predict the phase stability in these powders, and were calibrated using the experimental results to give a more complete understanding of the phase transformations during thermal processing.

5.2 Introduction

Aluminum 2024, the alloy used in this study, is an age-hardenable alloy that is widely used in the aircraft and aerospace industries for wrought components, coatings, and repair applications [1]. For the coating and repair applications, powder is the most common feedstock, which is typically generated using the process of gas atomization [2]. During this process, the molten alloy is atomized using a gas stream and the produced droplets subsequently undergo rapid cooling, resulting in powder particles with an as-cast dendritic microstructure that inherently contain segregation of alloying elements [3]. The processing parameters also affect the morphology of the resulting particles, all of which are primarily spherical, though the mixture contains a wide size distribution. Powders tend to have higher strength and hardness than their bulk counterparts due to their small grain size and rapidly-solidified metastable state [4-7]. Initial results show that parts that are deposited using cold spray in a solid state from these powders can also have higher strength than their bulk counterparts but often have lower ductility [8].

Coatings and repair applications often utilize solid state deposition processes, with gas-atomized powder for feedstock. In these solid-state processes, such as cold spray and additive friction stir, the feedstock powder is not melted [9,10], thus preserving the chemistry, initial phase composition, and crystal structure. Additionally, these lower temperature processes potentially avoid unwanted grain growth that can occur with high temperatures [11].
Heat treatments are often applied to certain aluminum alloys to intentionally manipulate their microstructure and, subsequently, their mechanical properties. One of the main steps of a heat treatment process is a solution treatment, in which a sample is heated to a given temperature, held for a specified amount of time, then followed by a quench. This process is intended to re-dissolve solidified phases and segregated elements into a super-saturated solid solution, and the quench enables retention of this metastable structure at lower temperature. The next step in a heat treatment is the aging treatment, which is intended to nucleate and grow specific phases that enhance the strength. The primary strengthening phases of 2024 are the S (orthorhombic Al_2CuMg) and θ (tetragonal Al_2Cu) phases [12], both of which can be dissolved

during the solution treatment step and then precipitated through their sequences to obtain optimal dispersion and therefore optimal strength. This study evaluated treatment times in order to optimize the solid solution to enable maximum precipitation of these beneficial phases during a subsequent aging step.

Currently, optimization of these parameters is often accomplished by an Edisonian approach of trial and error. To decrease process development time, models can be used to predict microstructural evolution during heat treatment in order to engineer materials with desirable properties. Models have been developed using commercially available thermodynamic and kinetic software (e.g. Thermo-Calc, JMatPro, and Pandat); however, before the data from these models can be fully utilized, they must first be validated. This paper addresses experimental validation of the control of the powder microstructure through solution treatment and quenching steps in order to improve the properties of solid state deposition processes.

5.3 Method

5.3.1 Powder

The powder used for this study was Al 2024, gas atomized in nitrogen (Valimet, Stockton, CA). The received powders were mechanically sieved using sieves compliant with ASTM E 11 into seven classifications to aid in the repeatability of selecting similarly sized particles for analysis [13]. The size classifications were <25 µm, 25-32 µm, 32-28 µm, 38-45 µm, 45-53µm, 53-63 µm, and >63 µm. The 45-53 µm category was chosen for this analysis, as it was the most abundant. This category had a d_{10}, d_{50}, and d_{90} of 18 µm, 34 µm, and 60 µm respectively. The chemical composition of the studied powder was 3.93 wt% Cu, 1.51 wt% Mg, 0.54 wt% Mn, 0.262 wt% O, 0.13 wt% Si, 0.065 wt% Fe, 0.029 wt% Ti, 0.013 wt% Zn, 0.0051 wt% Cr, with the balance Al, as measured by direct current plasma emission spectroscopy [14]. When compared to the ASTM standard, this is within the acceptable composition ranges [15].

5.3.2 Modeling

A solution treatment is intended to re-dissolve secondary phases and segregated elements formed during solidification into a super-saturated solid solution to obtain a more homogenous microstructure. Previous work using JMatPro software models determined that chemical segregation is redistributed much faster than the secondary phases are dissolved, due to the fast diffusion rates at the small scale lengths seen in powders [2]. Therefore, only the dissolution of secondary phases was considered when determining thermal treatment time and temperatures needed for homogenization.

The thermal treatment parameters to dissolve secondary phases were selected using Thermo-Calc software (Stockholm, Sweden); the goal was to maximize the degree of intermetallic dissolution while avoiding melting. Figure 1a shows the equilibrium secondary phases present in Al 2024 as a function of temperature. Though gas atomized powder particles are not in a state of equilibrium due to their rapid solidification, this data was useful in determining the treatment temperature by revealing melting temperatures of secondary phases.

The dark blue line in Figure 1a indicates the presence of liquid (melting) increases above temperatures of 530 °C; hence, the treatment temperature must be below 530 °C. Additionally,

Figure 1a was inspected for a minimum of phases present, which occurs around 500 °C. Upon further consideration of wrought 2024 treatments and potential incipient melting, 490 °C was chosen [16].

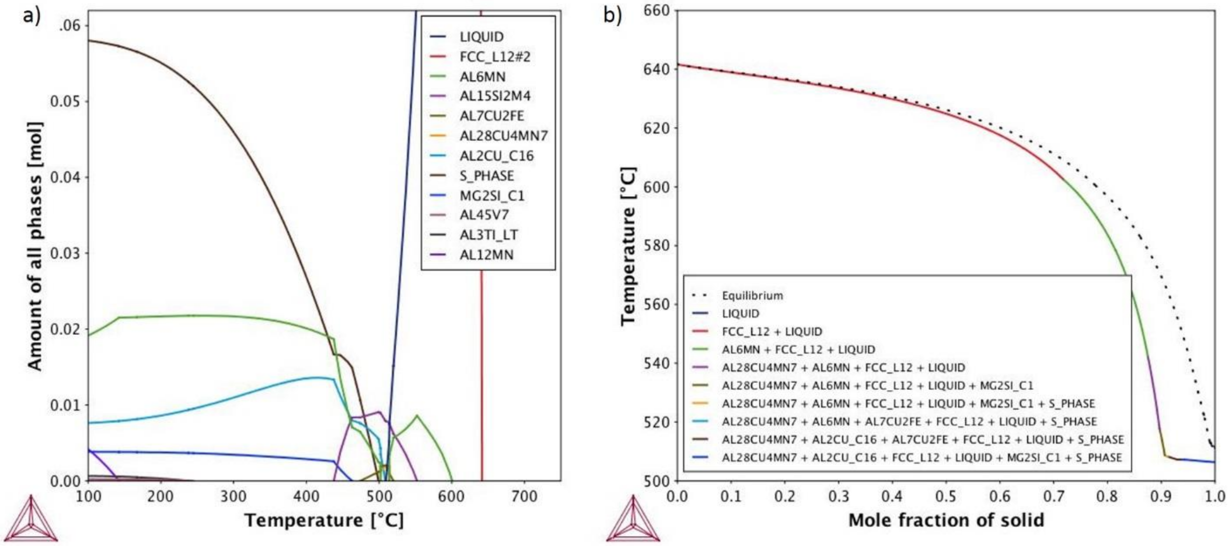

Figure 1. Phase diagrams predicted using Thermo-Calc for a) non-equilibrium conditions (Scheil Solidification) and b) equilibrium conditions.

The thermal treatment time required to dissolve the secondary phases at the pre-determined temperature was simulated using a diffusion-based module in the Thermo-Calc software, DICTRA, and will be further discussed in future publications. Here, experimental work was performed to determine the ideal thermal treatment time and validate the diffusion-based model.

The Thermo-Calc software was also used to help identify the secondary phases present in the powder microstructures through the use of the equilibrium diagram in Figure 1a, and the non-equilibrium Scheil solidification diagram in Figure 1b for both the thermally treated and as-received conditions, respectively.

5.3.3 Treatment

Al Powder samples were sealed in crucibles for treatment in a differential scanning calorimeter (DSC) (TA Instruments Discovery DSC with LN2P cooler). They were heated at 50°C/min to 490 °C (as determined by Thermo-Calc models), and held for times between 0-2 hours in increments of 20 minutes, then quenched at approximately 120°C/min. All experiments were performed in an inert nitrogen environment. One sample was left untreated in the as-received condition.

5.3.4 Characterization

Characterization of the powders was performed using differential scanning calorimetry (DSC), light microscopy, scanning electron microscopy (SEM), energy dispersive spectroscopy (EDS), transmission electron microscopy (TEM, STEM) and electron backscatter (EBSD) to evaluate the evolution of the secondary phases.

DSC was performed using a TA Instruments Discovery DSC. Scans were run with a Nitrogen purge gas at 50 mL/min, and at a scanning rate of 10 °C/min from ambient to 500 °C.
After treatment, samples were mounted in a two part epoxy resin (EpoxiCure 2, Buehler, Lake Bluff, IL), and then were ground and polished using an automatic polisher (Tegramin-20, Struers, Cleveland, OH) with a final 0.25µm colloidal silica suspension for metallographic examination.

While grain recrystallization was not the goal of the treatments, it may still occur. For grain size analysis, the polished samples were etched using Keller's reagent for 5 seconds each to reveal the microstructure then measured via light microscopy. Light microscopy micrographs were taken using an Olympus GX71 stereoscope.

SEM micrographs were taken using a Zeiss EVO-MA10. EDS was performed using a silicon drift detector Xflash Detector 630M, Bruker, Billerica, MA). EDS analysis was performed in SEM, however little can be gleaned from the results. The secondary phases present in these rapidly-solidified powders are smaller than the interaction volume of the electron beam, so it is not possible to differentiate between the different phases. EDS using transmission electron microscopy (TEM) was additionally performed to accurately identify each phase. The reduced interaction volume of the TEM beam increases the resolution available for phase analysis.
A gallium focused ion beam (FIB) (FEI Helios 660 Nanolab and FEI Scios Dual Beam FIBs) was used to prepare samples for TEM. In order to section the powder in the FIB, powder was adhered to an SEM stub using carbon tape [17]. A powder particle was chosen and then a protective Pt layer was deposited on the top of the particle (45 µm X 1 µm X 1 µm). The FIB was used to mill perpendicularly to the surface to take away the material on either side of the Pt layer. This slice of the powder particle was then lifted out and attached to a Mo omni-grid. The sample was thinned to a thickness of about 100nm. Smaller samples were then extracted from the larger slice for further EDS analysis and where thinned to 50nm to minimize signal interaction from the matrix behind the chosen phase being analyzed.

A Probe-corrected FEI Titan Themis 300 S/TEM with ChemiSTEM technology was used to take TEM and STEM images at an accelerating voltage of 300kV. A Bruker Super-X EDS system was used for EDS analysis at 300kV.

Additionally, the as-received and 60 min heat treated conditions were evaluated utilizing electron backscatter diffraction (EBSD) to evaluate the orientation structure of the rapidly solidified powder. The EBSD samples were prepared by milling in the FIB. EBSD was performed using an EDAX EDS detector at an accelerating voltage of 20 kV with a step size of 0.3 µm.

5.4 Results & Discussion

5.4.1 Microstructure

5.4.1.1 Light Microscopy

Light microscopy micrographs were taken to measure the effect of thermal treatment on the grain size of the powder. While unintended, grain growth or recrystallization may occur during these thermal treatments; thus, it is important to understand the effect of the thermal treatments on all aspects of the microstructure of the powder. The initial grain size of the powder was 1.5 µm, which is consistent with what is reported in literature. It was seen that after an initial growth from heating of about 0.5 µm, there was no appreciable grain growth with increasing treatment time.

5.4.1.2 SEM

SEM micrographs were taken to evaluate the evolution of the secondary phases as a function of treatment time. Samples of micrographs used are shown in Figure 2 a-h, with Figure 2 e-f having a higher magnification than Figure 2 a-d. Area fraction of the secondary phases were measured using image thresholding. Some precipitates were too small to be seen in the SEM; these were investigated through the use of TEM. Figure 2 i-l shows the image thresholding process, where the green areas represent the areas of the secondary phases that were used in the analysis. Multiple micrographs were taken for each condition and then results were averaged. This is one advantage of SEM over TEM – the ability to quickly gather data from many powder particles, resulting in a broader understanding of the microstructure of each treatment condition.

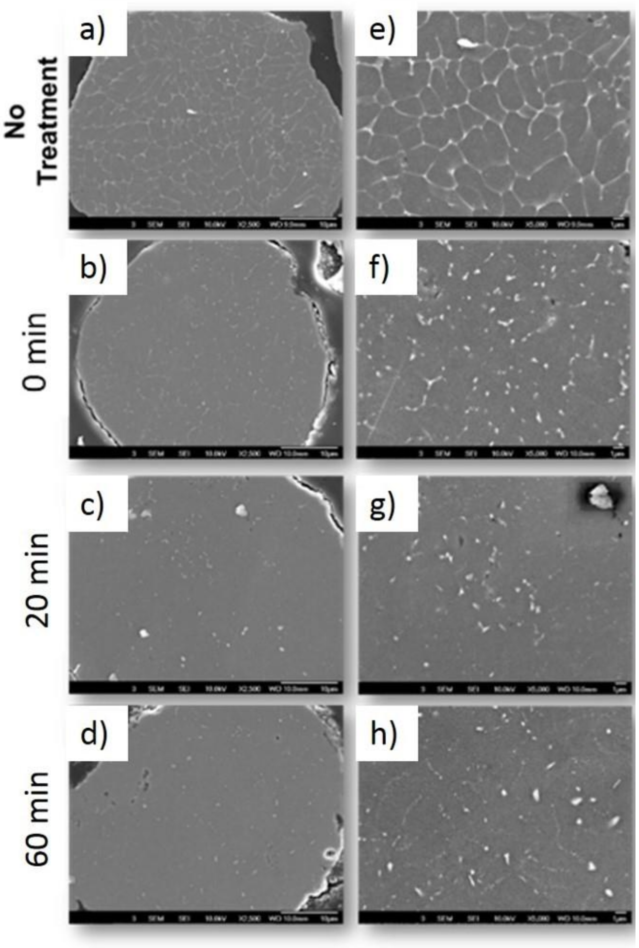

Figure 2. 2a. Low mag SEM micrograph of powder in as-received condition, 2b. Low mag SEM micrograph of powder with 0 min treatment time, 2c. Low mag SEM micrograph of powder with 20 min treatment time, 2d. Low mag SEM micrograph of powder with 60 min treatment time, 2e. High mag SEM micrograph of powder in as-received condition, 2f. High mag SEM micrograph of powder with 0 min treatment time, 2g. High mag SEM micrograph of powder with 20 min treatment time, 2h. High mag SEM micrograph of powder with 120 min treatment time.

Figure 3 shows the secondary phase area fraction as a function of treatment time. The trend suggests the general dissolution of the segregation and secondary phases within the first hour, but growth between one and two hours. It is hypothesized that this is a result of competing growth and dissolution of different phases, which will be further addressed with the TEM results.

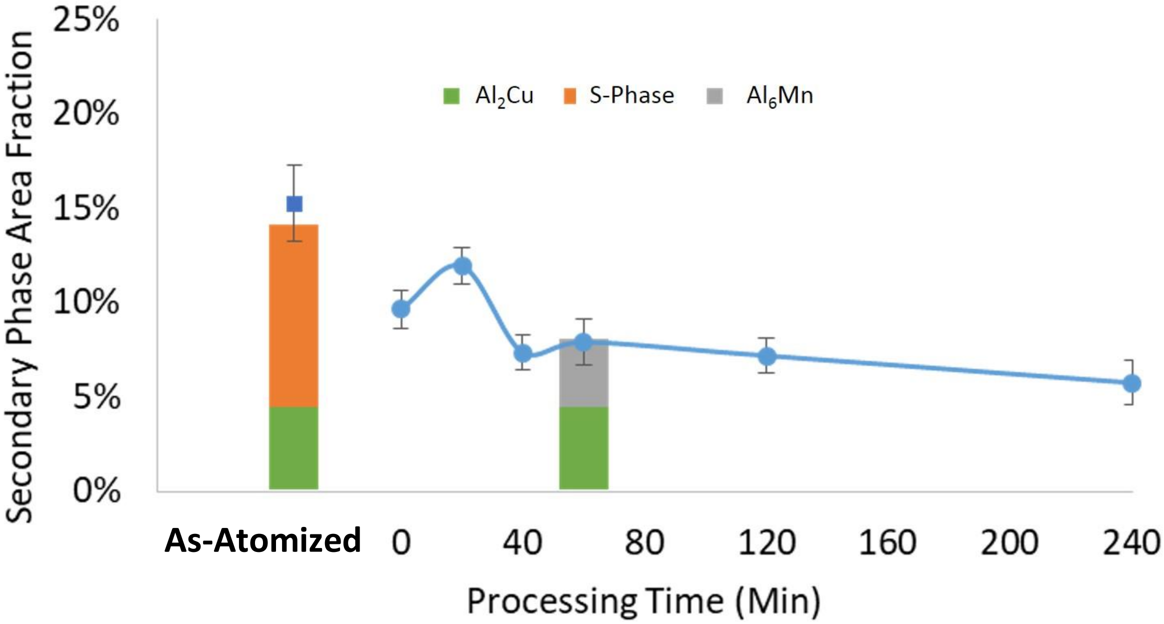

Figure 3. Secondary phase area fraction vs. treatment time. Blue line represents the fraction calculated from SEM images, while bars represent the fraction calculated from TEM images.

EBSD was used secondarily to evaluate the granular structure of the rapidly solidified powders. A preliminary evaluation was only performed on the as-received and 60 minute thermally treated conditions. Figure 4 shows EBSD micrographs and corresponding electron backscatter micrographs of both conditions. The grain size measured via this method was found to be 3-4 µm in both the as-received and thermally treated conditions. When the grain size from both of these EBSD micrographs are compared to the cell sizes seen in the corresponding SEM micrographs, there is a discrepancy. The sizes of the granular features measured from SEM are of comparable size to the feature size measured via light microscopy after etching, while the size of the features from EBSD are considerably larger than both of those. This implies that there are both granular and sub-granular structures in these rapidly solidified powders. This is consistent with results seen for as-received 6061 powder, showing a granular and sub-granular structure[6]. However, in the 6061, the authors saw a reorientation of the grains after thermal treatment for 60 minutes, which is not the case in the 2024 powder seen here. The alloying content of the studied 6061 was much lower than that of the 2024 studied here; 2 wt% in the 6061, compared to the 6 wt% in the 2024 here. Given the difference in the composition, there is a greater driving force for the precipitation of secondary phases in the 2024, leading to more phases per area. Increased amounts of phases are more effective at pinning the grain boundaries, thus delaying the reorientation in these 2024 powders.

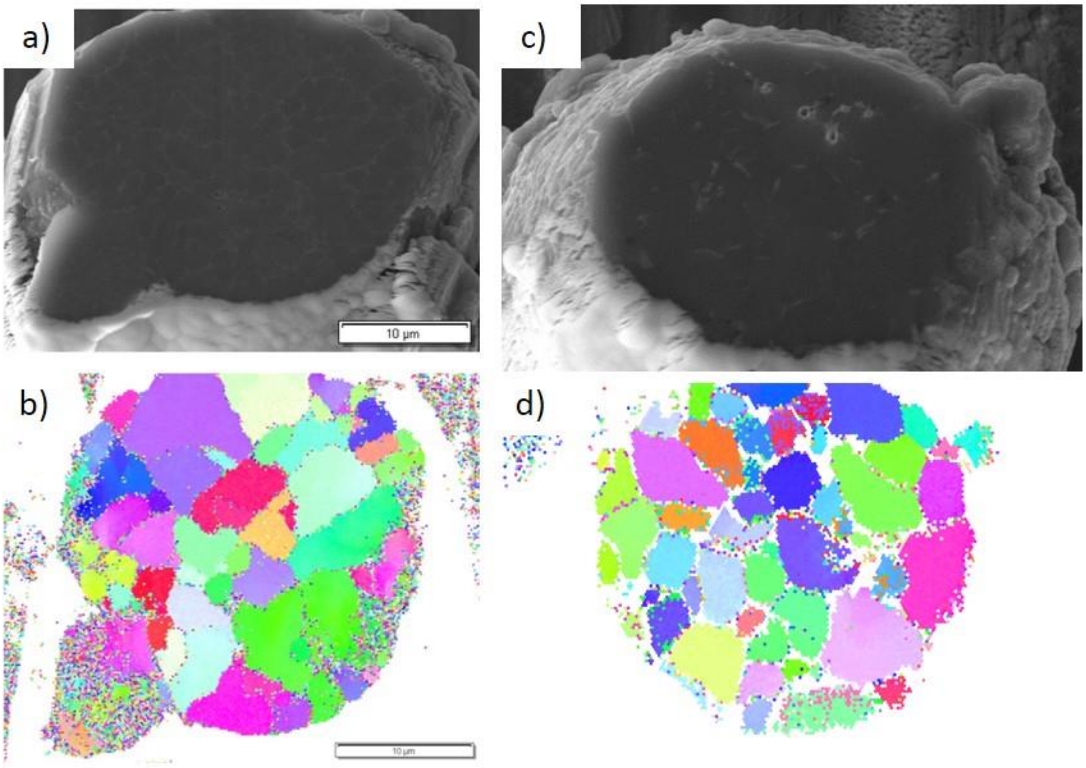

Figure 4. 4a. SEM micrograph of a powder particle in as-received condition, 4b. EBSD micrograph of a powder particle in as-received condition, 4c. SEM micrograph of a powder particle in 60 minute thermally treated condition, 4d. EBSD micrograph of a powder particle in 60 minute thermally treated condition.

5.4.1.3 TEM

TEM was used to evaluate the internal microstructure of the powder. Figure 5 shows low magnification micrographs of the lamella from a powder particle for a) as-received and b) thermally treated for 1 hour at 490 °C. It shows similar features as those seen in the SEM micrographs (Figure 2), however, finer precipitates in the thermally treated sample are now resolvable. Image thresholding was also performed on these micrographs, and the results are displayed as bars on Figure 3. Note the agreement between the values calculated by different the different electron microscopy techniques.

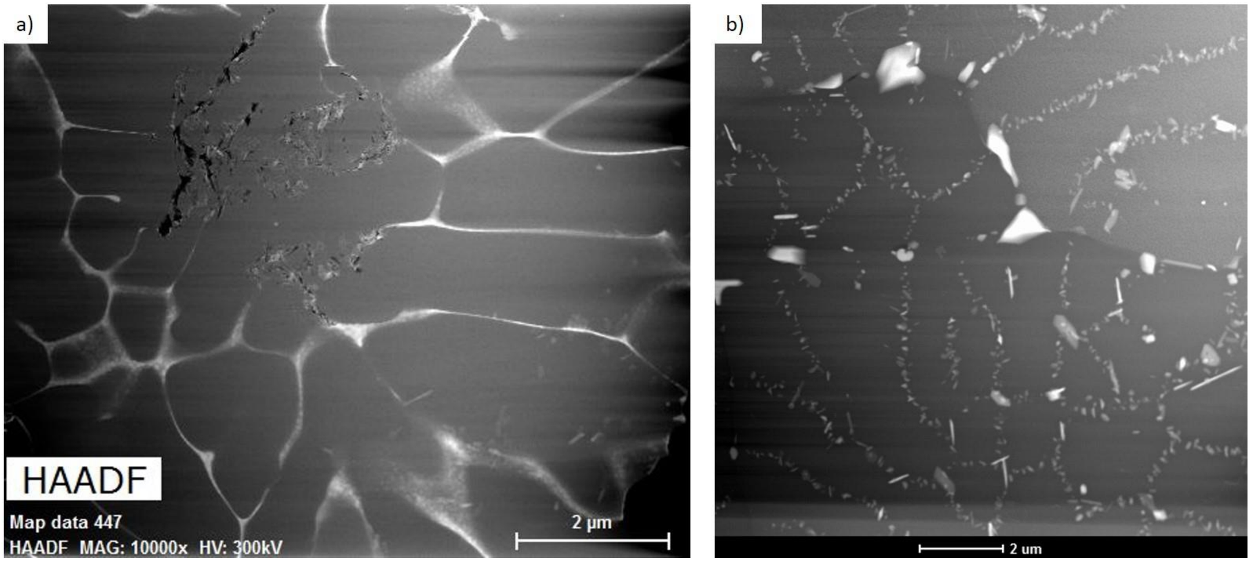

Figure 5. Low magnification HAADF images of powder Al 2024 a) in the as-received condition and b) after a 60 minute thermal treatment.

Figure 6 shows high magnification representative microstructures of the as-received condition with elemental EDS maps. In the SEM micrographs, the secondary phases at the boundaries appear to be a single continuous phase, however, in the HAADF images in Figure 6, it can be seen that two phases exist at the boundary. The elemental maps in Figure 6 show that one phase consists of Cu, Mg, and Si, and the second, a discrete phase, consists of Cu, Fe, and Mn. Further investigation using EDS point quantification analysis revealed these phases to be S-phase with trace amounts of Si and Al_2Cu with trace amounts of Fe and Mn, respectively. During rapid solidification there is solute microsegration of the alloying elements at the boundaries. This segregation is highly unstable with a high propensity for the formation of secondary phases. Thus, the S-phase and Al_2Cu form rapidly while the Fe and Mn have no time to diffuse. Based on literature data compiled in the Thermo-Calc databases, it is known that Fe and Mn are soluble in Al_2Cu.

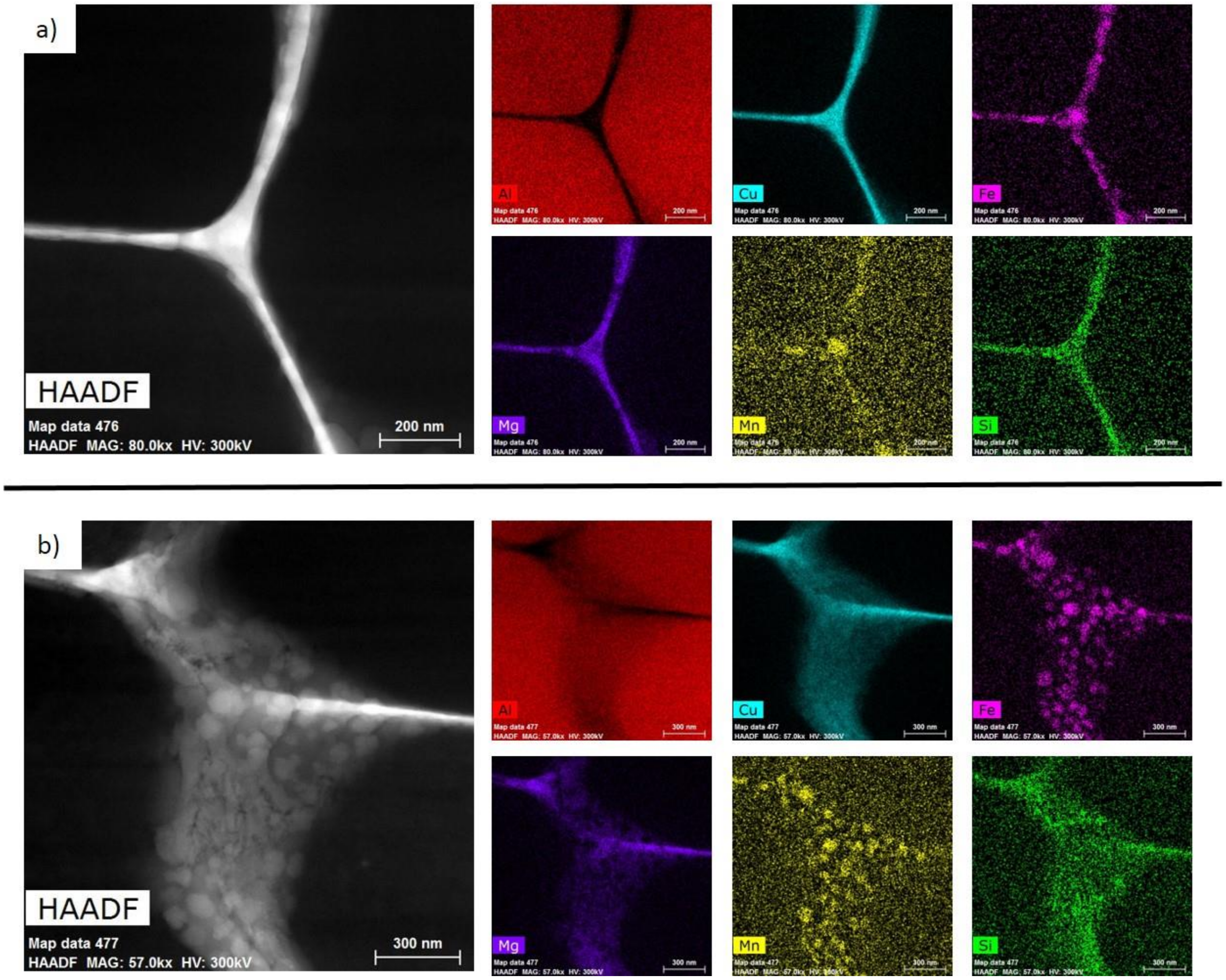

Figure 6a,b. TEM HAADF images of the as-atomized powder grain boundary phases for two different cross-sections demonstrating the network of S-Phase and the dispersed Al_2Cu within the phase.

The two phases have an intertwined morphology. S-phase forms a network-structure at the sub-grain boundaries, while Al_2Cu forms as discs in or on the network. Little to no precipitation is seen in the bulk of the sub-grains, though considering the small size of the sub-grains and subsequent short diffusion distance to a boundary, this is an expected observation.

Given the rapidly solidified nature of the powders and the non-equilibrium conditions, it is expected that the as-received microstructure would follow Scheil solidification. Based on the Scheil solidification model in Thermo-Calc (Figure 1b), the two most abundant phases predicated are S-phase and Al_2Cu. As this is consistent with the results from the experimental, it validates the applicability of the Scheil solidification model this rapidly solidified powder.

Figure 7 shows high magnification of representative microstructures of the 60 minute thermally treated condition with elemental EDS maps. In SEM micrographs, both large and small discrete secondary phases can be seen at the boundaries. This is similar to what is seen in the TEM in the HAADF images in Figure 7, however in the TEM it is possible to resolve even smaller phases. Based on the size distributions of these phases, it is hypothesized that there are two different phases. The elemental maps in Figure 7 show that two phases do exist, one consisting of Al and Cu, and the other consisting of Al, Cu, Fe, and Mn. Further investigation using EDS point quantification analysis revealed these phases to be Al_2Cu and Al_6Mn with trace amounts of Cu and Fe; additionally, small amounts of $Al_{28}Cu_4Mn_7$ were identified. The Al_2Cu has a plate-like morphology, the Al_6Mn a short rod morphology, and the $Al_{28}Cu_4Mn_7$ a small plate morphology. While Al_2Cu is present in both the as-received and thermally treated conditions, there are differences in both the composition and morphology.

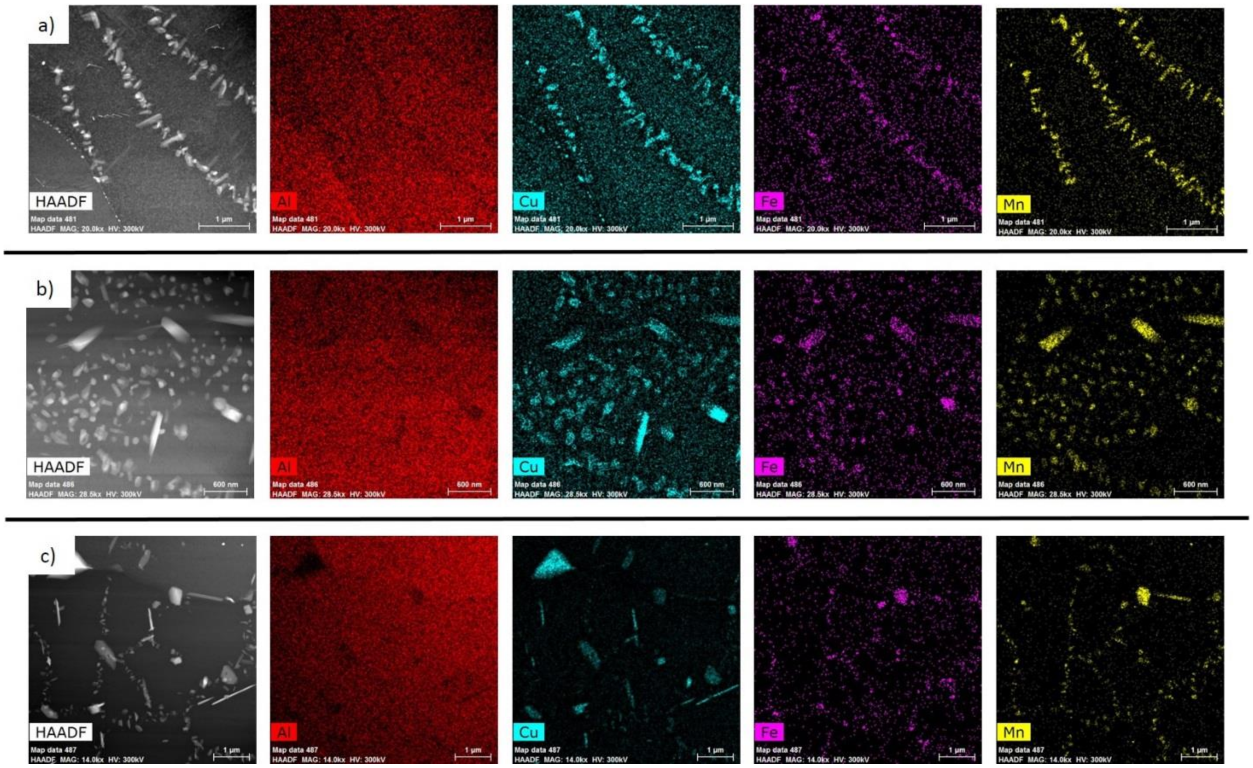

Figure 7a,b,c. TEM HAADF of internal microstructure of 60 minute treated condition powder demonstrating Al_2Cu and Al_6Mn secondary phases.

As seen in Figure 1a, S-phase has a dissolution temperature above than the treatment temperature, as does Al_2Cu; this does not agree with what was seen experimentally. Additionally, Figure 1a predicts the presence of the $Al_{15}Si_2Mn_4$ phase, which again is in disagreement with the experimental results. To further understand the phase transformation in this system, the model was calibrated to the experimental results by suppressing the $Al_{15}Si_2Mn_4$ phase in the simulation. The resultant equilibrium diagram is shown in Figure 8a. Figure 8b shows an increased magnification of Figure 8a and Figure 8c shows an increased magnification of the original diagram (Figure 1a) for comparison. Figure 8b shows that when $Al_{15}Si_2Mn_4$ is not present, a change in the stability of the other phases occurs; S-phase will completely dissolve at 490 °C, Al_2Cu remains stable until 502 °C, and $Al_{28}Cu_4Mn_7$ will now begin to form at 480 °C. Given these changes, the model now predicts the phases present in the powder. During thermal treatment, the boundary network S-phase dissolves, leaving a concentration of Al, Cu, Mg, and Si at the boundaries. Additionally, the Fe and Mn that was dissolved in the Al_2Cu in the as-received condition diffuses out of the Al_2Cu into the matrix, adds additional Fe and Mn concentrations at the boundary. This high concentration of Al, Cu, Fe, and Mn leads to the formation of Al_6Mn, as this is the next thermodynamically stable phase. The added thermal energy enables the growth of Al_2Cu from 50-100 nm-sized discs to 400-800 nm-sized plates.

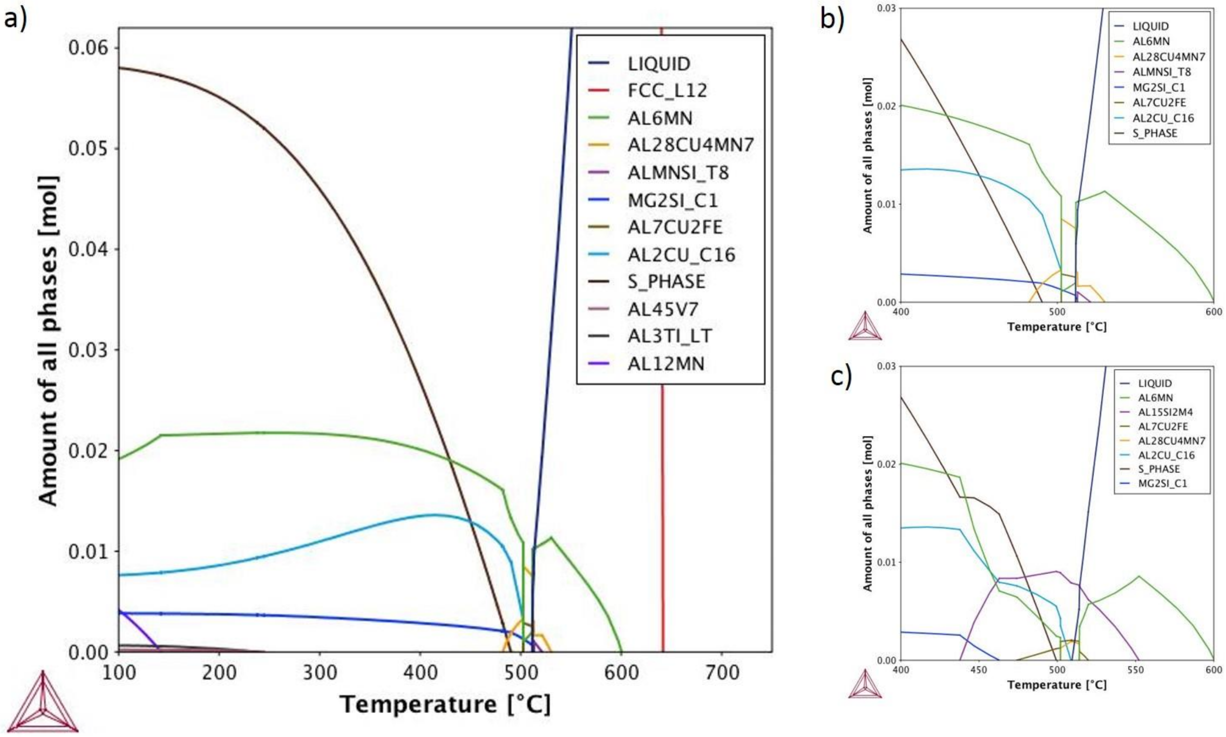

Figure 8. Phase diagrams predicted using Thermo-Calc a) with $Al_{15}Si_2Mn_4$ suppressed, b) increased magnification of (a), and c) increased magnification of Figure 1b.

5.4.2 Differential Scanning Calorimeter

TEM sample preparation can be time consuming and only yields insight into a small sample of the powder, thus it is important to utilize other, faster and more representative, analysis techniques to provide insight into a larger population of powder particles.

DSC was employed to evaluate the relative amount of secondary phases formed upon reheating solutionized specimens for various times at 490 °C. Figure 9a shows these scans while Figure 9b shows the enthalpy of the peak located around 300 °C. Note the difference in peak shape between the as-received condition and the various treatments but lack of difference in peak area as seen in the calculated enthalpies in Figure 9b.

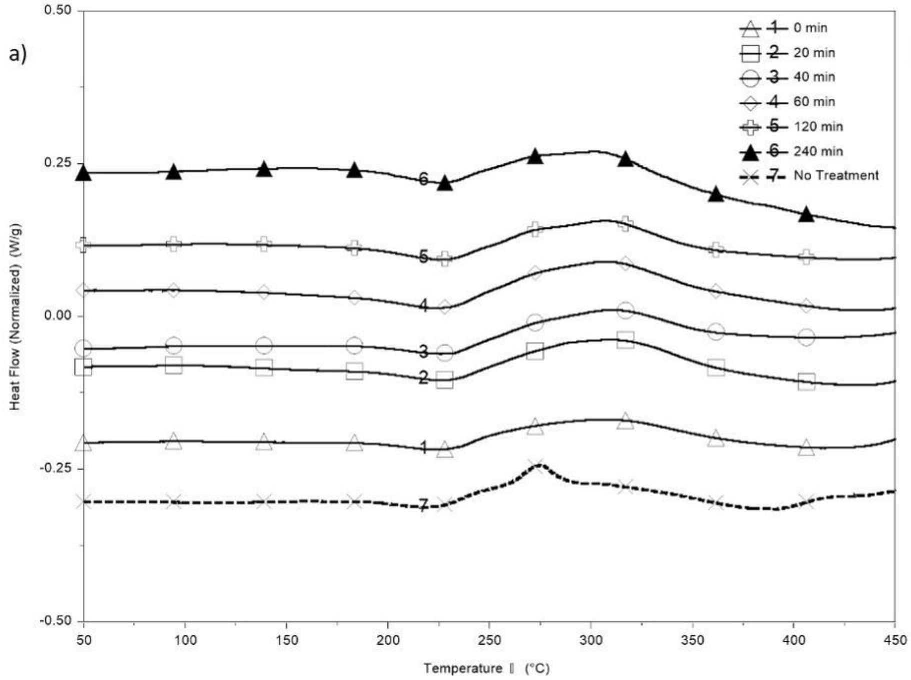

b)

Treatment	Enthalpy (J/g)
No Treatment	28
0 min	28
20 min	39
40 min	30
60 min	43
120 min	30
240 min	31

Figure 9. 9a. Normalized heat flow vs temperature (DSC) curves for each condition, 9b. Enthalpy of peak at 300°C for each condition.

The difference in thermogram shape indicates a difference in precipitation kinetics; the as-received condition has distinct peaks for what have been identified as the θ' and θ peaks whereas the solution treated conditions have a single peak in the same temperature range [12]. Despite the difference in peak shape, the enthalpy associated with the reaction in each thermally treated condition is similar, implying a similar degree of solid solution in each condition. However, this contradicts what was shown in the SEM micrographs and in Figure 3, both of which indicated differences in the secondary phases, and subsequently the degree of solid solution, of each condition.

The discrepancies between the two analysis techniques – DSC and electron microscopy – limits the convenience of DSC as a faster method for evaluating various treatment conditions. While the DSC thermograms show the changes in the Al_2Cu precipitate, consistent with TEM, they do not show the other intermetallics that are also present. Other research has shown that knowing exactly which intermetallics have formed is important for predicting the mechanical behavior of the final consolidated part.

5.5 Conclusion

A comparison of grain size measured via chemical etching and EBSD micrographs suggests that both granular and sub-granular structures are present in these powders. It was seen that there was no change in either the granular or sub-granular structure after thermal treatments due to boundary pinning by the secondary phases.

Electron microscopy revealed that the phases present in the as-received condition were found to be S-phase and Al_2Cu, which is consistent with non-equilibrium Scheil solidification predictions. Additionally, it was shown that at 490°C the S-phase dissolves and the remaining high elemental concentration forms Al_6Mn while the Al_2Cu grows from discs to plates. DSC results are consistent in showing the continued presence of Al_2Cu for the different treatment times.

The primary goal of a high temperature solutionization or homogenization treatment is to dissolve the secondary phases. Due to unique powder precipitation kinetics, this was not achieved in this study. SEM micrographs showed the thermal treatment to not have homogenized the microstructure. Rather, the thermal treatment transformed some phases, and TEM was necessary to identify the precipitation sequences with the aid of thermodynamic modeling. Future work evaluating other treatment temperatures is needed. It was shown here that, due to the higher percentage of grain boundary area acting as diffusion highways and the small grain sized leading to small diffusion distances to those highways, much shorter solutionization times will be needed for powders compared to their wrought counterparts.

5.6 Acknowledgements

This work was funded by the United States Army Research Laboratory, grant #W911NF-15-2-0024.

This work was performed in part at:

- The Kostas Advanced Nano-Characterization Facility in Kostas Research Institute at Northeastern University,
- The Center for Nanoscale Systems (CNS), a member of the National Nanotechnology Coordinated Infrastructure Network (NNCI), which is supported by the National Science Foundation under NSF award no. 1541959, and
- The University of Connecticut/Thermo Fisher Scientific Center for Advanced Microscopy and Materials Analysis.

5.7 References

1. V. Champagne and D. Helfritch, *Mater. Sci. Technol.*, 31, 627 (2015)
2. V. Champagne, A. Nardi and D. Cote, *Int. J. Powder Metall.*, 51, 37 (2015)
3. E. J. Lavernia, J. Ayers and T. S. Srivatsan, *Int. Mater. Rev.*, 37, 1 (1992)
4. V. Champagne and D. Helfritch, *Mater. Sci. Technol.*, 31, 627 (2015)
5. Sabard, A., de Villiers Lovelock, H.L. & Hussain, T. J Therm Spray Tech (2018) 27: 145. https://doi.org/10.1007/s11666-017-0662-2
6. Walde, C., Cote, D., Champagne, V., & Sisson, R. (2018). Characterizing the Effect of Thermal Processing on Feedstock Al Alloy Powder for Additive Manufacturing Applications. *Journal of Materials Engineering and Performance*, 1-10.
7. Rokni, M. R., C. A. Widener, and G. A. Crawford. "Microstructural evolution of 7075 Al gas atomized powder and high-pressure cold sprayed deposition." *Surface and Coatings Technology* 251 (2014): 254-263.

8. P. D. Eason, J. A. Fewkes, S. C. Kennett, T. J. Eden, K. Tello, M. J. Kaufman and M. Tiryakioğlu, *Mater. Sci. Eng., A*, 528, 8174 (2011)
9. S. C. Lee and K. T. Kim, *Int. J. Mech. Sci.*, 44, 1295 (2002)
10. K. Matsuki, T. Aida, T. Takeuchi, J. Kusui and K. Yokoe, *Acta Mater.*, 48, 2625 (2000)
11. V. Champagne: The cold spray materials deposition process: Fundamentals and applications, 1st ed. (Boca Raton, FL: CRC Press, 2007)
12. C. Badini, F. Marino and E. Verné, *Mater. Sci. Eng., A*, 191, 185 (1995)
13. ASTM E11-17, ASTM International, West Conshohocken, PA, 2017
14. ASTM E1097-12, ASTM International, West Conshohocken, PA, 2017
15. ASTM B209-14, ASTM International, West Conshohocken, PA, 2014
16. G.E. Totten, Hardening, Annealing, and Aging, *Handbook of Aluminum: Vol. 1: Physical Metallurgy and Processes*. (CRC Press, 2003), p. 123-195.
17. Ernst, Alexis, Mei Wei, and Mark Aindow. "FIB Milling strategies for TEM Sample Preparation of Spheroidal Powder Particles." *Microscopy and Microanalysis* 24.S1 (2018): 826-827.

6 Phase Identification of Mg-Rich Phases in Al 6061 Powder

Gas-Atomized Al 6061 Powder: Phase Identification and Evolution during Thermal Treatment

Kyle Tsaknopoulos[1], Caitlin Walde[1], Victor Champagne, Jr.[2], and Danielle Cote[1]

[1] Worcester Polytechnic Institute, Worcester, MA, 01609, USA
[2] US Army Research Laboratory, Aberdeen Proving Ground, MD 21005-5069, USA
Corresponding Author: Danielle Cote, dlcote2@wpi.edu

Accepted to JOM Special Edition: Aluminum: New Alloys and Heat Treatment

Online on October 11, 2018

https://doi.org/10.1007/s11837-018-3175-7

6.1 Abstract

Metal additive manufacturing processes often use gas atomized powder as feedstock; these processes use different methods for consolidation. Depending on the consolidation temperature, secondary phases may be retained during processing, making it important to understand powder microstructure prior to consolidation. Commercial alloy compositions are typically used for these powders because they have been widely studied and qualified, however the microstructure of the powder form of these compositions has not been studied. This paper aims to understand the commercial Al 6061 powder: how the internal microstructure of the powder differs from wrought both in the as-manufactured and thermally treated conditions. A specific focus is put on the Mg-rich phases and their morphologies. This was accomplished through transmission electron microscopy (TEM), scanning transmission electron microscopy (STEM), and energy dispersive x-ray spectroscopy (EDS). Both size and morphology of the phases in the powder differ greatly from those in wrought.

6.2 Introduction

Commercial alloy compositions are often used to create powders that are used for feedstock for many metal additive manufacturing processes. In doing so, additional material qualification for a new alloy can be avoided, making qualification for use more feasible. While these compositions have been widely studied in the wrought or cast form, limited work has been performed to analyze the microstructure of the powder form or these alloys.

Some metal additive manufacturing techniques use gas atomized Al alloy powders as feedstock. During the gas atomization process, liquid droplets undergo rapid solidification, experiencing cooling rates on the order of 10^4-10^{-5} °C/s [1]. This cooling rate is radically different that those experienced by similar alloys in a casting process, which are on the order of 10^{-1}-10^2°C/s, leading to different microstructures and resultant properties in powders as compared to their cast or wrought counterparts [1].

With research on wrought parts, the structure has been widely studied before and after various thermal treatments and mechanical processes [2]. However, at the advent of additive manufacturing, the focus was first on creating the process, then on optimizing the processing parameters for the consolidated part, and it is only in recent years that research has been conducted analyzing the effects of the feedstock on the consolidated parts [3-10].

Many metal additive manufacturing techniques that utilize powder as its feedstock employ melting as a means of consolidating the feedstock into a solid material. These processes use different methods to melt the feedstock, for example electron beams or lasers, which affects the melt pool temperature [11-12]. These differences in melt pool temperature can influence the microstructure. Many secondary phases can have extremely high melting points, higher than that of the matrix of the material, so even though the powder is melted, not all of the secondary phases may melt [2]. With this in mind, the secondary phases could remain in the melt pool, depending on the AM processing temperature (laser, e-beam, etc.), and thus be retained in the solidified consolidated structure.

Solid-state metal additive manufacturing (SS-MAM) techniques are gaining exposure because they do not have the severe cooling gradients seen in liquid-state manufacturing techniques. In these SS-MAM processes, the feedstock is not melted, and consequently the majority of features of the feedstock powder are retained or even improved upon during consolidation [13. With this in mind, it is important to understand the characteristics of the feedstock powder prior to use in solid state metal additive manufacturing processes, given that the rapidly solidified microstructure of the feedstock powders will carry over into the final consolidation.

To date, little research has been done to evaluate the properties and microstructure of rapidly solidified powders. Rokni et al. have performed some in-depth analysis of as-atomized aluminum powders. They analyze both the size distribution and shape, as well as the internal microstructure utilizing SEM, TEM, and EBSD. They report that gas atomized aluminum particles show surface grain features in the 1-4 μm range, with a similar structure internally accompanied by some solute segregation [3-6]. Additionally, they show that grains are typically equiaxed with some residual stresses [3].

As Rokni et al. show, the structure present in the powders is also present in the consolidated part. With this in mind, Sabard et al. apply a heat treatment to the as-atomized powders prior to use in cold spray consolidation [7]. They found that with a heat treatment of 4 hours at 450°C, particle deformation was enhanced, leading to improved particle-substrate bonding and thicker coatings. Additionally, they found that the thermally treated powders had a reduction in solute segregation and a higher porosity than the as-atomized condition. The authors also observed the formation of some needle-like precipitates in the thermally treated condition that were not present in the as-manufactured condition. The chosen treatment temperature is based on commercially used treatments for wrought components, and no work has been done to identify treatments specifically designed for powders.

Though Rokni et al. have performed extensive microstructural analysis of the as-atomized microstructure in relation to its presence in the consolidated structure, they, and others, have not identified the specific phases present in the as-atomized structure. Elsewhere, Adkins and Tsakiropoulos identified the major intermetallic present in their Al-Cr-Zr-Mn powders ($Al_{13}Cr_2$) but did not evaluate the range of possible phases [8]. Sabard et al. note that analysis in an SEM is not sufficient to identify phases present in gas atomized powder due to the low resolution [9]. Walde et al. evaluate the microstructural evolution of Al 6061 throughout a solution treatment, but only show trends in the Mg-rich and Fe-rich phases and do not identify phases [10]. Their microstructural evaluation utilizes scanning electron microscopy (SEM), but the interaction volume of the SEM beam limits the phase identification analysis possible.

Due to the smaller beam interaction volume, transmission electron microscopy (TEM), scanning transmission electron microscopy (STEM), and energy dispersive x-ray spectroscopy (EDS) in a TEM can more accurately identify the phases present beyond the current level of understanding. Fundamentally, this work employs TEM, STEM, and EDS-TEM to build upon the groundwork laid by Walde et al. in understanding the microstructures and secondary phases of gas atomized Al 6061 feedstock powders [10].

In wrought form, Al 6061 is a heat-treatable aluminum alloy with the primary strengthening sequence $\beta'' \rightarrow \beta' \rightarrow \beta$ (Mg_2Si), moving from needles, to rods, to equilibrium plates or cubes during treatment, respectively [14-15]. A typical heat treatment for this alloy consists of a solution treatment step to create a homogenous solid solution, a rapid quench to retain the metastable microstructure, an aging step to evenly precipitate uniformly sized strengthening phases, and an optional working step. It is important that the first step successfully reaches maximum solid solution in order to achieve an optimal distribution of precipitates during the following aging step [2]. Beta (Mg_2Si) is typically 25 µm to begin with, dissolve during treatment, then reform during aging at around 10 nm. These phases may or may not fully dissolve during treatment [16].

In summary, this work characterizes gas-atomized Al 6061 in both the as-manufactured and thermally treated conditions. Emphasis is given to identifying the phases present, more specifically the Mg-rich phases (the strengthening phase in the Al 6061 alloy) as they differ in morphology from those present in wrought counterparts. This is accomplished through extensive TEM analysis.

6.3 Method

6.3.1 Powder

For this research, gas atomized Al 6061 powder manufactured by Valiment, Inc. (Stockton, CA), was used. The initial batch was classified by size using a mechanical sieving method in compliance with ASTM E11 and divided into seven particle size categories. Size category 38-45um, was chosen for the analysis with d_{10} of 32 µm, d_{50} of 41 µm, and d_{90} of 54 µm. The chemical composition of this powder was found using direct current plasma emission spectroscopy (ASTM E1097-12) and is found in Table I and is in compliance with Al 6061 (ASTM B209) [17-18].

Table I: Al 6061 powder chemical composition analysis compared to ASTM B209

Element	Reviewed Powder	ASTM Standard[18]
	wt. %	wt. %
Magnesium	0.950	0.80-1.20
Silicon	0.490	0.40-0.80
Iron	0.270	< 0.70
Copper	0.250	0.15-0.40
Oxygen	0.100	---
Chromium	0.087	0.04-0.35
Zinc	0.035	< 0.25
Manganese	0.034	< 0.15
Titanium	0.024	< 0.15
Other	---	< 0.15
Aluminum	Remainder	Remainder

6.3.2 Modeling

The computational thermodynamic and kinetic modeling software, Thermo-Calc (Stockholm, Sweden) was used to provide insight into the secondary phases present with the given Al 6061 alloy composition as well as information about their stability at different treatment temperatures. The TCAL5 database was used to create an equilibrium diagram and non-equilibrium Scheil solidification diagram of the exact composition of the alloy under investigation for comparison with the powder microstructure.

6.3.3 Treatment

With the goal of creating a homogenous microstructure, a temperature of 530°C was chosen which allowed for dissolution of secondary phases without melting the powder [2]. The samples were treated for 60 minutes using a differential scanning calorimeter (DSC) (TA Instruments Discovery DSC with LN2P cooler) with a heating rate of 50°C/min to 530°C, held at temperature for 60 minutes and quenched at a rate of 120°C/min in a nitrogen environment [10].

6.3.4 Characterization

For TEM imaging, samples were created using a gallium focused ion beam (FIB) (FEI Helios 660 Nanolab and FEI Scios Dual Beam FIBs). Powder was distributed on carbon tape on an SEM stub for FIB sectioning. This was done by applying a protective Pt layer on the top surface of the chosen powder particle (approximately 40 µm X 1 µm X 1 µm). Material on either side of the Pt layer was then removed by milling perpendicular to the top surface of the Pt layer. This produced a parallel-sided slice of the powder particle. This slice was then lifted out and attached to a Mo omni-grid. Then it was thinned to a thickness of approximately 100nm with a final finish of 5kV to remove surface stresses. For elemental quantification analysis using EDS, thinner samples were needed to remove the interaction signal from other phases and the matrix behind the desired phase; smaller sections of the large sample were taken for further thinning for this analysis.

TEM and STEM images were taken using a Probe-corrected FEI Titan Themis 300 S/TEM with ChemiSTEM technology at an accelerating voltage of 300kV. EDS was completed using a Super-X EDS system at 300kV.

6.3.4.1 Image Analysis

In order to quantify the secondary phases present, the image analysis software Olympus Stream was used to segment the images using contrast differences between the phases and the matrix. Typical images of this analysis can be seen in Figure 1, which shows typical TEM images for both the as-manufactured and thermally treated samples. The Mg-rich phases contrast darker than the matrix in the TEM high-angle annular dark-field (HAADF) images while the Fe-rich phases are contrast lighter.

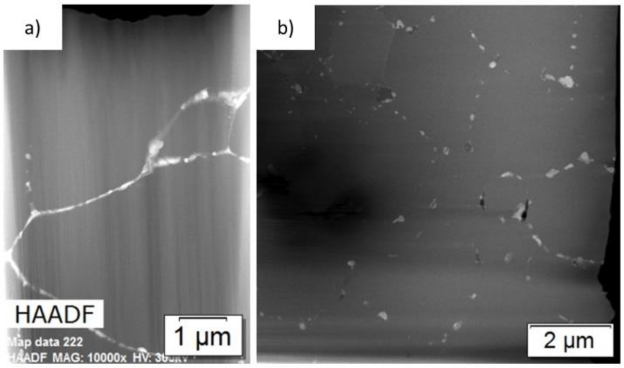

Fig. 1. Typical images used for secondary phase fraction analysis; a. TEM HAADF of as-manufactured Al 6061 particle lamella, b. TEM HAADF of thermally treated Al 6061 particle lamella

6.4 Results and Discussion

6.4.1 Modeling

The diagrams created in Thermo-Calc provide insight into which phases are expected given the alloy composition and serve as a starting point for phase identification in the powder microstructure. Figure 2a shows the equilibrium phases present in the Al 6061 composition as a function of temperature. This shows the stability of the different secondary phases, which is especially useful to know during thermal treatment. Since these powders are gas atomized, they are rapidly solidified and are thus not considered to be in an equilibrium state. Given that, it is expected that the phases present in the as-manufactured powder microstructure would more closely match that predicted by the Scheil solidification diagram, Figure 2b.

The equilibrium and non-equilibrium phases predicted by the Thermo-Calc models for as-manufactured and thermally treated conditions are compiled in Figure 2c. This demonstrates the predicted phases in the as-manufactured powder for rapid solidification (Scheil results), the phases expected if the initial powder were at equilibrium (Equilibrium results at 25°C), and the phases expected after thermal treatment of the powder (Equilibrium results at 530°C). The Scheil results predict the presence of $Al_{15}Si_2(Fe,Mn)_4$, Q(AlCuMgSi), $Al_{18}Fe_2Mg_7Si_{10}$,$AlSi_3Ti_2$, $Al_9Fe_2Si_2$, Al_8Fe_2Si, $Al_{13}Fe_4$ and Mg_2Si, in order of increasing abundance in the as-manufactured powder microstructure, with the most prominent phases being Mg_2Si and $Al_{13}Fe_4$. The Equilibrium results at 25°C predict the presence of Al_3Ti, $Al_{13}Fe_4$, $Al_{45}Cr_7$, $Al_9Fe_2Si_2$, T-Phase, and Mg_2Si in order of increasing abundance. Here the most prominent phases were $Al_9Fe_2Si_2$, T-Phase, and Mg_2Si. The Equilibrium results at 530°C show only the presence of $Al_9Fe_2Si_2$, as the previously mentioned phases are no longer stable at that temperature and will have dissolved back into the matrix.

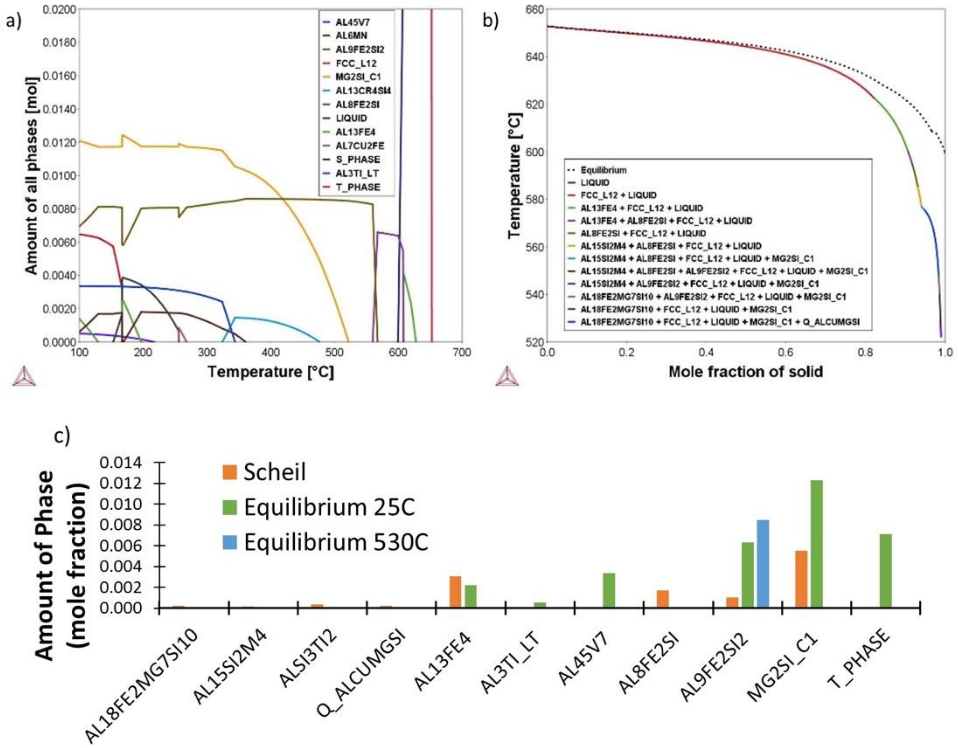

Fig. 2a. Equilibrium Diagram from Thermo-Calc software, b. Scheil Diagram from Thermo-Calc software, c. Amount of each possible phase as predicted by Thermo-Calc software at varying conditions.

These results can be used to determine the phases present in powder microstructure, but it is important to note that the data used to create the Thermo-Calc databases was taken from cast or wrought samples, rather than powder samples. Given this, it is possible that there are discrepancies between the powder microstructure and the predicted models as the kinetics for powders are significantly faster than their wrought counterparts due to their smaller size.

6.4.2 As-Manufactured Powder

Once sectioned and thinned, the samples were analyzed by TEM HAADF,EDS maps and EDS point quantifications. While thinner samples were specifically extracted to remove interaction effects from the matrix or overlapping phases, there were still many instances where the secondary phases were thinner than the lamella. This was taken into consideration during analysis of the point quantifications; if there is matrix behind the analyzed phase, the quantification will show a higher Mg content, as the matrix is richer in Mg than in Si. Alternatively, if there is an Fe-rich phase behind the analyzed phase, the quantification will show a lower Mg content, as the Fe-rich phases contain more Si than Mg. With this in mind, all of the Mg-rich phases were found to be Mg_2Si with varying morphologies.

Figure 3 displays images of as-manufactured powder. Figure 3a shows an SEM image of an as-manufactured powder particle. The channeling contrast reveals clusters of similarly oriented sub-grains with phases at the sub-grain boundaries, consistent with what is reported in the literature for powders [3-10]. Figure 3b shows a low-magnification TEM-HAADF image of a similar sample. Figure 3c shows a higher magnification TEM-HAADF image of an as-manufactured sample. Note the continuous nature of the phases at the sub-grain boundaries. These, and similar microstructures, were analyzed in the image analysis software to determine the phase fraction of the secondary phases. It was found that there was 1.62% (area) Mg_2Si and 3.42% (area) Fe-rich phases present in the as-manufactured samples.

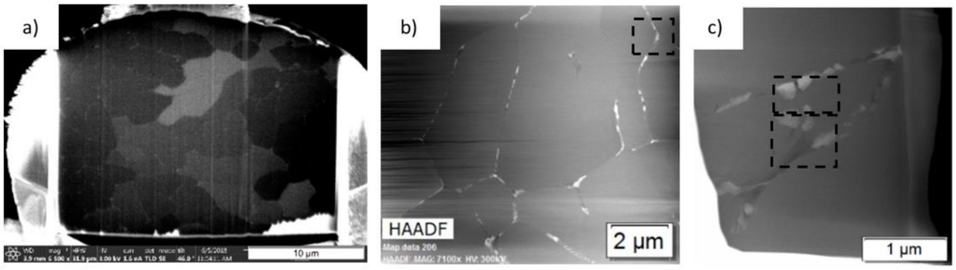

Fig. 3. Overview images of as-manufactured Al 6061; a. SEM, b. TEM HAADF, c. increased magnification HAADF from b. Outlined regions show where further analysis will be highlighted.

Additionally, EDS point analysis quantification was performed at multiple points at the subgrain interiors to determine the matrix composition. The average matrix composition was found to have 97.56 wt% Al, 1.16 wt% Mg, 0.04 wt% Fe, and 0.02 wt% Si with trace amounts of the remaining elements. The solubility limit of Mg in Al is less than 0.5 wt% at room temperature [19]. This demonstrates that the Mg composition in the Al matrix in these powders is higher than the solubility limit. This confirms the super saturated nature of the powders due to rapid solidification.

Figure 4 shows a HAADF micrograph of a triple point boundary with elemental EDS maps for Al, Cu, Fe, Mg, and Si. Figure 4g shows the highlighted region of Figure 4a magnified, where the atomic lattice of the precipitate can be seen as incoherent with that of the matrix. From the elemental maps, it can be concluded that this is a rod-like Mg_2Si particle with an Fe-rich phase surrounding it. This morphology appears to be unique to powders. The composition from point analysis combined with the incoherent nature of the phase boundary indicates the phase is Mg_2Si and not a metastable precursor.

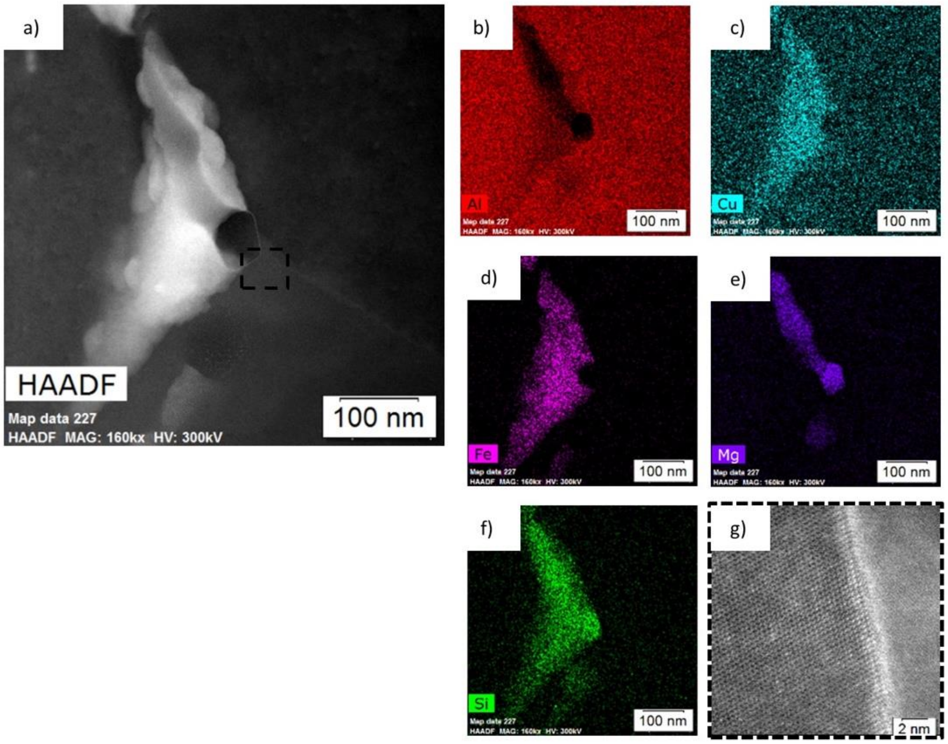

Fig. 4a. HAADF image of a triple point in as-manufactured Al 6061; elemental EDS maps for b. Al, c. Cu, d. Fe, e. Mg, f. Si. g. High magnification HAADF if highlighted region in a.

Figures 5a-f shows a HAADF image of Mg_2Si and Fe-rich particles along a grain boundary, along with elemental EDS maps for Al, Cu, Fe, Mg, and Si. It can be seen that Si is present in both the Mg- and Fe-rich phases. These have different morphologies than the Mg_2Si and Fe-rich phase in Figure 4.

Figures 5g-m shows a HAADF image of Mg_2Si and Fe-rich phases in a lamellar structure along a boundary. This microstructure is consistent with that of cellular precipitation, which is more likely to be the mechanism of precipitation in non-equilibrium systems. This morphology of Mg_2Si is particularly different than seen in castings. A perpendicular view of the cellular precipitates can be seen in Figures 5a-f.

Figures 5n-t shows a HAADF image of Mg_2Si in another cellular structure with the Al-matrix, along with elemental EDS maps for Al, Cu, Fe, Mg, and Si. Here, there is no Fe-rich phase interacting with the Mg_2Si, so this is yet another unique morphology.

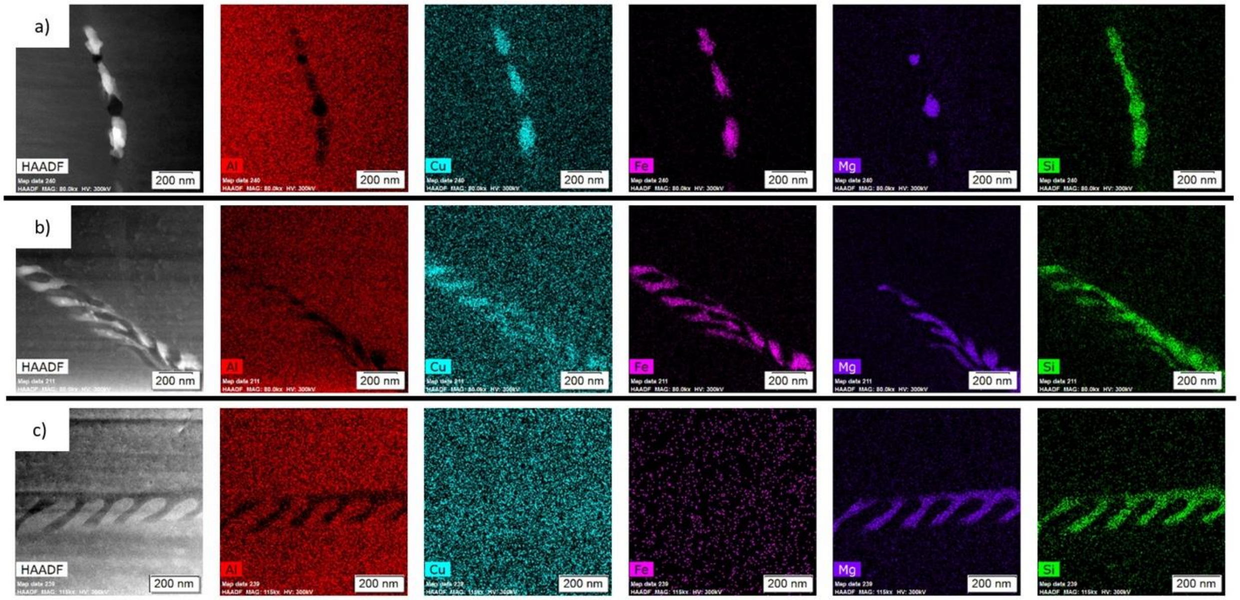

Fig. 5. Elemental EDS maps and HAADF images of Mg-rich phases at a boundary in as-manufactured Al 6061; a. alternating Mg2si and Fe-rich phases (left to right: HAADF image, Al, Cu, Fe, Mg, Si), b. alternating Mg2si and Fe-rich phases in a different orientation (left to right: HAADF image, Al, Cu, Fe, Mg, Si), c. unique Mg2si morphology at a boundary phases (left to right: HAADF image, Al, Cu, Fe, Mg, Si).

Figure 6 shows additional morphologies of the Mg_2Si (dark-contrasting phase) present in the as-manufactured powders at various magnifications. All of the unique morphologies seen in the as-manufactured powders can be attributed to the rapidly-solidified, non-equilibrium structure.

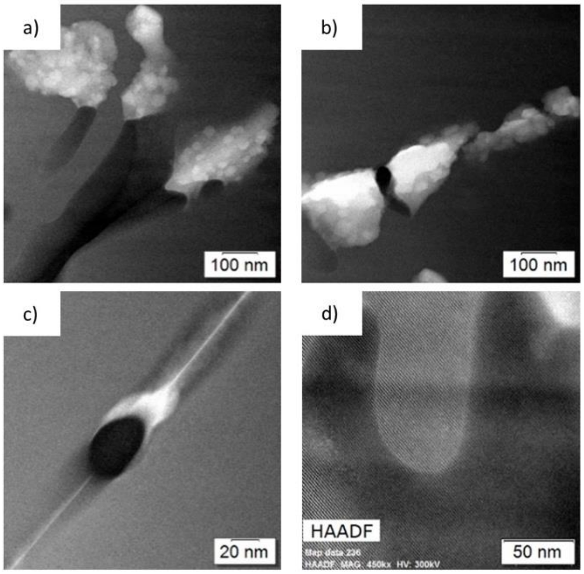

Fig. 6. Additional morphologies of Mg2Si in as-manufactured Al 6061. a. Fe-rich phase on Mg_2Si, b. alternating Fe-rich and Mg_2Si on a boundary, c. Mg_2Si on a boundary, d. atypical Mg_2Si morphology.

The thermodynamic and kinetic models in Figure 2 predict that other Mg-containing phases should be present in the as-manufactured condition, however, Mg_2Si is the only Mg-rich phase seen in these gas atomized Al 6061 powders. The discrepancy stems from the models being created using data for wrought conditions. This further emphasizes the need to understand powders in both models and experiments.

6.4.3 Thermally Treated Powder

Figure 7a shows an SEM image of a thermally treated powder particle. Figure 7b shows a low-magnification TEM image of a similar sample. Figure 7c shows a higher magnification TEM image of a thermally treated sample. Note the discrete phases, in contrast to the continuous nature of the phases present in the as-manufactured sample. This structure is consistent with what is reported in the literature for powders [3-10].

Additionally, note the qualitative decrease in the dark-contrasting Mg_2Si. These, and similar micrographs, were used in the image analysis software to determine the phase fraction of the Mg_2Si. It was found that there was 0.81% (area) Mg_2Si, a decrease from the as-manufactured samples, and 4.4% (area) Fe-rich phases, an increase from the as-manufactured sample.

Figure 7d-e shows examples of two Mg_2Si morphologies in the thermally treated condition. Figure 7d shows an Mg_2Si particle at a prior triple point, while Figure 7e shows a much smaller Mg_2Si particle with an Fe-rich phase. Based on Figure 2, all Mg_2Si should dissolve at the treatment temperature. It is hypothesized that the Mg_2Si at the triple points spheroidizes to a more equilibrium plate-like shape prior to dissolving, while Mg_2Si on the grain boundaries dissolves. The point quantification analysis, along with the semi-coherent atomic lattice structure seen in Figure 7d, indicates these phases are Mg_2Si rather than a metastable precursor.

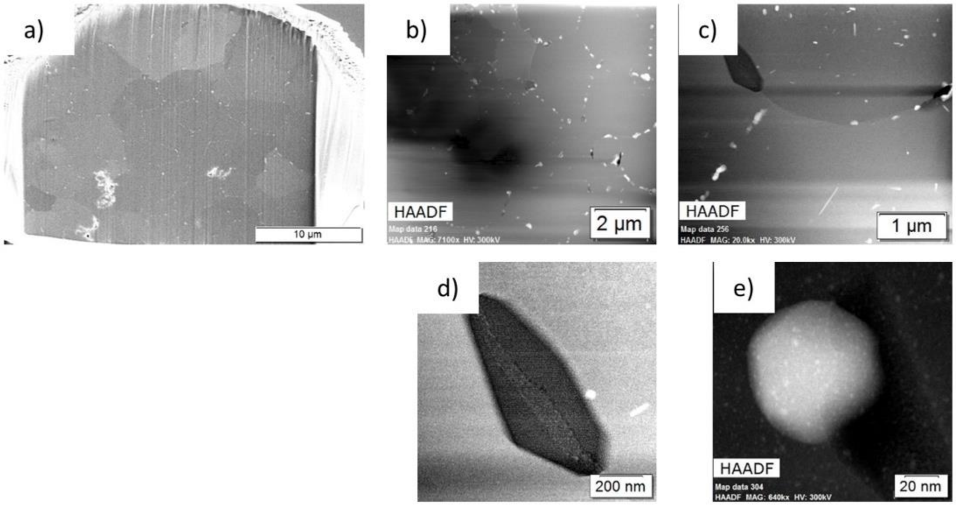

Fig. 7. Overview images of thermally treated Al 6061; a. SEM, b. TEM HAADF, c. increased magnification HAADF of similar sample, d. Mg2Si of plate-like morphology, e. Mg2Si dissolving.

A longer treatment time is necessary to fully dissolve all the Mg_2Si and reach the equilibrium structure predicted by Figure 2a. However, it has been shown in SEM studies that the Fe-rich phases continue to grow, and thus results in a more heterogeneous microstructure [10]. Treatment times must be optimized for each application, depending upon whether the goal is a homogenous microstructure or the complete dissolution of Mg_2Si. Fe-rich phases tend to act as nucleation sites for cracks and have been known to cause poor wear properties, however at least partially-solutionizing the powder has been shown to increase ductility during the solid state metal additive manufacturing process cold spray [4, 20]. It has been hypothesized that the Fe-rich phases control the mechanical properties of this powder, but given the amount of different types of Fe-rich phases predicted by Figure 2, and the fact that model predictions were inaccurate for Mg_2Si, identification of the Fe-rich phases is an extensive study that will be reported separately [10].

The thermodynamic and kinetic models in Figure 2 predict the Mg_2Si should be fully dissolved at 530°C, however, some Mg_2Si is still present in these thermally treated gas atomized Al 6061 powders at this temperature. The discrepancy stems from the models being created using data for wrought conditions, and also the treatment time not being long enough to reach equilibrium. This further emphasizes the need to understand powders in both models and experiments.

Previous work done by Walde et al. reports phase fractions for the Mg- and Fe-rich phases in powders in the same conditions as studied here, however work is performed here in TEM rather than SEM [10]. Due to the smaller interaction volume, TEM can provide better insights into the amount of phases present than SEM, as some of the phases present are smaller than the interaction volume of the SEM beam, a limitation acknowledged by the authors. They report no measurable Mg-rich phases and 16% (area) Fe-rich phases in the as-manufactured powder, with less than 1% (area) Mg-rich phases and 4.5% (area) Fe-rich phases in the thermally treated powder. Both the numbers and trends vary greatly from the results reported here. This discrepancy is likely due to the limitations of the SEM beam as previously discussed; TEM analysis revealed many precipitates that are too small for an SEM to detect.

In general, the Mg_2Si seen in these powders varies in both size and morphology from what is reported in the literature for wrought Al 6061. In the literature for wrought 6xxx Al alloys, Mg_2Si is stated to exist as plates or cubes, with precursors β' and β" existing as rods and needles respectively. None of these structures are observed in the as-manufactured powder, and equilibrium plate-like Mg_2Si is seen in varying amounts in the thermally treated sample. Perhaps in shorter treatment time increments (20 min, 40 min) the metastable phases could be seen. In powders, the as-manufactured sample is smaller, and with the higher cooling rate during solidification, the grains are smaller. Because of this, the boundaries are smaller, which significantly limits the size of the precipitates, making those present in powder around 10 times smaller than those present in the wrought condition.

6.5 Conclusion

Through extensive TEM analysis, this work demonstrates how the internal microstructure of commercial alloy compositions in the powder form differ from those present in the wrought condition. Specific focus is given to the Mg_2Si phase in the as-manufactured and thermally treated conditions, as it is the primary strengthening phase in the Al 6061 alloy. It was shown that Al 6061 powder contains Mg_2Si of highly atypical morphologies in the as-manufactured condition. Once thermally treated, the smaller Mg_2Si precipitates dissolve and the larger ones spheroidize to the more equilibrium plate- or cube-like structures. This greatly differs from the microstructures seen in the wrought versions of the same commercial alloy composition and from the amounts of Mg_2Si predicted by thermodynamic and kinetic models.

There is opportunity for further optimization of the thermal treatment for individual applications; it is not possible to achieve a fully homogenous microstructure as the Fe-rich phases grow as the Mg_2Si dissolves. Identification of those Fe-rich phases will be needed to effectively optimize the thermal treatment parameters and will be reported elsewhere.

6.6 Acknowledgements

This work was funded by the United States Army Research Laboratory, grant #W911NF-15-2-0024.

This work was performed in part at the *Kostas Advanced Nano-Characterization Facility in Kostas Research Institute at Northeastern University* and at the *Center for Nanoscale Systems (CNS)*, a member of the National Nanotechnology Coordinated Infrastructure Network (NNCI), which is supported by the National Science Foundation under NSF award no. 1541959.

6.7 References

1. A. Mullis, L. Farrell, R. Cochrane, N. Adkins, *Metall. Trans. B*, 44, 992 (2013).
2. G.E. Totten, Hardening, Annealing, and Aging, *Handbook of Aluminum: Vol. 1: Physical Metallurgy and Processes*. (CRC Press, 2003), p. 259
3. Rokni, M. R., Widener, C. A. & Champagne, V. R. *J. Therm. Spray Technol.,* 23**,** 514 (2014).
4. Rokni, M. R., Widener, C. A., Champagne, V. K., Crawford, G. A. & Nutt, S. R. *Surf. Coatings Technol.,* 310**,** 278 (2017).
5. Rokni, M. R., Widener, C. A., Ozdemir, O. C. & Crawford, G. A. *Surf. Coatings Technol.,* 309**,** 641 (2017).
6. Rokni, M. R., Widener, C. A., Crawford, G. A. & West, M. K. *Mater. Sci. Eng. A,* 625, 19 (2015).
7. Sabard, A., de Villiers Lovelock, H. L. & Hussain, T. *J. Therm. Spray Technol.,* 1 (2017).
8. Adkins, N. J. E. & Tsakiropoulos, P. *Mater. Sci. Technol.,* 7**,** 334 (1991).

9. Sabard, A., de Villiers Lovelock, H. L. & Hussain, T. *J. Therm. Spray Technol.,* 27**,** 145 (2018).
10. C. Walde, D. Cote, V. Champagne, R. Sisson. *Journal of Materials Engineering and Performance*. (2018) https://doi.org/10.1007/s11665-018-3550-0
11. L. Sochalski-Kolbus, E. Payzant, P. Cornwell, T. Watkins, S. Babu, R. Dehoff, M. Lorenz, O. Ovchinnikova, C. Duty, Metall and Mat Trans A, 46, 1419 (2015).
12. G. Vastola, G. Zhang, Q. Pei, Y. Zhang, JOM, 68, 1370 (2016).
13. Champagne, V. K. *The cold spray materials deposition process : fundamentals and applications*. (Woodhead, 2007). p. 52
14. Chakrabarti, D. . & Laughlin, D. E. *Prog. Mater. Sci.,* 49, 389 (2004).
15. Matsuda, K. *et al. Mater. Sci. Eng. A,* 262, 232 (1999).
16. John E. Hatch, *Aluminum: properties and physical metallurgy*, 1st ed. (Metals Park, OH: American Society for Metals, 1984), pp. 71-103.
17. ASTM E1097-12 Standard Guide for Determination of Various Elements by Direct Current Plasma Atomic Emission Spectrometry, ASTM International, West Conshohocken, PA, 2012, https://doi.org/10.1520/E1097-12
18. ASTM B209-10 Standard Specification for Aluminum and Aluminum-Alloy Sheet and Plate, ASTM International, West Conshohocken, PA, 2010, https://doi.org/10.1520/B0209-10
19. Thermo-Calc Software TCAL5 Aluminum-based Alloys Database version 5 (accessed 15 August 2018).
20. Polanco Espezua, Sandro & Baptista, C & Ferreira Laurito, Denise & Antunes, Ana. *SAE Technical Papers*, 10.4271/2012-36-0520, (2012).

7 Phase Identification of Fe-Rich Phases in Al 6061

Evolution of Fe-rich Phases in Thermally Processed Aluminum 6061 Powders for AM Applications

Caitlin Walde[1], Kyle Tsaknopoulos[1], Derek Tsaknopoulos[1], Victor Champagne[2], Danielle Cote[1]*

[1]Worcester Polytechnic Institute, Worcester, MA
[2]US Army Research Laboratory, Aberdeen Proving Grounds, MD
*Corresponding author; dlcote2@wpi.edu

Under Review

Keywords

Aluminum, AM, powder, secondary phases,

7.1 Abstract

Gas atomized powders are frequently used in metal additive manufacturing processes (MAM). During consolidation, properties and microstructural features of the feedstock can be retained; features of interest that may be retained include the secondary phases. Al 6061 is a heat treatable alloy that is commonly available in powder form. While heat treatments of 6061 have been widely studied in wrought form, little work has been done to study the process in powders. This work investigates the evolution of the Fe-containing precipitates in gas atomized Al 6061 powder through the use of transmission electron microscopy (TEM) and energy dispersive x-ray spectroscopy (EDS). The as-atomized powders contained $Al_{13}Fe_4$ at the boundaries. After thermal treatment at 530 °C for one hour, concurrent dissolution of $Al_{13}Fe_4$ and formation of $Al_9Fe_2Si_2$ occurs.

7.2 Introduction

Many metal additive manufacturing (MAM) techniques utilize rapidly solidified powders as feedstock. In MAM, it is important to understand the feedstock microstructure prior to consolidation. Depending on the MAM process, certain aspects of the feedstock powder can be retained after consolidation and can affect the microstructure and properties of the final consolidated part. For example, in liquid-state MAM processes, such as selective laser melting (SLM) and thermal spray, features such as the porosity and oxide shell can be retained [1-3]. In addition to these, in solid-state MAM, the majority of the initial microstructural features – secondary phases, grain boundaries – are retained, though slightly to heavily deformed. A greater understanding of the process input – feedstock powders – can lead to a greater understanding of the process output – the final consolidated part. This is especially useful when considering models for these MAM processes.

Aluminum alloys are often used in aerospace and automotive applications for their combination of light weight, strength, toughness, ductility, and corrosion resistance. Some of these conventionally made parts are being replaced by those made with MAM due to a better optimization of strength and corrosion resistance [4].

6061 is an Al-Mg-Si age-hardenable alloy. It is used primarily for its strength, light weight, and economic appeal. Its most predominate phase is Mg_2Si (β) with precursors β'' and β' offering the most strengthening. A typical heat treatment for 6061 would include a solutionization step to supersaturate the matrix with solute for optimum precipitation in subsequent steps; a quench to retain the supersaturated matrix at lower temperatures; and an aging step to uniformly nucleate and grow β'' and β'[5]. Additionally, as with most Al alloys, 6061 contains a variety of Fe-rich intermetallics. This is due to the low solubility of Fe in Al [6]. These phases are AlFeSi-based and are brittle needles or platelets. Iron can form various phases, depending on the presence of other alloying elements. These phases include $Al_{12}(FeMn)_3Si$, Al_8Fe_2Si, $Al_{12}Fe_3Si$,

$Al_{15}Fe_3Si_2$, which form preferentially depending on the local composition [6-7]. They are the first phases to form from the liquid during solidification. Because of their high melting temperature they are difficult to dissolve during a homogenization or solutionization treatment [5-6].

In MAM, it has been shown that thermally treating the feedstock powder prior to consolidation can have an effect on the properties of the consolidated part [8-12]. Considering this, it is possible to alter the feedstock powder using heat treatments to optimize the properties of the consolidated part. However, it has been shown that, in powder form, Al 6061 does not behave as its wrought counterpart [13]. For example, Mg_2Si has unique morphologies in the powder form not seen in wrought Al 6061 [14]. Additionally, the small grain size of the powders, originating from their rapid solidification, decrease diffusion distance and therefore times, greatly accelerating diffusional processes. This becomes especially important to consider when evaluating thermal processing parameters for powders.

With the expectation that secondary phases in gas-atomized powders vary from their wrought counterparts, this work characterizes the AlFeSi intermetallics found in gas-atomized 6061 powders. Both the as-atomized and thermally treated conditions are considered. Characterization was performed using extensive transmission electron microscope (TEM) and energy dispersive spectroscopy (EDS) analysis.

7.3 Materials and Method

Commercially available gas atomized Al 6061 powder (Valimet, Inc., Stockton, CA) was used in this study. The powder was mechanically sieved using laboratory test sieves compliant with ASTM E11 to aid in repeatability of selecting similarly sized powder particles for analysis; the final classification had d_{10} of 32 µm, d_{50} of 41 µm, and d_{90} of 54 µm [15]. Direct current plasma emission spectroscopy was used to determine the elemental composition of the powders (Table 1); the composition is in compliance with the standard for Al 6061 alloys [16-17].

Table 1: Elemental composition of studied powder and ASTM Standard

Element	Studied Powder	ASTM B209 [17]
	wt. %	wt. %
Magnesium	0.950	0.80-1.20
Silicon	0.490	0.40-0.80
Iron	0.270	< 0.70
Copper	0.250	0.15-0.40
Oxygen	0.100	---
Chromium	0.087	0.04-0.35
Zinc	0.035	< 0.25
Manganese	0.034	< 0.15
Titanium	0.024	< 0.15
Other	---	< 0.15
Aluminum	Remainder	Remainder

Simulations were performed using computational thermodynamic and kinetic modeling software (Thermo-Calc, Stockholm, Sweden) with the exact elemental composition of the sample to predict the secondary phases and their stability. Both equilibrium and Scheil solidification diagrams were created using the TCAL5 database.

Powder was studied in two conditions; as-atomized and thermally treated. The thermally treated samples were treated at 530 °C for 1 hour to create a homogenous microstructure. Treatment was performed in a differential scanning calorimeter (DSC) (TA Instruments, New Castle, DE) with a heating rate of 50 °C/min and cooling rate of 120 °C/min in a nitrogen environment.

Samples were mounted in epoxy and prepared for analysis via mechanical grinding and polishing with a final polish using 0.05 µm colloidal silica. Samples were then characterized using a tungsten-source SEM (Zeiss EVO MA10) at an accelerating voltage of 10 kV. Both secondary and backscatter detectors were used.

Samples were characterized using a probe-corrected TEM (Titan Themis with ChemiSTEM, ThermoFisher Scientific, Waltham, MA) and energy dispersive X-Ray spectroscopy (EDS) (Super-X, ThermoFisher Scientific, Waltham, MA) at an accelerating voltage of 300 kV. Samples were prepared for TEM analysis using a gallium focused ion beam (FIB) (Helios 660 Nanolab, ThermoFisher Scientific, Waltham, MA). Parallel-sided lamella were lifted-out from powder particle cross-sections and attached to a Mo Omni-grid. Samples were then thinned to a thickness of less than 100 nm, using an ion beam of 5 kV as the final step to minimize surface stresses.

The secondary phases were quantified by segmenting the TEM high-angle annular dark-field (HAADF) images using image analysis software (Stream, Olympus Corporation, Tokyo, Japan). In the HAADF image, the Fe-rich phases contrast as lighter than the matrix while the Mg-rich phases contrast darker.

7.4 Results and Discussion

Figure 1 shows cross sections of a) the as-atomized condition and b) the thermally treated condition taken using a backscatter electron (BSE) detector. In both, the light-contrasting regions correspond to the Fe-rich phases whereas the dark contrasting regions are either Mg_2Si or porosity; the difference between the Mg_2Si and the pores can be determined through a combination of EDS mapping and secondary electron micrographs. In the as-atomized condition, Fe-rich phases decorate the sub-grain boundaries completely, with small Mg_2Si primarily at the grain corners. This is typical of other gas-atomized Al 6061 powders that have been analyzed in literature [8, 13-14]. In the thermally treated condition, the Fe-rich phases behave in two ways: those in the network structure partially dissolve, while the discrete phases spherodize. Similarly, the Mg_2Si phase also exhibits two different behaviors: some dissolve and disappear while others grow and stabilize. Additionally, there is an increase in porosity in the thermally treated condition; this effect has been reported in other gas-atomized Al alloys as well as in Al 6061 [8, 12-14]. In both conditions, there is no nucleation in the bulk of the grain. Attempts to identify these phases in gas-atomized powders using SEM have been made; Bedard et al. [18] reduce the options from "Fe-rich" phases to, more specifically, an Fe-Si-Al phase, while Walde et al. [13] propose that $Al_{45}Cr_7$, $Al_6(Fe,Mn)$, $Al_{13}Fe_4$, $Al_9Fe_2Si_2$, and Mg_2Si are present in the as-atomized condition and that the $Al_{45}Cr_7$, $Al_6(Fe,Mn)$, $Al_{13}Fe_4$, and Mg_2Si dissolve after thermal treatment while the $Al_9Fe_2Si_2$ grows. However, it is widely acknowledged that the interaction volume of an SEM beam is insufficiently small to accurately identify phases of this size. Thus, TEM has been employed to further study the microstructural evolution. The equilibrium phases present in bulk Al 6061 are typically $Al_{12}(FeMn)_3Si$, Al_8Fe_2Si, $Al_{12}Fe_3Si$, $Al_{15}Fe_3Si_2$, though in gas-atomized powders the non-equilibrium phases dominate due to the rapid solidification [6-7, 13].

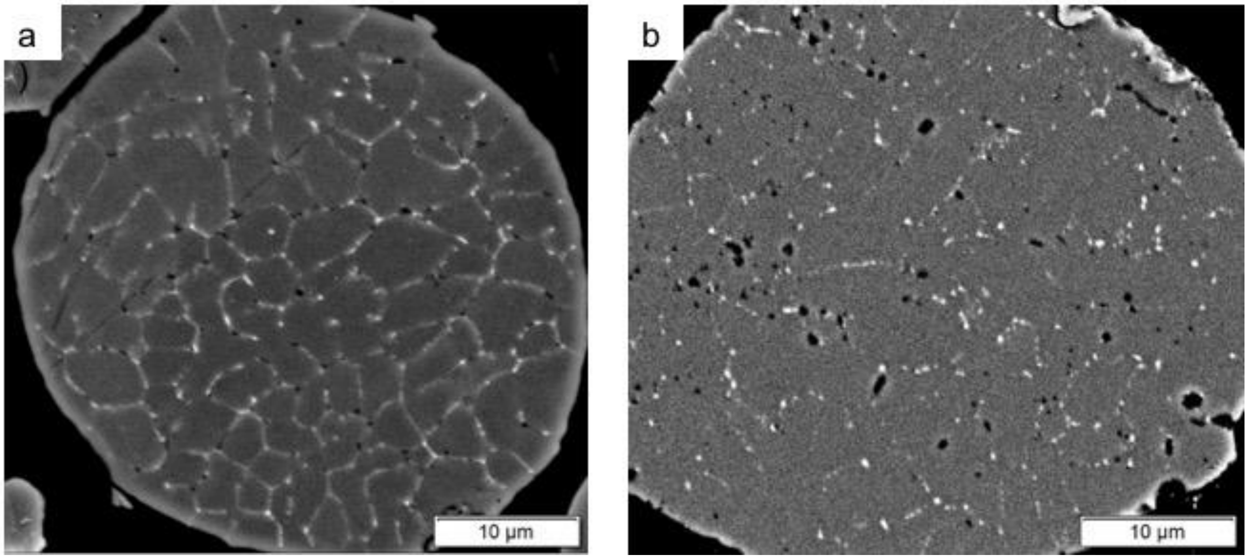

Figure 1: BSE images of cross sections of a) the as-atomized powder and b) the thermally treated powder.

Figure 2 shows a HAADF image and overview EDS maps of the as-atomized condition using TEM. Note that what appeared to be a continuous network structure at the boundaries in SEM micrographs is actually comprised of discrete Fe-rich phases and small Mg_2Si. The EDS here confirms that the Fe-rich phase is an Fe-Si-Al phase. Additionally, these micrographs confirm that there are no secondary phases in the bulk of the grains.

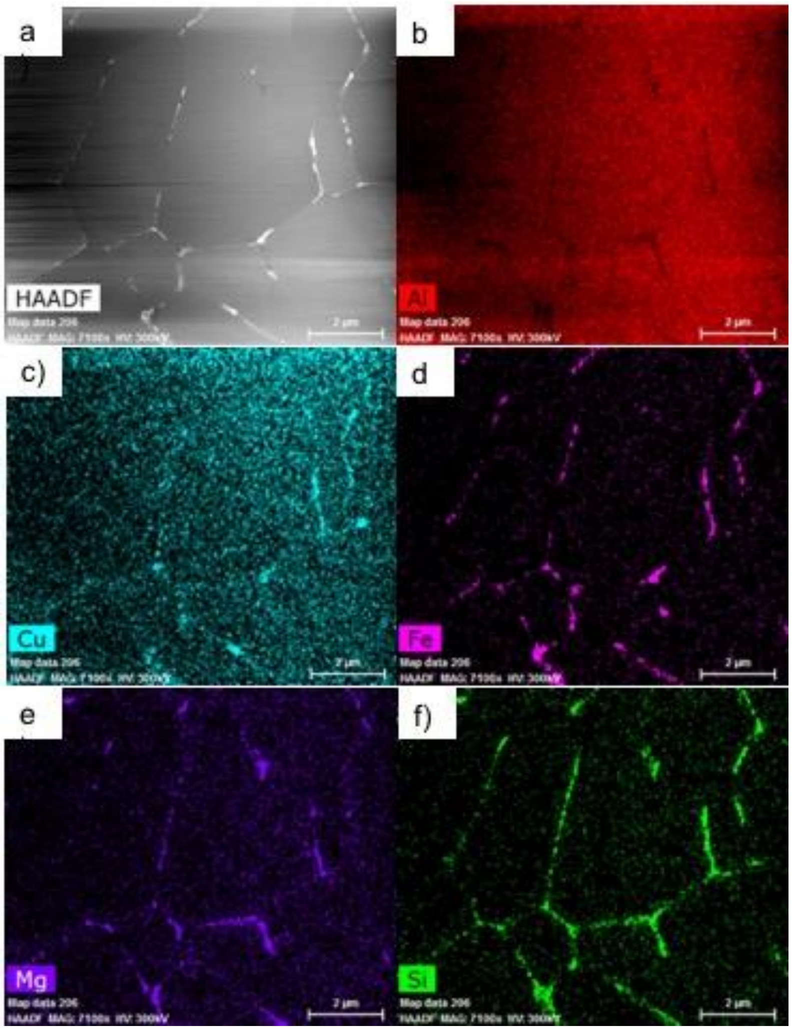

Figure 2: Overview images of the as-atomized powder: a) HAADF, and EDS maps of b) Al, c) Cu, d) Fe, e) Mg, and f) Si.

Figure 3 shows a higher magnification HAADF and EDS maps of a boundary in the as-atomized condition. Note how the Fe-rich phases and Mg_2Si are intertwined within the network of boundaries. Figure 4 shows a higher magnification HAADF image of a triple point in the as-atomized condition. Again, it can be seen that the Fe-rich phases and Mg_2Si are intertwined with one another. EDS here further confirms that the Fe-rich phase is an Fe-Si-Al phase. Point EDS quantification of the Fe-rich phase reveals it to be $Al_{13}Fe_4$ of various morphologies. As reported in literature and predicted by the thermodynamic and kinetic simulations (Thermo-Calc), $Al_{13}Fe_4$ can contain Cu, Mn, Si, and Zn in addition to the Al and Fe (Table 2).

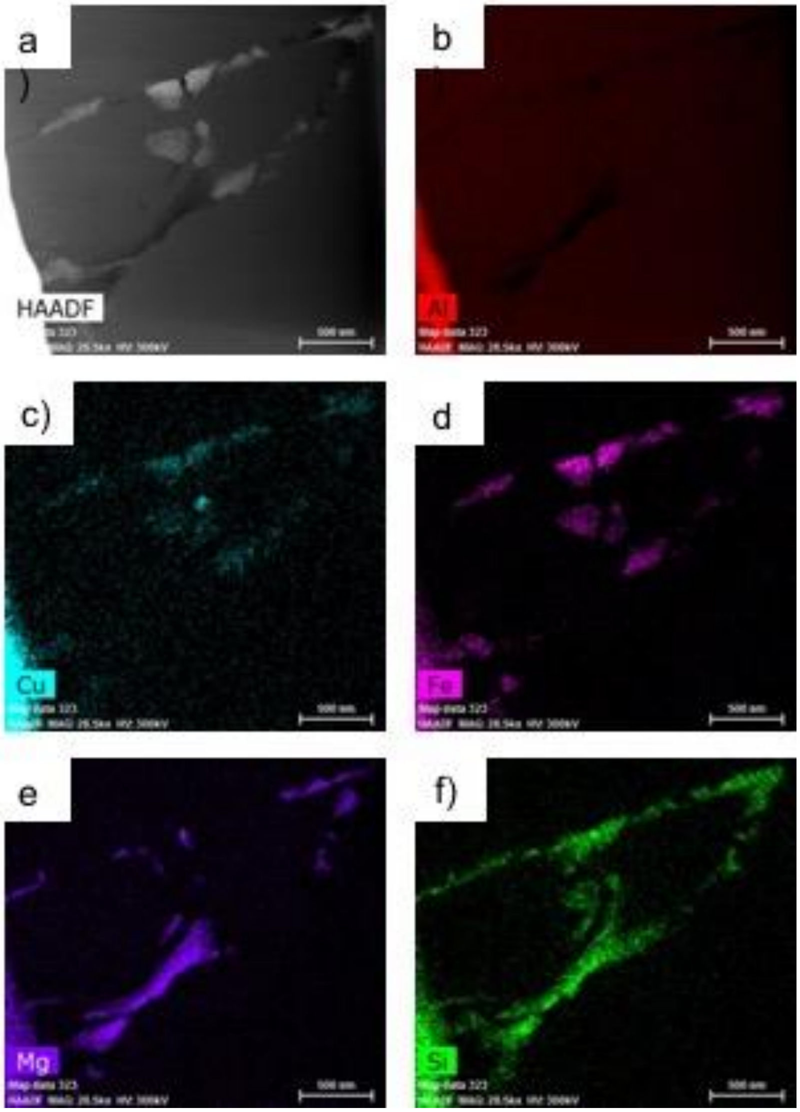

Figure 3: Higher magnification a) HAADF, and EDS maps of b) Al, c) Cu, d) Fe, e) Mg, and f) Si of a boundary in the as-atomized powder.

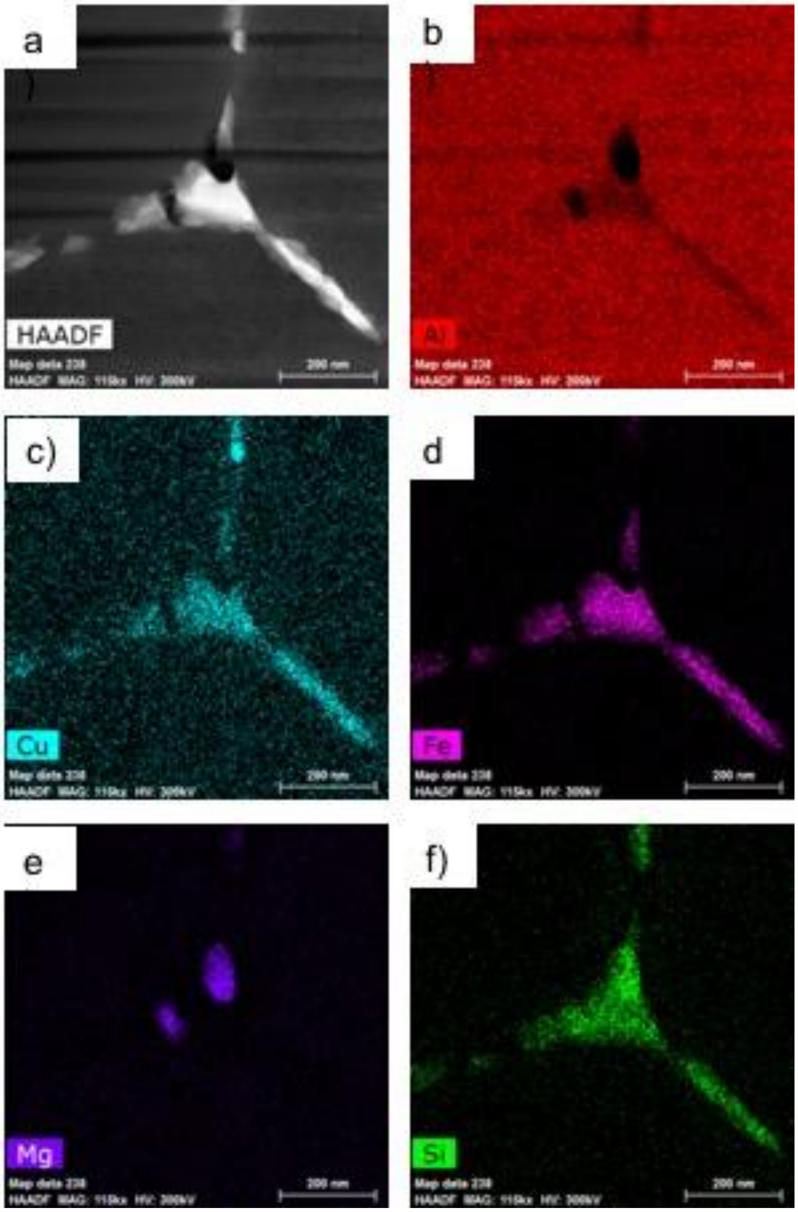

Figure 4: Higher magnification a) HAADF, and EDS maps of b) Al, c) Cu, d) Fe, e) Mg, and f) Si showing Mg_2Si and $AL_{13}Fe_4$ at a triple point in the as-atomized powder.

Table 2: Secondary phases, as predicted by Thermo-Calc.

Phase	**Possible Elements/More exact stoich.**
$Al_{13}Fe_4$	$(Al,Cu)_{0.63}(Zn,Fe,Mn)_{0.23}(Al,Si,Zn)_{0.14}$
Mg_2Si	Mg_2Si_1
Al_6Mn	$(Al,Zn,Cu)_6(Mn,Fe,Cu)_1$
$Al_9Fe_2Si_2$	$Al_{0.6}Fe_{0.15}Si_{0.1}(Al,Si)_{0.15}$
$Al_{45}V_7$	$Al_{45}Cr_7$
$Al_{15}Si_2M_4$	$Al_{16}(Si,Al)_2(Mn,Fe)_4Si_1$
Al_7Cu_2Fe	Al_7Cu_2Fe
$Al_{13}Cr_4Si_4$	$Al_{13}Cr_4Si_4$
Al_8Fe_2Si	$Al_{0.66}Fe_{0.19}Si_{0.05}(Al,Si)_{0.1}$
S-Phase	$(Al,Si)_2Cu_1Mg_1$
T-Phase	$Mg_{26}(Al,Mg)_6(Al,Mg,Cu,Zn)_{48}Al_1$

Image thresholding was used to quantify the amounts of these phases, and Figure 5 shows the results for both the SEM and TEM, represented as points and bars respectively. For the as-atomized condition quantified via SEM, it was determined that there was 0.27% (area) Mg_2Si and 5.16% (area) $Al_{13}Fe_4$, while via TEM it was determined that there was 0.4% (area) Mg_2Si and 2.5% (area) $Al_{13}Fe_4$. The area percentages measured for the Mg_2Si were consistent between the SEM and TEM quantifications. However, for the Fe-rich phase, $Al_{13}Fe_4$, the SEM measured twice as much as the TEM. This elevation is likely due to the larger interaction volume in the SEM, which makes phases under the surface fluoresce. Additionally, due to the small size of the TEM samples, it is expected that the quantifications may only be approximate, though the trends may still be significant.

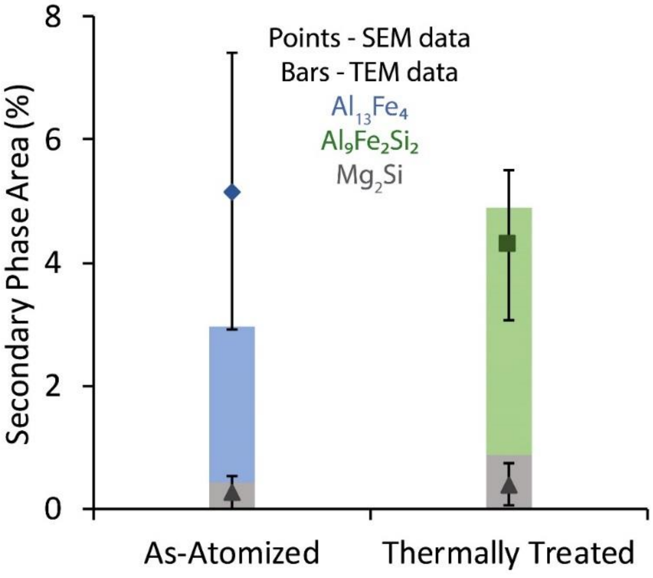

Figure 5: Secondary phase area percentages determined for the as-atomized and thermally treated conditions via both SEM (points) and TEM (bars).

Figure 6 shows a HAADF image and overview EDS maps of the powder microstructure in the thermally treated condition using TEM. Note the Fe-rich phases and Mg_2Si are no longer intertwined and that the Mg_2Si at the grain corners has substantially grown. Figure 7 and Figure 8 show high magnification HAADF and EDS maps of an Fe-rich phase. Note the incoherent boundaries, the accumulation of Cr at the outside of the phase, and the clusters of Mg on the boundary. Point EDS quantification of the Fe-rich phase reveals it to be $Al_9Fe_2Si_2$. What has been reported in literature, and what is predicted by thermodynamic and kinetic simulations (Thermo-Calc), indicate that $Al_9Fe_2Si_2$ has a more stoichiometric ratio of $Al_{0.6}Fe_{0.15}Si_{0.1}(Al,Si)_{0.15}$ (Table 2).

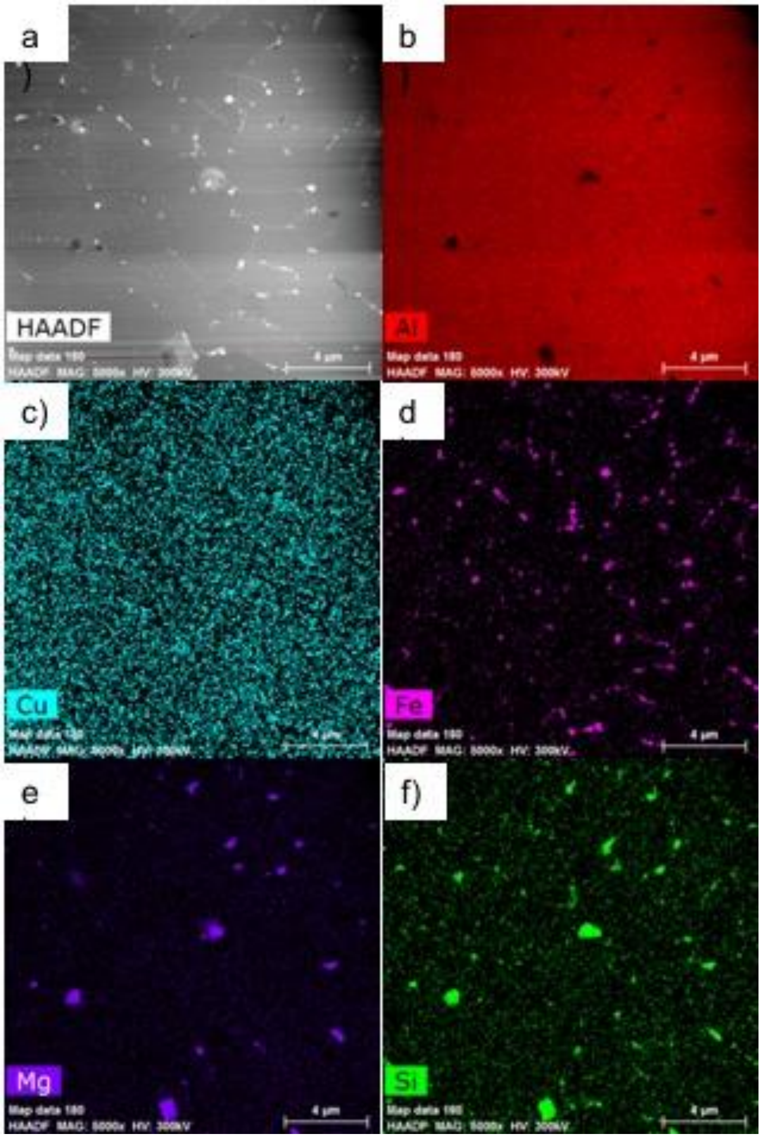

Figure 6: Overview images of the thermally treated powder: a) HAADF, and EDS maps of b) Al, c) Cr, d) Cu, e) Fe, f) Mn, g) Mg, and h) Si.

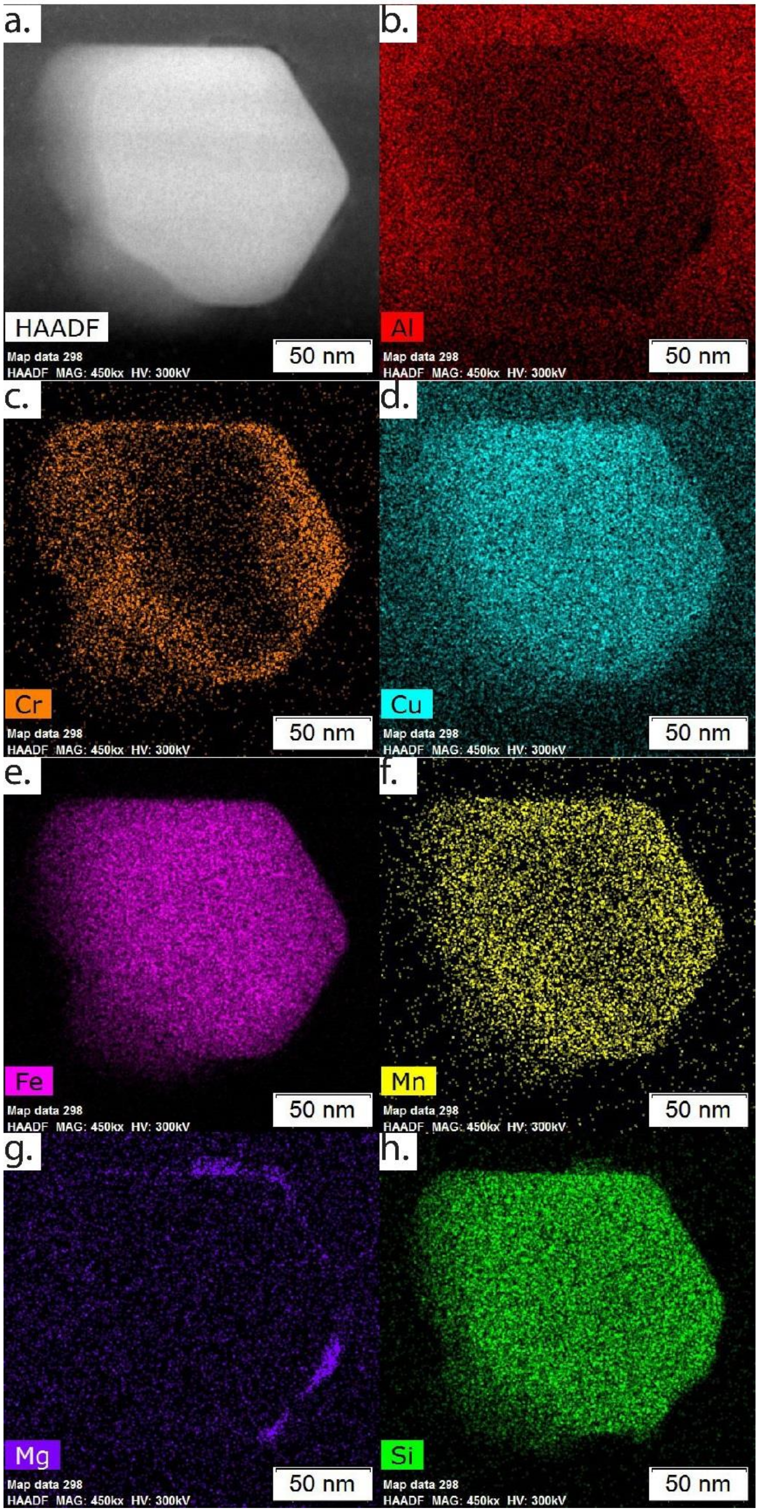

Figure 7: a) HAADF, and EDS maps b) Al, c) Cr, d) Cu, e) Fe, f) Mn, g) Mg, and h) Si showing Al9Fe2Si2 and residual Mg2Si in the thermally treated powder.

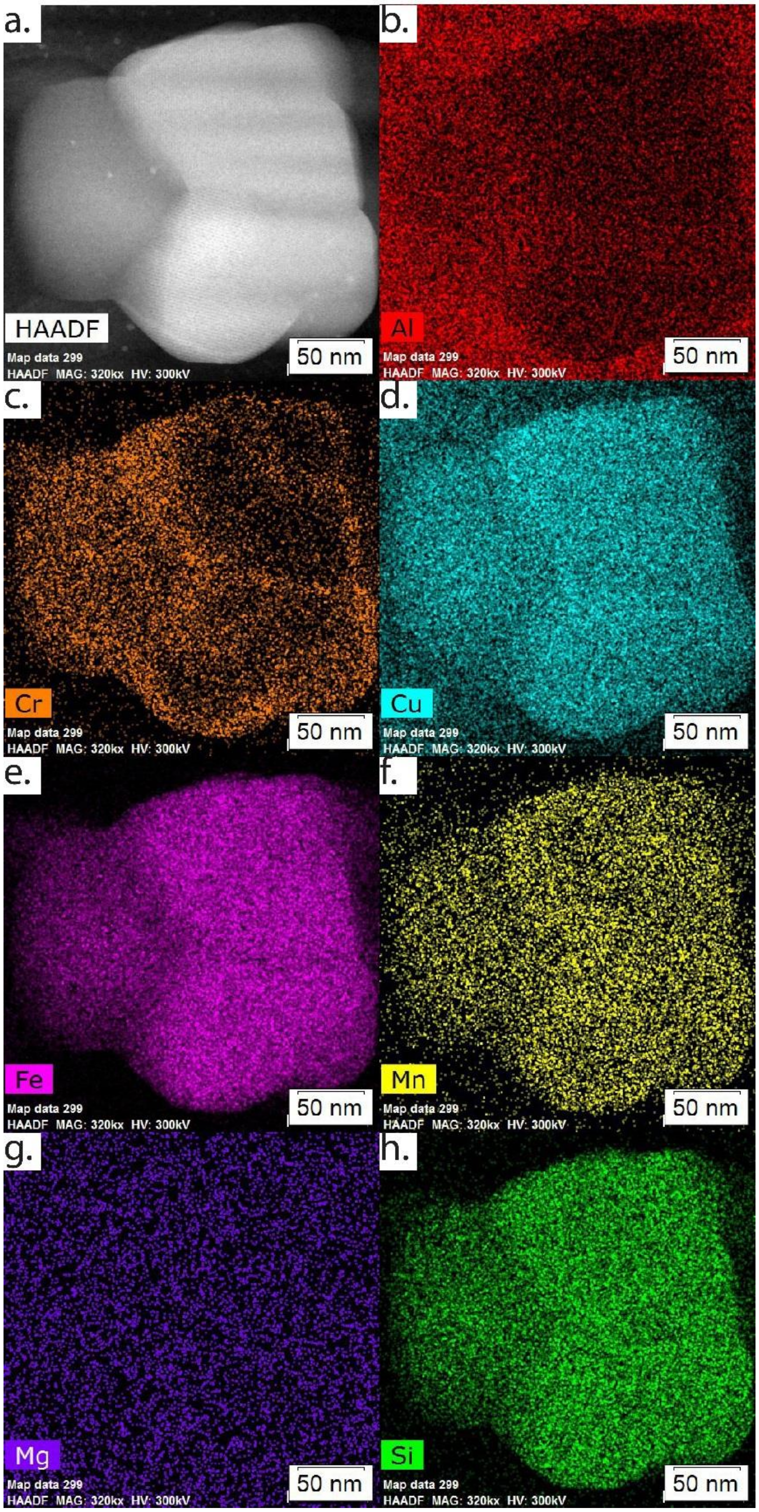

Figure 8: a) HAADF, and EDS maps of b) Al, c) Cr, d) Cu, e) Fe, f) Mn, g) Mg, and h) Si showing another morphology of Al9Fe2Si2 in the thermally treated powder.

Image thresholding was also used to quantify the amounts of these phases. Figure 5 shows the results determined via both the SEM and TEM. For the thermally treated condition as measured via SEM, it was determined that there was 0.4% (area) Mg_2Si and 4.29% (area) $Al_9Fe_2Si_2$, while via TEM it was determined that there was 0.9% (area) Mg_2Si and 4.0% (area) $Al_9Fe_2Si_2$. The areas measured for the Mg_2Si were consistent between the SEM and TEM quantifications. Unlike in the as-atomized condition, the amount of the Fe-rich phase, $Al_9Fe_2Si_2$, measured in the SEM was consistent with that measured in the TEM. Since the $Al_9Fe_2Si_2$ precipitates are larger and spherodized after thermal treatment than the $Al_{13}Fe_4$ precipitates were in the as-atomized condition, it is easier to isolate and reduce their fluorescence. Again, due to a small TEM sample size, it is expected that the quantifications may only be approximations for the actual amount of phases present.

Tsaknopoulos et al. performed work in a similar system, addressing the Mg_2Si evolution [14]. Fig. 2 in their work shows the thermodynamic stability of phases in this system, which is applicable to the work performed here. As indicated in their Fig. 2, $Al_{13}Fe_4$ is less stable than $Al_9Fe_2Si_2$ at 530 °C, the treatment temperature used here. Therefore, it is hypothesized that, upon heating, the $Al_{13}Fe_4$ dissolves, resulting in an area of matrix supersaturated in Fe, Si, and Cu. Upon prolonged exposure to elevated temperature, the Cu easily diffuses throughout the matrix. Since the $Al_{13}Fe_4$ was intertwined with the Mg_2Si, those regions with Fe and Si supersaturated in the matrix are still intertwined with the Mg_2Si. After the dissolution of the $Al_{13}Fe_4$, the $Al_9Fe_2Si_2$ readily forms, often nucleating on an undissolved Mg_2Si. It is not uncommon for there to be residual Mg_2Si after treatment at 530 °C [5,14].

When comparing the as-atomized to thermally treated conditions in Figure 5, it appears that the area fraction of Mg_2Si is constant, as determined via both SEM and TEM. This is inconsistent with what is expected, which is that the Mg_2Si should dissolve at the treatment temperature of 530 °C. When the micrographs are evaluated qualitatively, it can be seen that there are many small Mg_2Si precipitates in the as-atomized condition as opposed to the few, larger Mg_2Si precipitates in the thermally treated condition; this would lead the overall area fractions to be the same, but with different size distributions. This is consistent with other studies of gas-atomized Al 6061 powders [13-14].

Unlike the Mg_2Si, the area percentage of Fe-rich phases changes after thermal treatment. This is best understood when considering the identified phases; $Al_{13}Fe_4$ is 23.5% Fe while $Al_9Fe_2Si_2$ is 15.4% Fe. Assuming the Fe content remains constant throughout the treatment process and that all of the Fe present in the powder particle is in the Fe-rich phases, there is more Fe present in a given sized $Al_{13}Fe_4$ precipitate than in a same size $Al_9Fe_2Si_2$ precipitate. Given this, it is expected to see a smaller area percentage of $Al_{13}Fe_4$ than $Al_9Fe_2Si_2$; this is consistent with the trend seen in Figure 5.

Table 2 indicates that $Al_{13}Fe_4$ can contain Cu, Mn, Zn, and Si in addition to the Al and Fe; however, EDS maps indicate that Cu and Si are present but not Mn or Zn. It is important to consider the overall composition of the alloy (Table 1) and note that there is less than 0.05 wt% of both of these elements, making their presence difficult to detect unless highly concentrated.

Additionally, Table 2 indicates that $Al_9Fe_2Si_2$ should not contain Cu, Mn, or Cr, contrary to what is seen in the maps in Figure 7 and Figure 8. Given that the $Al_9Fe_2Si_2$ formed in a region formerly supersaturated with Cu, it is not unreasonable to assume that some excess Cu was remaining in that area during cooling after the heat treatment that was incorporated into the $Al_9Fe_2Si_2$. Prior to heating, the Cr and Mn were homogeneously supersaturated in the matrix. During heating, this likely remained. A major difference between the two conditions is the cooling rate; the as-atomized sample was rapidly solidified and experienced cooling rates on the order of 10^5-10^6 °C/min whereas the thermally treated sample was rapidly cooled and experienced cooling rates on the order of 10^2 °C/min. With the slower cooling rate, the matrix was likely unable to maintain the supersaturation with Cr and Mn, leading to the accumulation of those elements at the $Al_9Fe_2Si_2$ at the boundaries. Point EDS quantification of the $Al_9Fe_2Si_2$ revealed the exact composition to include 0.01 wt% Mn and 0.01 wt% Cr, which are considered trace amounts. To fully understand the transformations occurring in this system, hot stage TEM will be performed in future work.

Of the phases typically seen in bulk Al 6061 ($Al_{12}(FeMn)_3Si$, Al_8Fe_2Si, $Al_{12}Fe_3Si$, and $Al_{15}Fe_3Si_2$ [6-7]), none were identified in these gas-atomized powders. When Walde et al. [13] hypothesized that $Al_{45}Cr_7$, $Al_6(Fe,Mn)$, $Al_{13}Fe_4$, $Al_9Fe_2Si_2$, and Mg_2Si are present in the as-atomized condition with $Al_9Fe_2Si_2$ growing and the others all dissolving with thermal treatment, they were perhaps the most accurate. Two of their five predicted phases were seen in the as-atomized condition, and two of the five were seen in the thermally treated condition. Based on equilibrium conditions, $Al_9Fe_2Si_2$ would be present in abundance at room temperature. However, these powders were rapidly solidified, undergoing non-equilibrium conditions. Based on Scheil solidification (non-equilibrium conditions) predictions, as presented in Tsaknopoulos et al. [14] Fig. 2b, $Al_{13}Fe_4$ is the most abundant phase to form during solidification. As all of the Fe and some of the Si were used in the $Al_{13}Fe_4$, $Al_9Fe_2Si_2$ cannot form until the $Al_{13}Fe_4$ dissolves, as is seen after 60 minutes of thermal treatment at 530 °C.

It is important to remember that the type of sample considered here is rapidly solidified powders. Given the finer microstructural features in powders, as compared to their wrought counterparts, the shorter diffusion distances and metastable conditions have a great effect on the phase type, morphology, and chemistry seen in the powders. In general, both the $Al_{13}Fe_4$ and $Al_9Fe_2Si_2$ have morphologies different than their wrought counterparts. This is consistent with other microstructural evaluations of rapidly solidified powders [13-14].

7.5 Conclusion

By employing extensive TEM and EDS analysis, this work analyzes the effect of thermal treatment on the AlFeSi intermetallics present in gas-atomized 6061 powders. It was shown that $Al_{13}Fe_4$ was present in the as-atomized condition and transforms to $Al_9Fe_2Si_2$ after a treatment of 1 hour at 530 °C. Since parts made via MAM techniques can retain microstructural features of the feedstock powder in the consolidated part, it is beneficial to understand the microstructure of the feedstock powder prior to consolidation.

7.6 Acknowledgements

This work was funded by the United States Army Research Laboratory, grant #W911NF-15-2-0024.

This work was performed in part at the *Kostas Advanced Nano-Characterization Facility in Kostas Research Institute at Northeastern University* and at the *Center for Nanoscale Systems (CNS)*, a member of the National Nanotechnology Coordinated Infrastructure Network (NNCI), which is supported by the National Science Foundation under NSF award no. 1541959.

7.7 References

1. E.O. Olakanmi, R.F. Cochrane, and K.W. Dalgarno, A review on selective laser sintering/melting (SLS/SLM) of aluminium alloy powders: Processing, microstructure, and properties. *Prog. Mater. Sci.*, 2015; **74**, p 401-477.
2. M. Tang, and P.C. Pistorius, Oxides, Porosity and fatigue performance of AlSi10Mg parts produced by selective laser melting. *Int. J. Fatigue*., 2017, **94**, p 192-201.
3. RW Smith, and R Knight, Thermal spraying I: Powder consolidation-From coating to forming. *JOM*, 1995, **47**(8), p 32-39.
4. WE Quist, and RE Lewis, The need for rapidly solidified powder metallurgy aluminum alloys for aerospace applications, *Rapidly Solidified Powder Aluminum Alloys*, Fine ME, Starke EA, Ed., Philadelphia (PA), ASTM International, 1986, p 22.
5. L Katgerman, and D Eskin, Hardening, Annealing, and Aging. *Handbook of Aluminum: Vol. 1: Physical Metallurgy and Processes,* G.E. Totten, Ed., Boca Raton (FL), CRC Press, 2003, p. 259-304
6. SG Shabestari, The effect of iron and manganese on the formation of intermetallic compounds in aluminium-silicon alloys, *J. Mater. Sci. Eng. A*., 2004, **383**(2), p 289-298.
7. M Lech-Grega, and S Boczkal, Iron Phases in Model Al-Mg-Si-Cu Alloys, *Mater. Sci. Forum*., 2011, **674**, p 135-140.
8. M Rokni, C Widener, and V Champagne, Microstructural evolution of 6061 aluminum gas-atomized powder and high-pressure cold-sprayed deposition, *J. Therm. Spray Technol.,* 2014, **23**(3), p 514-524.
9. M. Rokni, C. Widener, V. Champagne, G. Crawford, and S. Nutt, The effects of heat treatment on 7075 Al cold spray deposits, *Surf. Coatings Technol.,* 2017, **310,** p 278-285.
10. M Rokni, C Widener, O Ozdemir, and G Crawford. Microstructure and mechanical properties of cold sprayed 6061 Al in As-sprayed and heat treated condition. *Surf. Coatings Technol.*, 2017, **309**, p 641-650.

11. M Rokni, C Widener, G Crawford, and M West, An investigation into microstructure and mechanical properties of cold sprayed 7075 Al deposition, *Mater. Sci. Eng. A*., 2015, **625**, p 19-27.

12. A Sabard, H de Villiers Lovelock, and T Hussain, Microstructural Evolution in Solution Heat Treatment of Gas-Atomized Al Alloy (7075) Powder for Cold Spray, *J. Therm. Spray Technol*., 2018, **27**(1-2), p 145-158.

13. C Walde, D Cote, V Champagne, and R Sisson, Characterizing the Effect of Thermal Processing on Feedstock Al Alloy Powder for Additive Manufacturing Applications, *J. Mater. Eng. Perform.,* 2018, DOI: 10.1007/s11665-018-3550-0

14. K Tsaknopoulos, C Walde, V Champagne, and D Cote, Gas-Atomized Al 6061 Powder: Phase Identification and Evolution During Thermal Treatment, *JOM*, 2018, DOI: 10.1007/s11837-018-3175-7

15. "Standard Specification for Woven Wire Test Sieve Cloth and Test Sieves," E11-17, American Society for Testing and Materials (ASTM International). USA: ASTM; 2017.

16. "Standard Guide for Determination of Various Elements by Direct Current Plasma Atomic Emission Spectroscopy," E1097-17, American Society for Testing and Materials (ASTM International). USA: ASTM; 2017.

17. "Standard Specification for Aluminum and Aluminum-Alloy Sheet and Plate," EB209-14, American Society for Testing and Materials (ASTM International). USA: ASTM; 2014.

18. B Bedard, T Flanagan, A Ernst, A Nardi, A Dongare, H Brody, V Champagne, S Lee, and M Aindow, Microstructural and Micromechanical Response in Gas-Atomized Al 6061 Alloy Powder and Cold-Sprayed Splats, *J. Therm. Spray Tech.,* 2018 , DOI: 10.1007/s11666-018-0785-0.

8 Phase Transformations in Al 7075 Powder

Phase Transformations in Thermally Treated Gas-Atomized Al 7075 Powder

Caitlin Walde [1], Kyle Tsaknopoulos [1], Victor Champagne[2], Danielle Cote[1]*

[1]Worcester Polytechnic Institute, Worcester, MA
[2]US Army Research Laboratory, Aberdeen Proving Grounds, MD
*Corresponding author; dlcote2@wpi.edu

Under Review

8.1 Abstract

Al 7075 is a heat treatable Al-Mg-Zn alloy widely used in the aerospace industry. Recently, it has found application as feedstock for metal additive manufacturing (MAM) techniques. It has been shown that wrought alloy compositions in powder form differ greatly in microstructure and properties from their conventional form. Given this, it is important to understand the internal microstructure of the powders prior to use in MAM processes.

This work studies the as-atomized condition of gas-atomized Al 7075 powders, as well as the effect of thermal treatments on the microstructure and secondary phases. Extensive electron microscopy revealed the presence of T-Phase, Al_7Cu_2Fe, and Mg_2Si in the as-atomized condition of this gas-atomized Al 7075 powder. Thermal treatments were performed at 465 °C and 480 °C with the goal of homogenizing the microstructure – dissolving T-phase while avoiding S-phase growth, avoiding Al_7Cu_2Fe coarsening, and avoiding melting. In the samples treated at 465 °C, S-phase was unexpectedly present. In both 465 °C and 480 °C treatments, the T-phase was not fully dissolved after the 60 minute treatment. Guided by the thermodynamic modeling, these results indicate a shift in local equilibria in these powders.

8.2 Introduction

Al 7075 is a heat treatable Al-Mg-Zn alloy that is widely used in the aerospace industry in compressively loaded parts for its combination of high specific strength and resistance to stress corrosion cracking [1]. Al 7075 is available in multiple forms; it is typically cast then worked to a wrought condition, though it is also available in wires and powders. The latter forms are used mainly as feedstock in metal additive manufacturing (MAM) processes. Powder-fed processes are more common, with selective laser melting (SLM), powder bed fusion (PBF), and selective laser sintering (SLS) having perhaps the most wide-spread use [2]. In liquid-state processes, where the powder is melted during consolidation, features present in the feedstock powder – such as surface oxides and internal porosity – can be retained during consolidation. In solid state processes, where the powder is not melted during consolidation, this effect is more significant, with features such as secondary phases, in addition to surface oxides and internal porosity, being retained during consolidation. With this in mind, it is important to understand the microstructure of the powders prior to consolidation [3-4].

The feedstock powders are often gas-atomized, experiencing cooling rates on the order of 10^6 °C/s during solidification [5]. This categorizes the powders as rapidly solidified, which results in microstructures very different than conventional castings, where the cooling rate is on the order of less than 10^2 °C/s [5]. Minimal segregation, non-equilibrium phases, and microstructure homogeneity are characteristics of rapidly solidified structures [5-7].

The three primary steps in a heat treatment are solutionization, quenching, and aging [8]. The purpose of the solutionizing step is to dissolve secondary phases and achieve a homogenous microstructure; this is typically performed at elevated temperatures in the 450-550 °C range, depending on the alloy. This step is followed by a rapid quench, to maintain the supersaturated metastable microstructure at room temperature. The aging step is designed to homogenously nucleate and grow the primary strengthening phase in the alloy; this is usually performed at lower temperatures in the 150-250 °C range, depending on the alloy. For Al 7075, the strengthening sequence is GP zones (MgZn) $\rightarrow$ η' $\rightarrow$ η ($MgZn_2$) $\rightarrow$ T' $\rightarrow$ T $\rightarrow$ ($Al_2Mg_3Zn_3$) [8]. Whether the sequence finishes at η or at T phase depends on the Mg:Zn ratio. Natural aging typically continues for years, so artificial aging steps are important to achieve stable precipitates. Additionally, as Fe and Si are impurities in Al, Al_7Cu_2Fe, $Al_{12}(Fe,Mn)_3Si$, $Al_6(Fe,Mn)$, Mg_2Si, SiO_2, and $Al_{23}CuFe_4$ are also common phases in Al 7075, in addition to the η and T strengthening phases. Depending on the exact alloy compositions, some of these phases may be insoluble. Of note is that Mg_2Si is virtually insoluble in Al 7075 [1].

Because features in the powder are retained during consolidation, the as-atomized microstructure can be controlled using thermal treatments. Recent research has shown the retention of feedstock powder microstructure during consolidation for other alloys, though that research included a limited analysis of the internal microstructure of the powders, not fully investigating the effect of the thermal treatments on the powders [9-14]. These researchers assumed the network of solute elements at the boundaries in the as-atomized structure, as seen in scanning electron microscopy (SEM) and energy dispersive x-ray spectroscopy (EDS), was segregation. While the presence of secondary phases was noted in the thermally treated powders, no further in-depth analysis was performed to identify the phases. However, in-depth analysis here indicates the as-atomized microstructure of the powders is actually distinct phases, as revealed using transmission electron microscopy (TEM), consistent with what is expected in rapid solidification [3,15]. Additionally, it was recently noted that these gas-atomized powders have both a granular and sub-granular structure. The secondary phases exist at all boundaries, with groups of sub-grains having the same orientation, comprising larger grains [3-4,15]. The size of the sub-grains is typically what is reported; when etched it is impossible to distinguish between the high-angle and low-angle boundaries that differentiate the grains and sub-grains.

Solutionization times for Al 7075 are typically on the order of 4-16 hours for wrought components, depending on part size [8]. Given this time scale, other researchers chose to use long heat treatment times for their powders, however, other research performed on Al 6061 indicated faster diffusion times in powders, resulting in the need for shorter thermal treatments [4,9].

This research investigates the effect of thermal treatment on the transformations of the secondary phases present in gas-atomized Al 7075 powders through the use of TEM and EDS.

8.3 Method

The studied powder was gas-atomized Al 7075 (Valimet, Inc., Stockton, CA) with a d_{10} of 26.1 µm, d_{50} of 37.1 µm, and d_{90} of 52.5 µm. The composition of the powders, as determined by direct current plasma emission spectroscopy and shown in Table 1, is within the acceptable ranges for Al 7075 [16-17].

Table 1: Powder composition compared to ASTM standard.

Element	**Wt %**	**ASTM B209**
Cr	0.210	0.18-0.28
Cu	1.700	1.2-2.0
Fe	0.180	0.50
Mg	2.300	2.1-2.9
Mn	0.031	0.30
Si	0.110	0.40
Ti	0.031	0.20
Zn	5.600	5.1-6.1
Other		0.15
Al	89.8	remainder

Thermal treatment parameters were determined with the assistance of computational thermodynamic and kinetic software (Thermo-Calc, Stockholm, Sweden), shown in Figure 1. Thermal treatments were performed with the goal of homogenizing the microstructure – dissolving T-phase while avoiding S-phase growth, avoiding Al_7Cu_2Fe coarsening, and avoiding melting. 465 °C was selected to reduce the coarsening effect of Al_7Cu_2Fe by maintaining a lower temperature to slow diffusion while still avoiding the formation of S-phase, which is present below 450 °C. 480 °C was chosen because it is the conventional solutionization temperature used for Al 7075. Treatment times ranged from 0-4 hours. The “as-atomized” indicates an untreated condition, while the thermally treated conditions are noted by the time at treatment temperature; the thermally treated samples all experienced the ramp to elevated temperature. Samples were treated in a nitrogen environment in a differential scanning calorimeter (DSC) because of its high thermal accuracy. One sample was left untreated, in the as-atomized condition.

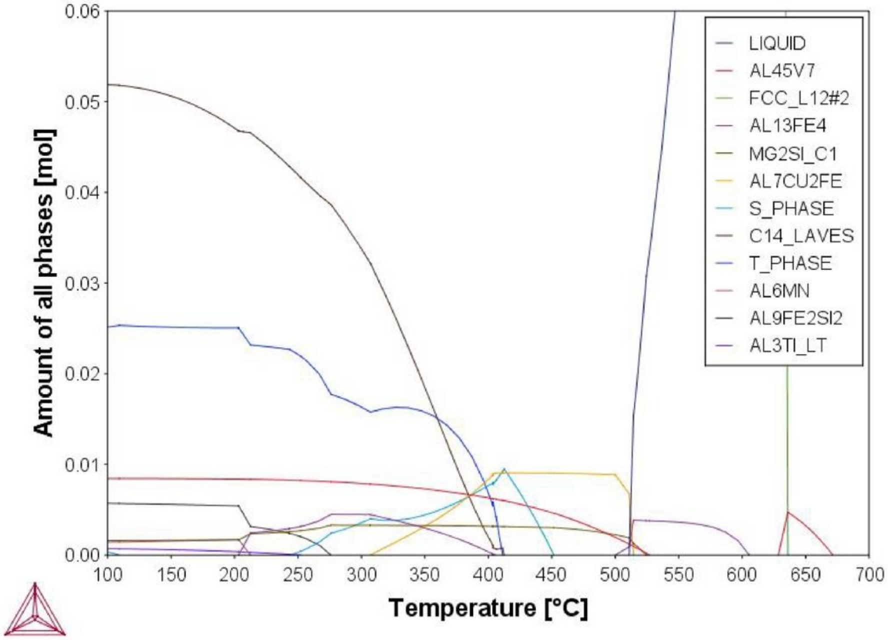

Figure 1: Equilibrium diagram, as predicted by Thermo-Calc simulations. Amount of phases present as a function of temperature for the specific composition of the alloy investigated given in Table 1.

Samples were prepared for scanning electron microscopy (SEM) and energy dispersive x-ray spectroscopy (EDS) analyses by mounting the powders in a hot-cure epoxy and grinding and polishing incrementally with a final 0.25 µm colloidal silica suspension.

SEM and EDS analyses were performed on all samples using a tungsten-filament SEM at 10-15 kV. Powders in both the as-atomized and thermally treated conditions of 465 °C for 60 minutes and 480 °C for 60 minutes were prepared for transmission electron microscopy (TEM) analysis using focused ion beam (FIB) milling (Scios DualBeam and Helios 660 Nanolab, ThermoFisher Scientific, Waltham, MA) [15,19]. Lamellae were polished with a final beam current of 0.1 nA and had a final thickness of less than 200 nm. TEM analysis was performed using a probe-corrected TEM (Titan Themis with ChemiSTEM, ThermoFisher Scientific, Waltham, MA) and energy dispersive X-Ray spectroscopy (EDS) (Super-X, ThermoFisher Scientific, Waltham, MA) at an accelerating voltage of 300 kV. The amounts of secondary phases present in the conditions were quantified using image contrast thresholding. All EDS maps are in wt%.

Additionally, the as-atomized condition was evaluated using electron backscatter diffraction (EBSD). FIB was used to prepare powder particles for EBSD analysis, and an accelerating voltage of 20 kV with a step size of 0.3 µm was used for analysis.

8.4 Results and Discussion

Figure 2 displays an overview SEM micrograph and EBSD micrograph of the as-atomized condition. The continuous network structure present at both the grain and sub-grain boundaries in the as-atomized is consistent with what is seen in other gas-atomized powders [15]. Note the large grains in Figure 2b that have smaller regions with slight misorientation (<15°) within them, which corresponds to the sub-grain boundaries.

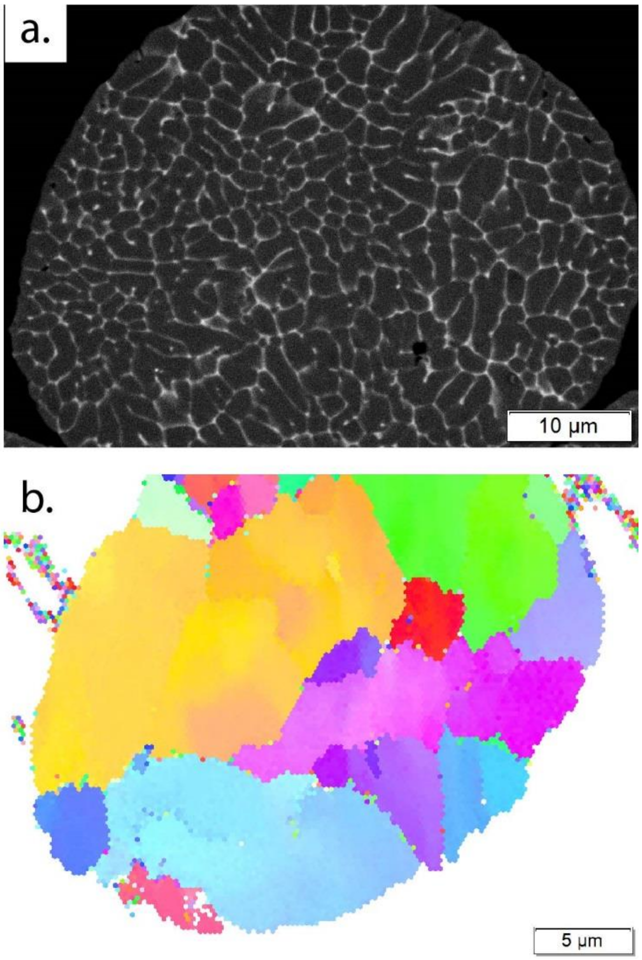

Figure 2: Overview SEM micrograph and EBSD micrograph of the as-atomized condition.

Figure 3 shows overview SEM micrographs of the thermally treated conditions. As seen in Figure 3a and Figure 3b, the network structure present in the as-atomized condition begins to dissolve simply by bringing the powder up to an elevated temperature. With increased treatment times, note the presence of both larger phases and smaller phases in two different regions; the large phases are present at the high-angle grain boundaries, such as seen in Figure 2b, while the smaller phases are present at the low-angle sub-grain boundaries.

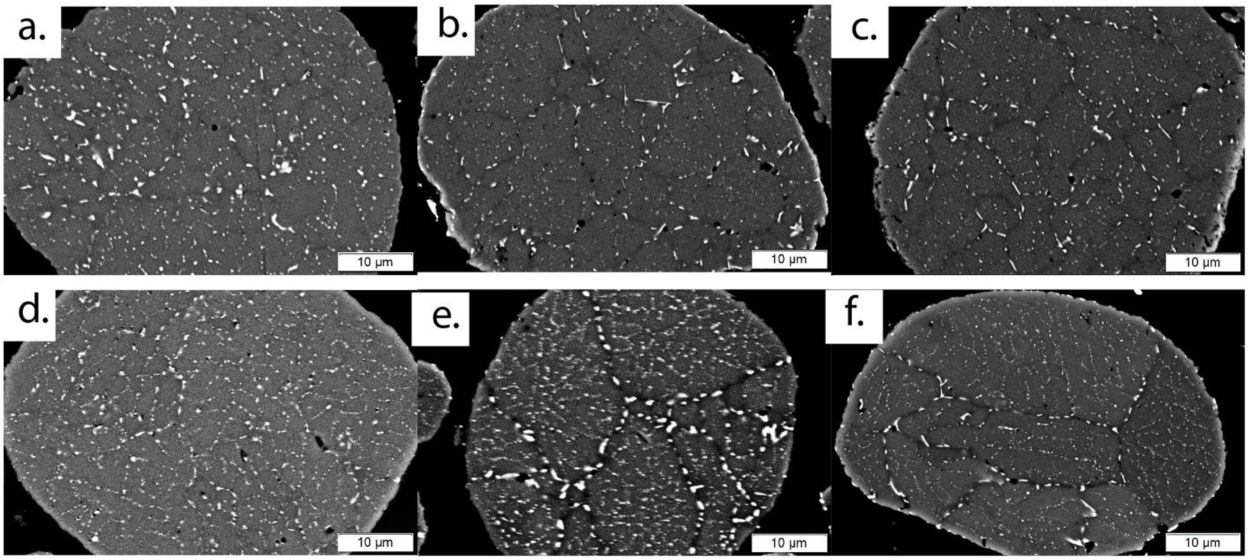

Figure 3: Overview SEM micrographs of the thermally treated conditions; a) 465 °C for 0min, b) 465 °C for 60min, c) 465 °C for 120min, d) 480 °C for 0min, e) 480 °C for 60min, f) 480 °C for 120min.

Figure 4 shows the area percent of secondary phases present as a function of treatment time for both treatment temperatures.

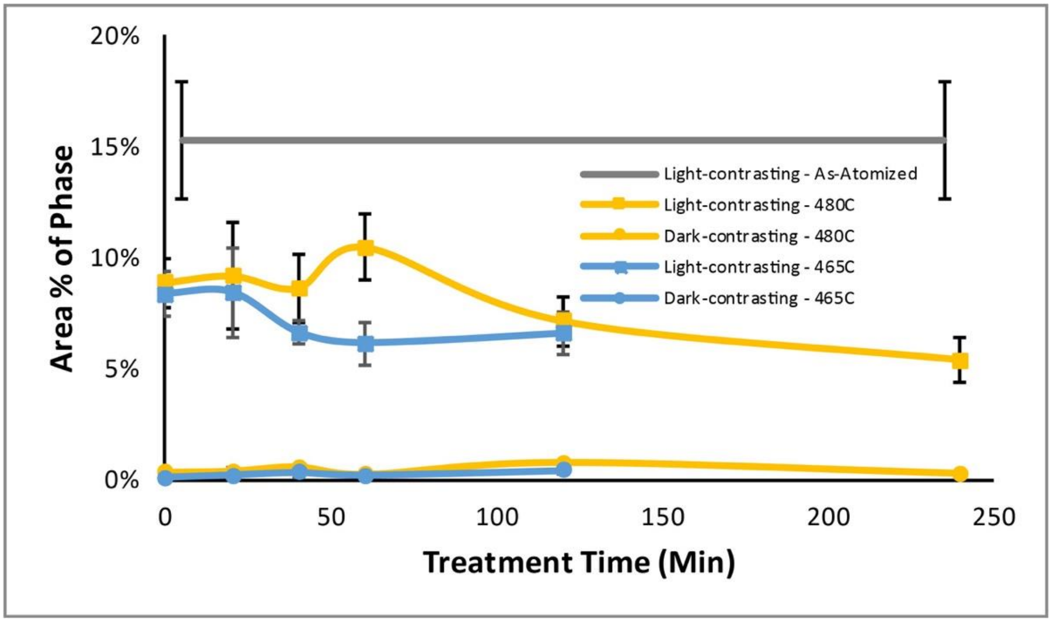

Figure 4: Area percent of secondary phases present as a function of treatment time for both treatment temperatures.

In the treatment performed at 465 °C, there is an initial drop in secondary phase amount after the sample reaches the set temperature, consistent with Figure 3. Then, there is a slight decrease in amount of light-contrasting secondary phases after 20 minutes of treatment, stabilizing after 60 minutes of treatment. The dark-contrasting phases, while not detected in the as-atomized condition, is stable in very low amounts across all treatment temperatures.

In the treatment performed at 480 °C, there is an initial drop in secondary phases after increasing the sample to the set temperature, consistent with Figure 3d, after which there is a slight increase in the light-contrasting phases until 60 minutes of treatment. After 60 minutes, the light-contrasting phases decrease. The dark-contrasting phase, while not detected in the as-atomized condition, is stable across all treatment temperatures.

When comparing the two treatment temperatures, it is of note that the dark-contrasting phase area percent is the same, whereas the light-contrasting phase trends vary. There is a similar reduction in the light-contrasting phase in both treatments when at the set temperature. However, after approximately 20 minutes of treatment, the trends diverge; at 480 °C, the light-contrasting phase increases while at 465 °C the light-contrasting phase decreases. After approximately 120 minutes of treatment, the trends converge again, appearing to reach an equilibrium.

Due to the large interaction volume in the SEM, EDS was not successful in further differentiating the light- and dark-contrasting phases into the constituents predicted in Thermo-Calc. Hence, EDS was performed in a TEM.

Figure 5 shows overview TEM micrographs of the as-atomized and thermally treated conditions for 60 minutes at each temperature. Figure 5a shows a similar structure as seen in the SEM in Figure 2a; on the other hand, Figure 5b and Figure 5c provide much more detail than their SEM counterparts in Figure 3. Figures 6-8 show higher magnification TEM micrographs and corresponding EDS maps to give further insight into the specific constituents present in each condition.

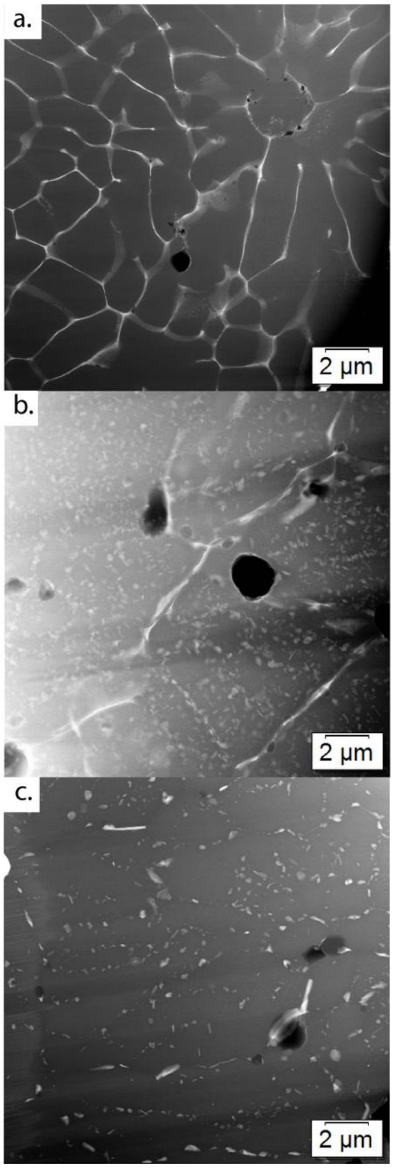

Figure 5: Overview TEM micrographs of a) the as-atomized condition, b) 60min at 465 °C and c) 60min at 480 °C.

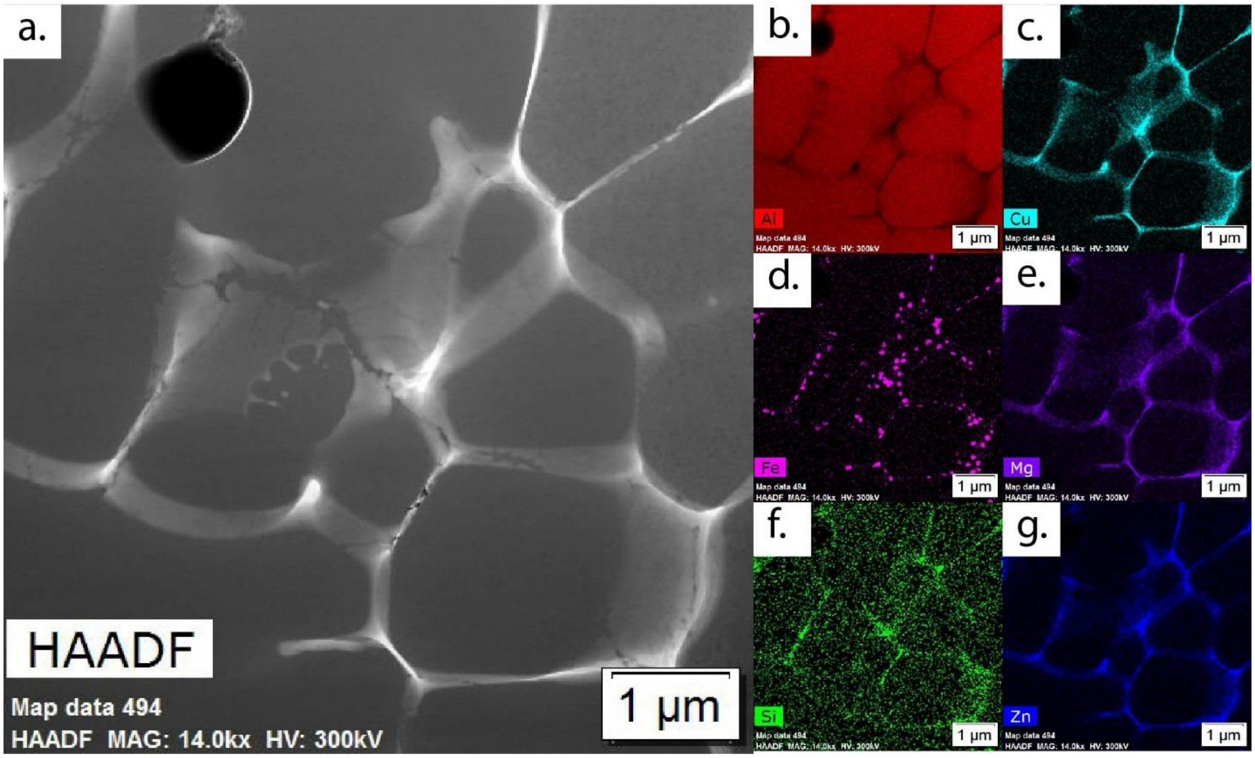

Figure 6: TEM micrograph and EDS maps for the as-atomized condition; a) HAADF, b) Al, c) Cu, d) Fe, e) Mg, f) Si, and g) Zn.

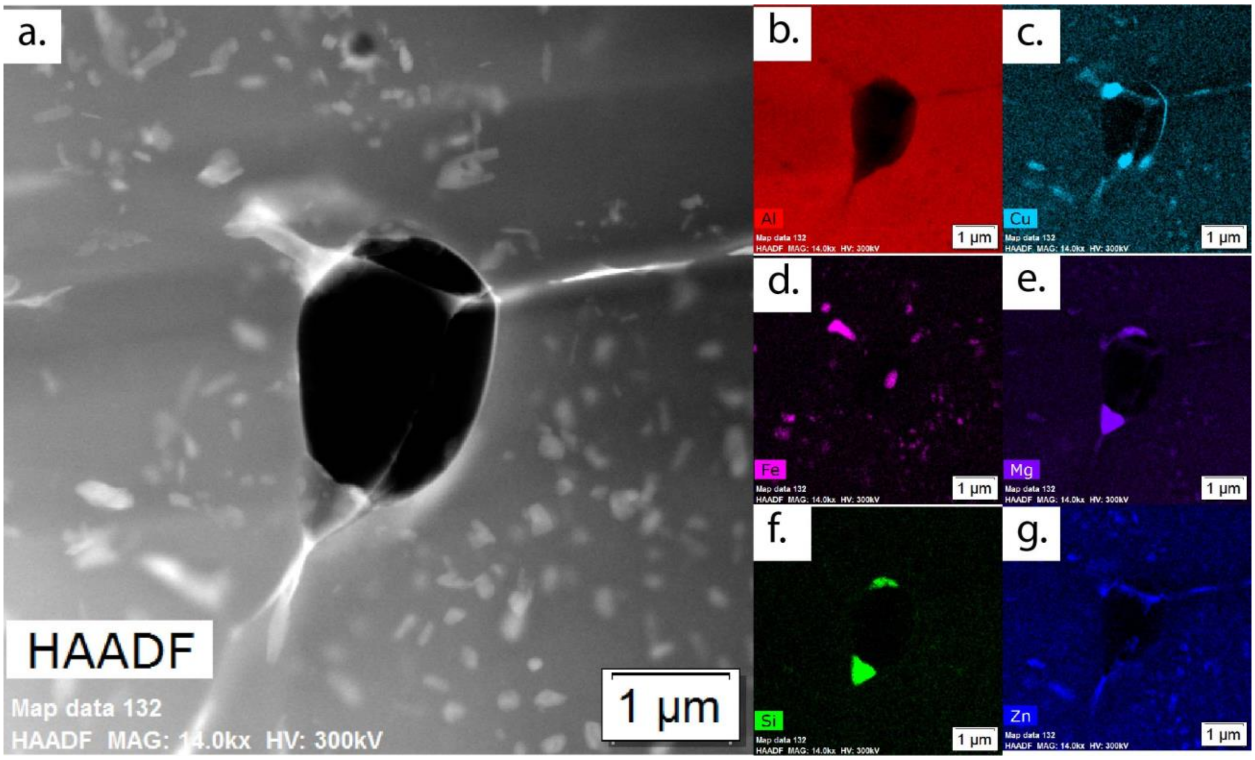

Figure 7: TEM micrograph and EDS maps for the 60min at 465 °C condition; a) HAADF, b) Al, c) Cu, d) Fe, e) Mg, f) Si, and g) Zn.

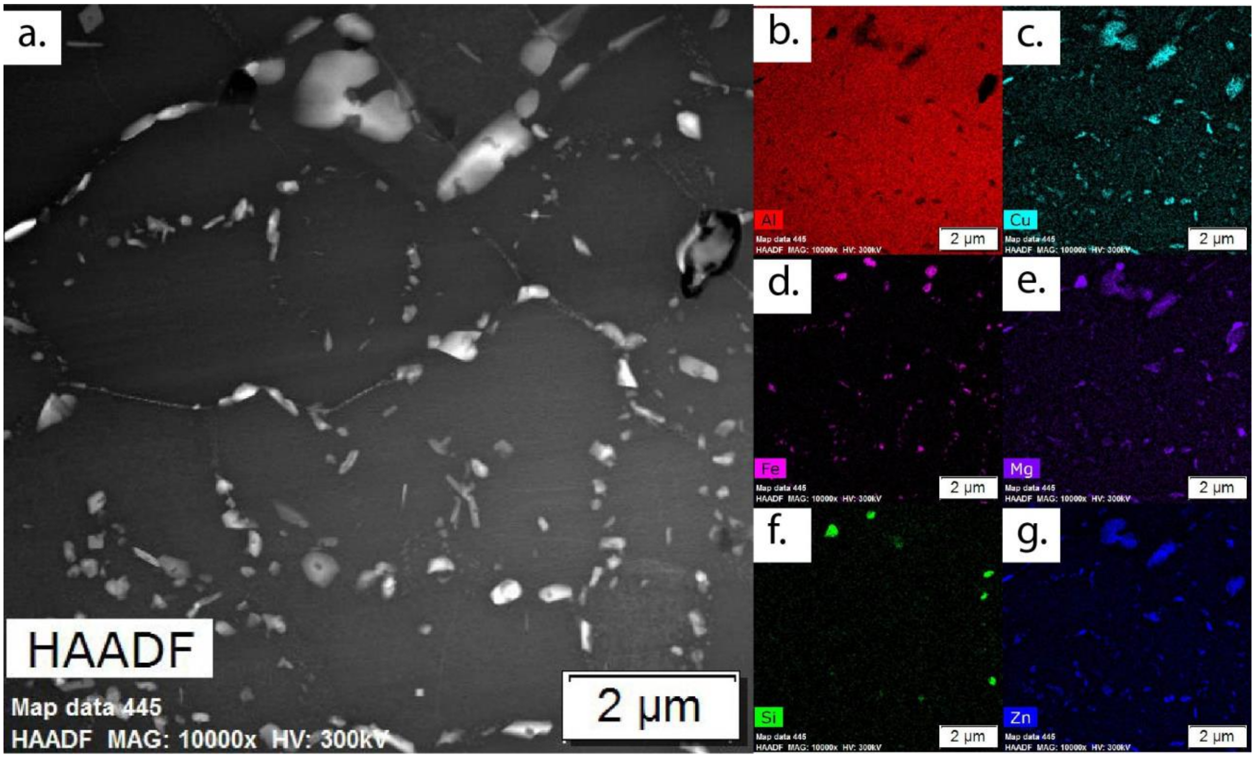

Figure 8: TEM micrograph and EDS maps for the 60min at 480 °C condition; a) HAADF, b) Al, c) Cu, d) Fe, e) Mg, f) Si, and g) Zn.

Figure 6 shows TEM micrograph and EDS maps for the as-atomized condition. Note the presence of two phases – an Al-Cu-Mg-Zn network phase and discrete Fe-rich phases. EDS point quantification revealed the Al-Cu-Mg-Zn network to be T-phase and the discrete Fe-rich phases to be Al_7Cu_2Fe, which is consistent with what is seen in literature [1]. Additionally, the dark-contrasting phase seen in the thermally treated SEM micrographs (Figure 3 and Figure 4) is also found in the as-atomized structure using TEM, and has been identified as Mg_2Si.

Figure 7 shows TEM micrograph and EDS maps for the sample thermally treated at 465 °C for 60 minutes. Note the presence of four phases – an Al-Cu-Mg-Zn phase, an Al-Cu-Mg phase, an Fe-rich phase, and a Si-rich phase. EDS point quantifications revealed the Al-Cu-Mg-Zn phase to be residual T-phase that had not fully dissolved, the Al-Cu-Mg phase to be S-phase, the Fe-rich phase to be the Al_7Cu_2Fe, and the Si-rich phase to be Mg_2Si. Based on the equilibrium diagram in Figure 1, S-phase is not expected to be present at this temperature; this indicates a difference in the local equilibrium for the powder in comparison to the global powder composition as measured by direct current plasma emission spectroscopy.

Figure 8 shows TEM micrograph and EDS maps for the sample thermally treated at 480 °C for 60 minutes. Note the presence of three phases – an Al-Cu-Mg-Zn phase, an Fe-rich phase, and a Si-rich phase. EDS point quantifications revealed the Al-Cu-Mg-Zn phase to be residual T-phase that had not fully dissolved, the Fe-rich phase to be the Al_7Cu_2Fe, and the Si-rich phase to be Mg_2Si. Note the lack of the S-phase that was present in the 465 °C thermally treated condition.

An unexpected similarity between the treatment temperatures is the presence of T-phase seen in Figure 7 and Figure 8. The equilibrium predictions indicate that T-phase should not be present at either temperature; this indicates that 60 minutes of treatment at either temperature is not sufficient time to dissolve the T-phase. As Scheil simulations predict T-phase to be the most abundant phase, it is expected that it may take additional time to dissolve. Unfortunately, it is not possible to distinguish between the T-phase and Al_7Cu_2Fe in the SEM (Figure 3), so further TEM work would be needed to determine if 120 minutes or 240 minutes of treatment is sufficient to fully dissolve T-phase.

Additionally, large and small phases can be seen in both the SEM and TEM micrographs; they have been identified as both T-phase and Al_7Cu_2Fe, with sizes corresponding to different boundary types. The high-angle boundaries have more open space, hence the phases can be larger there, whereas the phases at the low-angle boundaries have less open space for growth.

Of significant note is the difference in precipitate locations between the 465 °C and 480 °C treatment temperatures; the 465 °C treatment has precipitates both at the boundaries and in the bulk of the grains, whereas the 480 °C only has precipitates at the boundaries. Because the grains are so small in these gas-atomized powders and there is such a small diffusion distance to the grain boundaries from the center of the grains, the driving force for precipitation on the boundaries is easily achievable, thus precipitation will occur first and most frequently on the grain boundaries. However, it is possible for the boundaries to become saturated. This is the case in the 465 °C treatment. The boundaries are saturated with T-phase and Al_7Cu_2Fe so the S-phase can only precipitate in the bulk matrix. This can be seen in both the SEM and TEM micrographs.

Given the increase in understanding of the phases present in each condition from study in TEM, it is beneficial to revisit Figure 4 to further understand the trends found in the SEM analysis. Recall the increasing trend in the light-contrasting phases in the 480 °C treatments at 60 minutes; in TEM, two different light-contrasting phases were identified at the boundaries: Al_7Cu_2Fe and T-phase. As previously stated, the T-phase is in the process of dissolving, so this increase is likely due to the coarsening of the Al_7Cu_2Fe at a faster rate than the T-phase dissolution. It is expected that after 120 minutes of treatment, the T-phase would be fully dissolved and the Al_7Cu_2Fe reached a stable size and fraction, reflected in the plateau in Figure 4. In comparison, at 60 minutes of treatment at 465 °C, there is a decreasing trend in the light-contrasting phases in the SEM. This trend is surprising because based on the TEM results, there are three different light-contrasting phases present – Al_7Cu_2Fe and T-phase at the boundaries and S-phase in the bulk of the grains. Because S-phase is forming, Al_7Cu_2Fe cannot coarsen. In SEM, S-phase was not detected in the bulk, but this is likely due to the limiting resolution of the SEM; this causes the area fraction to appear lower than expected based on TEM results. With this in mind, it is important to understand the limitations of individual characterization techniques and utilize multiple techniques.

8.5 Conclusions

Extensive electron microscopy revealed the presence of T-Phase, Al_7Cu_2Fe, and Mg_2Si in the as-atomized condition of this gas-atomized Al 7075 powder. Thermal treatments were performed with the goal of homogenizing the microstructure – dissolving T-phase while avoiding S-phase growth, avoiding Al_7Cu_2Fe coarsening, and avoiding melting. 465 °C was chosen because the Al_7Cu_2Fe should coarsen slower at a lower temperature, and this is as low as possible without containing S-phase. 480 °C was chosen because it is the conventional solutionization temperature used for Al 7075. In the samples treated at 465 °C, S-phase was present, indicating a shift in local equilibrium of the powders as compared to the global composition of the powder batch. In both treatments, 60 minutes was insufficient to fully dissolve the T-phase. Due to the large interaction volume of the SEM as compared to the size of the precipitates present in these powders, it is not possible to accurately differentiate these phases in the SEM; additional TEM would be necessary to evaluate the time required to fully dissolve the T-phase.

It is important to understand the benefits, as well as the limitations, of different microscopy techniques and utilize multiple for different purposes. The SEM is useful for high-throughput measurements and total secondary phase area quantification. However, its lower resolution does not allow for tracking individual secondary phases. The TEM is useful for its high-resolution, allowing for identification of individual phases. However, the time required for sample preparation limits its feasibility for high-throughput evaluations. Leveraging the strengths of each technique, and coupling both of these microscopy techniques with modeling, allows for enhanced understanding of the microstructural evolution with decreased time spent on data collection.

8.6 Acknowledgements

This work was funded by the United States Army Research Laboratory, grant #W911NF-15-2-0024.
This work was performed in part at the *Kostas Advanced Nano-Characterization Facility in Kostas Research Institute at Northeastern University* and at the *Center for Nanoscale Systems (CNS)*, a member of the National Nanotechnology Coordinated Infrastructure Network (NNCI), which is supported by the National Science Foundation under NSF award no. 1541959.

8.7 References

1. G.E. Totten and D.S. MacKenzie: *Handbook of Aluminum: Vol. 1: Physical Metallurgy and Processes*, CRC Press, Boca Raton, FL, 2003, pp. 81-210.
2. William E. Frazier: *JMEP,* 2014, ser. 6, vol. 23, pp. 1917-1928.
3. K. Tsaknopoulos, C. Walde, V. Champagne, and D. Cote: *JOM*, 2018, https://doi.org/10.1007/s11837-018-3175-7
4. C. Walde, D. Cote, V. Champagne, and R. Sisson: *JMEP*, 2018 https://doi.org/10.1007/s11665-018-3550-0

5. R. Mehrabian, B.H. Kear, and M. Cohen: *Rapid Solidification Processing. Principles and Technologies, II. Proceedings of the International Conference on Rapid Solidification Processing (2nd), March 23-26, 1980, Reston, Virginia USA*, (1980), pp 7-8, 22.
6. M.E. Fine: *Rapidly solidified powder aluminum alloys: a symposium* (No. 890). ASTM International, 1986, pp. 85.
7. W. J. Ullrich: *Powder Metallurgy in Defense Technology. Proceedings of the 1986 P/M in Defense Technology Seminar,* David Taylor Naval Ship Research & Development Center, December 3-4, 1986, Annapolis, Maryland, USA, 1986, pp 88.
8. G.E. Totten and D.S. MacKenzie: *Handbook of Aluminum: Vol. 1: Physical Metallurgy and Processes*, CRC Press, Boca Raton, FL, 2003, pp. 259-304.
9. A. Sabard, H. L. de Villiers Lovelock, and T. Hussain: *J. Therm. Spray Technol.,* 2018, ser. 1-2, vol. 27, pp. 145-158.
10. M. Rokni, C. Widener, and V. Champagne: *J. Therm. Spray Technol.,* 2014, vol. 23**,** p. 514.
11. M. Rokni, C. Widener, V. Champagne, G. Crawford, and S. Nutt: *Surf. Coatings Technol.,* 2017, vol. 310**,** pp. 278-285.
12. M. Rokni, C. Widener, O. Ozdemir, and G. Crawford: *Surf. Coatings Technol.,* 2017, vol. 309**,** pp. 641-650.
13. M. Rokni, C. Widener, G. Crawford, and M. West: *Mater. Sci. Eng. A,* 2015, vol. 625, pp. 19-27.
14. A. Sabard, H. de Villiers Lovelock, and T. Hussain: *J. Therm. Spray Technol.,* 2017, vol 27, pp. 145-158.
15. K. Tsaknopoulos: Worcester Polytechnic Institute, Worcester, MA, unpublished research, 2018.
16. ASTM E1097-12 Standard Guide for Determination of Various Elements by Direct Current Plasma Atomic Emission Spectrometry, ASTM International, West Conshohocken, PA, 2012, https://doi.org/10.1520/E1097-12
17. ASTM B209-10 Standard Specification for Aluminum and Aluminum-Alloy Sheet and Plate, ASTM International, West Conshohocken, PA, 2010, https://doi.org/10.1520/B0209-10

9 Phase Transformations in Al 5056 Powder

Phase Transformations in Gas-Atomized Al 5056 Powder

Kyle Tsaknopoulos[a] (klfitzpatricksch@wpi.edu), Caitlin Walde[a] (cewalde@wpi.edu), Derek Tsaknopoulos[a] (dgtsaknopoulos@wpi.edu), Victor Champagne, Jr. [b] (victor.k.champagne.civ@mail.mil), Danielle Cote[a*] (dlcote2@wpi.edu)

[a]Worcester Polytechnic Institute, 100 Institute Road, Worcester, MA 01609 USA
[b]US Army Research Laboratory, Aberdeen Proving Ground, MD 21005-5069 USA

* Corresponding author
Email: dlcote2@wpi.edu
Phone: 508-831-6020
Worcester Polytechnic Institute
Attn: Danielle Cote
100 Institute Road
Washburn 315 – MTE
Worcester, MA 01609 USA

Declarations of interest: none

9.1 Abstract

Aluminum 5056 is a work-hardenable alloy known for its corrosion resistance and has applications in additive manufacturing. Understanding the secondary phases in Al 5056 powders is important for understanding the properties of the final parts. Through extensive TEM, STEM, and EDS, magnesium segregation, β-Al_3Mg_2, Mg_2Si, and $Al_{13}Fe_4$ were identified in the as-atomized condition. After thermal treatment, the magnesium segregation and β-Al_3Mg_2 dissolved, while $Al_{13}Fe_4$ and Mg_2Si coarsened. Additionally, β-Al_3Mg_2 and an AlCr phase precipitated after natural aging. This speaks to the shelf-life of these powders and the importance of proper treatment and storage to maintain consistent results.

9.2 Keywords

Powder, aluminum, cold spray, heat treatment, Thermo-Calc

9.3 Introduction

Aluminum 5056 is a work-hardenable alloy known for its high resistance to corrosion. Al 5xxx series alloys were developed in the 1930s to meet a need for higher strength sheet materials with good formability and weldability, as well as corrosion resistance [1]. Magnesium shortages during World War II decreased the production of Al-Mg alloys until the 1950s when new alloys were created with easier formability with the increase of manufacturing capabilities. These new Al 5xxx series alloys could be used in many forms including castings, extrusions, plates, sheets, and wires. These alloys are the only non-heat treatable aluminum alloys to be used as plates or cast [1]. Specifically, Al 5056 is used for automotive applications, weld wire, welded storage vessels, rivets for magnesium, and fasteners [2-4]. Due to its high corrosion resistance, this alloy is often used on parts that are exposed to marine environments such as boat hulls and gangplanks [2,4].

In powder form, this alloy has been used substantially for the solid-state metal additive manufacturing process, cold spray. In this process, the powder is fed through a nozzle at supersonic velocities towards a substrate, where the particles plastically deform and create layers [5]. Since this alloy is work hardenable, it is able to exploit the work hardening effects of the cold spray process, making Al 5065 a logical choice for a feedstock material [6]. There have been two main applications of Al 5056 powder in cold spray. The first is a composite coating of SiC and Al 5056. This composite mixture leads to reinforcement of the aluminum matrix to improve hardness and wear resistance, and properties can be controlled through the ratio of SiC to Al 5056 in the powder [7-9]. The addition of these SiC particles was also shown to reduce the porosity in the coating. Since cold spray can only be used on ductile materials, the use of Al 5056 powder allows for ceramic particles to be used in the cold spray process [9]. The second application is the use of Al 5056 for cold spray repair of magnesium rotorcraft components [10-12]. The alloy was chosen to help make improvements to the corrosion resistance of the magnesium alloy [11]. The magnesium rotorcraft parts generally failed due to galvanic corrosion, and since Al 5056 has a high magnesium content, it was chosen to help reduce this

phenomenon. Al 5056 powder has also been used as a cold sprayed transition material between a magnesium alloy and Al 6061 substrates using fraction stir welding [13].
In the feedstock powder, the secondary phases present and phase transformations that occur during solidification, processing, and in service in aluminum alloys are largely dependent upon the exact alloying composition, and these phases play an important role in the properties and performance. The principle alloying element for this alloy is magnesium, which produces high strength, due to solid solution strengthening, that is directly proportional to the magnesium content in ranges up to 6 wt % [3]. An increased magnesium content increases the strength without excessively decreasing the ductility [4]. Titanium is added as a grain refiner, while manganese and chromium can correct for the corroding effect of iron, which is an impurity in aluminum alloys [14].

Since the aluminum matrix is super saturated with magnesium, there is a high driving force for the precipitation of β-Al_3Mg_2 phase [1]. Due to the low solubility of Mg_2Si in the aluminum matrix for this alloy, Mg_2Si can be seen as a major phase. The presence of chromium in this alloy leads to the formation of sub-microscopic intermetallic particles, $Al_{12}Mg_2Cr$. The addition of manganese leads to the formation of sub-microscopic $Al_6(Mn,Fe)$, as well as larger versions of that intermetallic. The presence of these intermetallics do not adversely affect its corrosion resistance, however, coarsened manganese and chromium particles can reduce ductility [4,14]. Al-Fe coarse intermetallic particles, including $Al_{12}(Fe,Mn)_3Si$, and Al_3Fe, reduce ductility as well as creep and fatigue resistance [14,1]. When the silicon solute is bound in Mg_2Si in this alloy, manganese precipitates as a dispersoid, favorably as $Al_6(Mn,Fe)$ over other aluminum-iron phases.

While in service, thermal variations can affect the microstructure. While the aluminum matrix is supersaturated with magnesium, it is mostly stable at room temperature, but precipitation of β-Al_3Mg_2 can be hastened by deformation and elevated temperatures, where it then precipitates on grain boundaries and shear bands. If β-Al_3Mg_2 forms at high temperatures (above 260°C) stable β-Al_3Mg_2 will form, but at room temperature, β' will form first. β' is very stable at low temperatures, and does not readily evolve to equilibrium phases, even after long aging times. Precipitation of β-Al_3Mg_2 leads to softening, and at grain boundaries, decreases corrosion resistance acting as an anodic phase to the matrix [1]. Additionally, the presence of β-Al_3Mg_2 at grain boundaries leads to intergranular cracking and stress corrosion [4]. Additionally, the $Al_{18}Mg_3Cr_2$ phase and $Al_6(Mn,Fe)$ phase can precipitate during ingot preheating, therefore special attention should be given to these phases during thermal changes [4,1].
Since Al 5056 is not an age hardenable alloy, it is typically not thermally treated in the conventional way. However, literature has shown that applying a solution treatment with subsequent natural aging, while it does not increase the strength of the alloy, can double the % elongation of the alloy [14]. Research on Al 5056 powder for cold spray has shown that heat treatment at 400°C for 6 hours has been used to degas the powder to reduce sintering during processing [12]. This process also led to a more homogenous distribution of magnesium in the matrix.

9.4 Materials and Methods

Commercially available (Valimet, Stockton, CA) gas-atomized Al 5056 powder was studied; the composition is in compliance with ASTM B316 (Table 1) and had a size distribution with d_{10} of 27.8 μm, d_{50} of 37.0 μm, and d_{90} of 52.3 μm [15].

Table 1. Composition of Al 5056 Powder, as determined via direct current plasma emission spectroscopy [16].

Element	Wt%
Chromium	0.15
Copper	0.013
Iron	0.11
Magnesium	5.38
Manganese	0.16
Silicon	0.050
Zinc	0.005
Total others each	< 0.05
Total others	< 0.15
Aluminum	Remainder

Thermodynamic and kinetic modeling software can aide in understanding the structure and processing of metallic alloy systems. The commercially available software, Thermo-Calc (Solona, Sweden), was utilized to create equilibrium and Scheil solidification diagrams (Figure 1). These diagrams provided insight into the internal microstructure of the powder by predicting secondary phases present in various conditions.

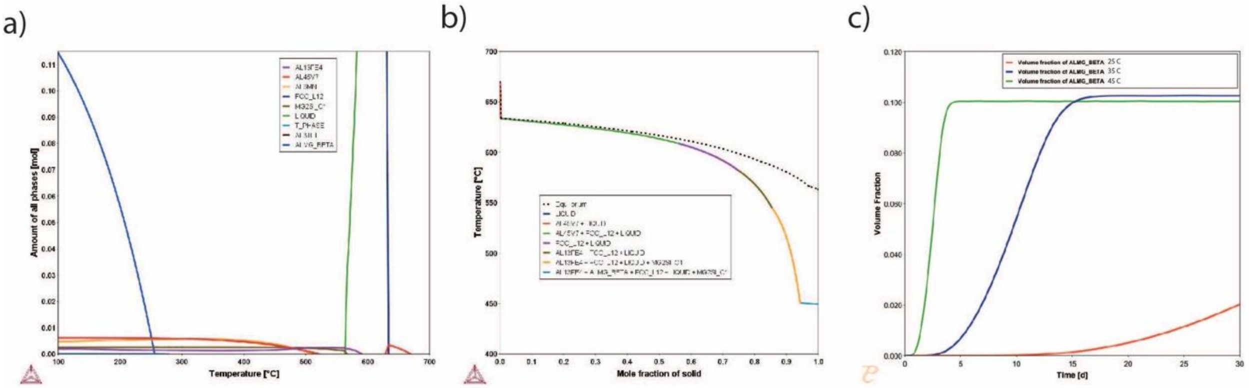

Figure 1: Thermodynamic and kinetic models produced using Thermo-Calc. a) Equilibrium diagram, and b) Scheil (non-equilibrium) solidification diagram c) Volume fraction as a function of time for β-Al_3Mg_2 Precipitate. All created using the TCAl5 Aluminum database and the measured chemical composition of the Al 5056 powder.

While Al 5056 is typically not considered a heat treatable alloy, solution treatment can be applied to homogenize the microstructure. The equilibrium property diagram (Figure 1a) was consulted when choosing a treatment temperature. 530˚C was chosen; it is below the melting temperature and above the dissolution temperature of Mg_2Si for this specific composition. A treatment time of 1 hour was chosen as it has been shown that the treatment times for gas-atomized powders are much shorter than typical solution treatment times [17-19]. A differential scanning calorimeter (DSC) (TA Instruments Discovery DSC with LN2P cooler) was used to thermally process the powder, due to the high level of control of heating and cooling rates, at a heating rate of 50 °C/ min and a cooling rate of 120 °C/min with a nitrogen purge gas. It has been shown that SEM is insufficient to show secondary phases of a few micron diameter; therefore, TEM is preferred [17-20]. Samples were created for TEM imaging using a gallium focused ion beam (FIB) (FEI Helios 660 Nanolab and FEI Scios Dual Beam FIBs) in a method similar to that employed by Tsaknopoulos et al. [18]. Parallel-sided lamellas of the powder particles of varying dimensions were produced. For EDS elemental quantification, samples of thicknesses below 100 nm were created to eliminate interaction from the matrix and other phases with the phase under consideration.

TEM, STEM, and EDS micrographs were collected using a Probe-corrected TEM (FEI Titan Themis 300 S/TEM with ChemiSTEM technology, and Super-X EDS system). All analysis was performed at 300 kV.

9.5 Results and Discussion

Figure 2 displays a low magnification HAADF and EDS maps representative of the as-atomized Al 5056 internal microstructure; regions of magnesium segregation, dispersed iron intermetallic phases at the grain boundaries, and some Mg_2Si also at the grain boundaries are seen. Figure 3a shows a STEM HAADF micrograph and corresponding STEM EDS maps at a high magnification of a grain boundary. This demonstrates the presence of flower-like disks of an iron intermetallic, as well as a dark contrasting AlMg phase. These are dispersed in the magnesium segregation in this alloy, which was caused by its very high magnesium content. This difference between this magnesium segregation and the AlMg phase is very evident in the magnesium EDS maps. Figure 3b shows a similar micrograph also with the presence of an MgSi phase at a grain corner. Elemental quantification was used to identify these phases: $Al_{13}Fe_4$, β-Al_3Mg_2, and Mg_2Si. This matches the phases predicted by Scheil solidification as seen in Figure 1b. It has been shown that Scheil solidification predictions are valid for powders due to their rapidly solidified nature [17-19]. The magnesium segregation can be homogenized using thermal treatment to improve the properties of the powder [12].

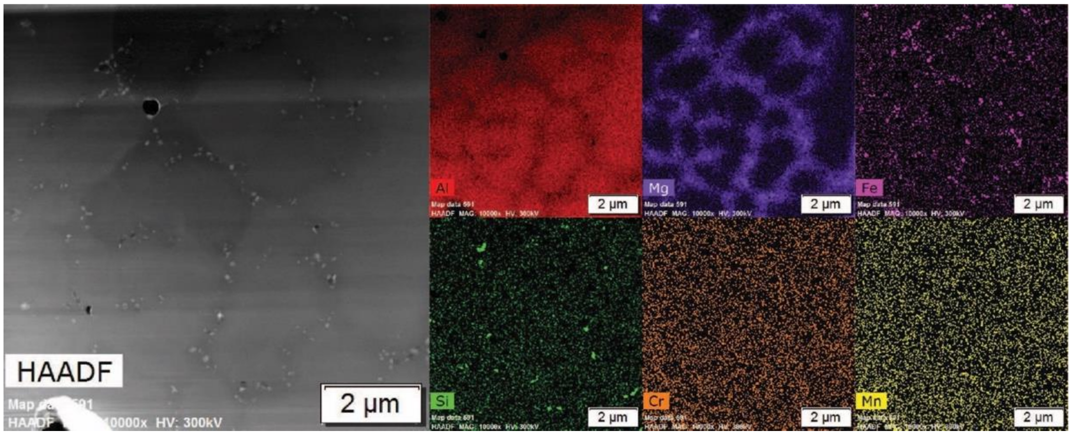

Figure 2: Low magnification TEM micrographs of the as-atomized condition; a) HAADF, and EDS maps of b) Al, c) Cr, d) Fe, e) Mg, f) Mn, and g) Si.

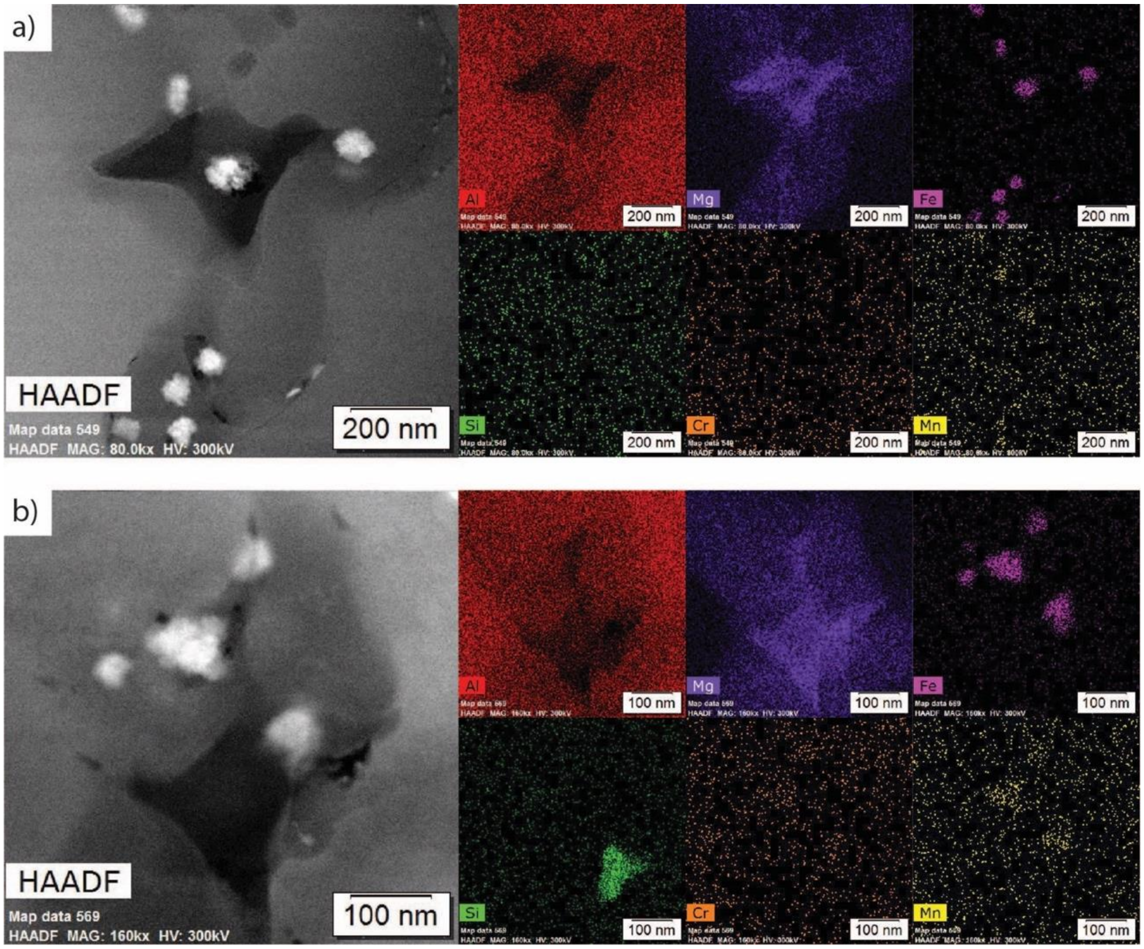

Figure 3: High magnification TEM micrographs of the as-atomized condition showing a) a grain boundary with an Fe-intermetallic (light contrasting) and Al-Mg β (dark contrasting), as well as Mg-segregation; and b) a grain corner featuring the same Fe-intermetallic (light contrasting), Mg_2Si (dark contrasting), and two types of Al-Mg β.

A thermal treatment of 530°C for 1 hour was evaluated in this study. Figure 4 shows STEM HAADF micrographs and corresponding EDS maps of the microstructure of the thermally treated condition. Note the presence of some residual coarsened Mg_2Si at grain corners, while most has dissolved. Additionally, magnesium solute segregation at the grain boundaries has equilibrated throughout the matrix and the β-Al_3Mg_2 has dissolved. Note the large and small bright contrasting phases at the grain boundaries in the HAADF image. The majority of these bright contrasting phases are coarsened $Al_{13}Fe_4$, with the largest phases present at grain corners. Based on the equilibrium diagram in Figure 1, Mg2Si is stable in very small amounts at the treatment temperature of 530°C; this is consistent with that was seen in the micrographs. Figure 1 demonstrates that the β-Al_3Mg_2 will dissolve by 250°C, which confirms the dissolution seen in the micrographs. Additionally, Figure 1 indicates that $Al_{13}Fe_4$ is more stable at the treatment temperature, thus leading to the coarsening seen in the micrographs. It has been shown that the homogenization of these powders leads to softening, which leads to improved deformation and bonding in cold spray deposits [12]. Additionally, research has shown that coarse AlFe precipitates have low bond strength with the matrix, causing the material to be more brittle, and can act as crack initiation sites, both of which negatively affects the mechanical properties [21,22]. Given this, it is important to heat treat the powder to homogenize the magnesium segregation to improve ductility without coarsening the $Al_{13}Fe_4$. Thermodynamic models can be used further to optimize the thermal treatment parameters to yield the desired internal microstructure for the best cold spray properties.

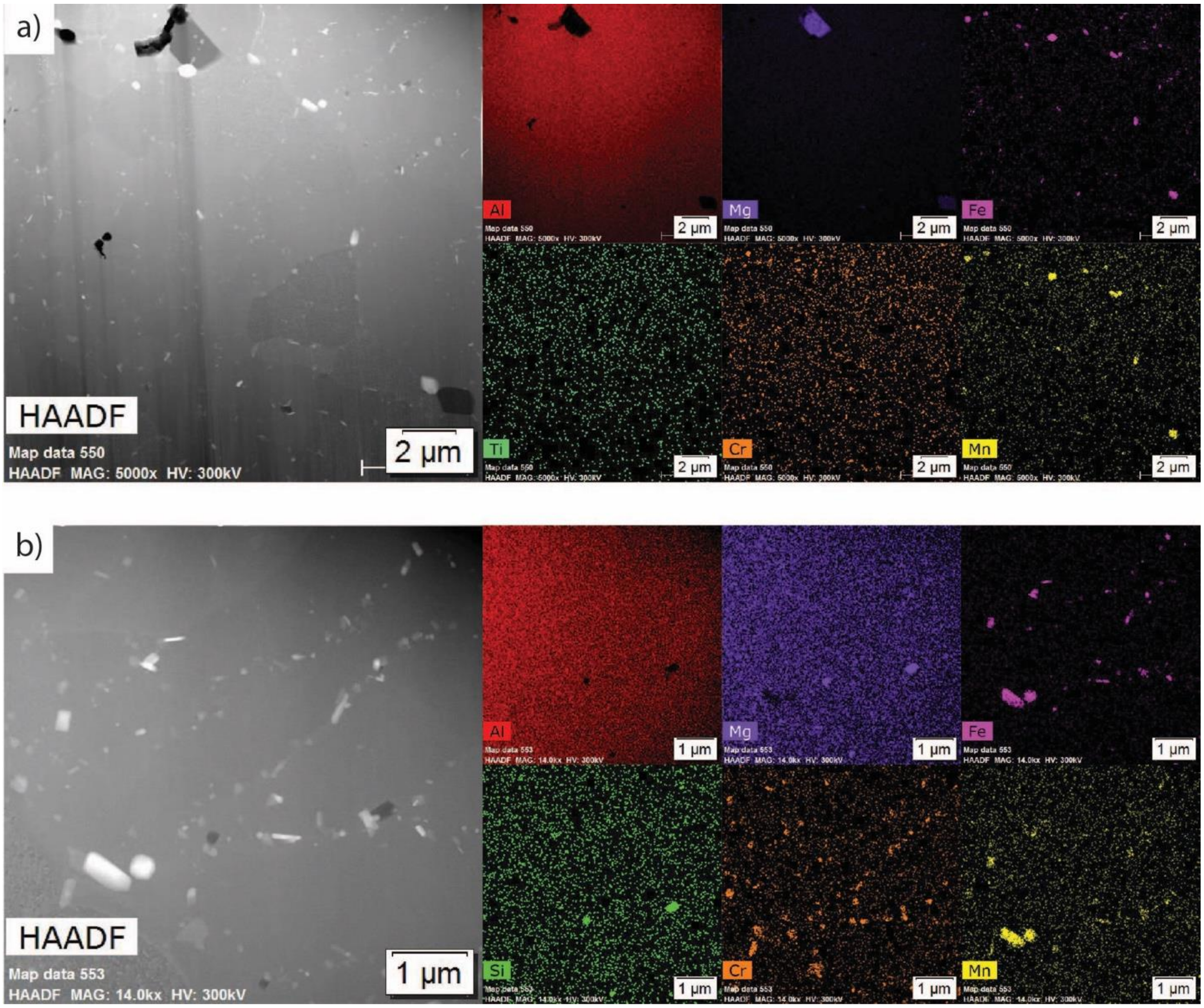

Figure 4: TEM micrographs and corresponding EDS maps of the thermally treated condition for a) low magnification and b) high magnification.

Due to the super saturated solid solution in Al 5056, natural aging can occur. In the as-atomized condition of this sample, natural aging was seen in the form of nano β-Al_3Mg_2 particles of about 10-20nm. These are generally seen growing on the boundaries of other phases as well as along grain boundaries, as seen as the small black contrasting dots in Figure 3a and 3b. Unlike the larger β-Al_3Mg_2 that formed during initial atomization, this β-Al_3Mg_2 has formed at room temperature over a longer period of time. Like the larger β-Al_3Mg_2 seen in these figures, the small β-Al_3Mg_2 also dissolves during heat treatment.

As was shown in Figure 4a, β-Al_3Mg_2 dissolved during heat treatment. After quenching, the sample was left at room temperature two days prior to being analyzed in the TEM. During this time, natural aging also occurred. During thermal treatment, as the phases in the as-atomized condition dissolved, the excess solute was homogenized into the matrix, further increasing the driving force for precipitation at room temperature due to the supersaturated matrix. Based on Figure 1, it is expected that the naturally aged phases could be β-Al_3Mg_2, $Al_{45}Cr_7$, Al_6Mn, Mg_2Si, and T-Phase at room temperature. Figure 4b shows a higher magnification STEM HAADF and corresponding EDS map for the micrograph in Figure 4a and demonstrates some of the naturally aged phases. Note the presence of many small (50nm) chromium-rich phases at the grain boundaries. Figure 1 suggests that this would be $Al_{45}Cr_7$, but EDS quantification indicated the presence of magnesium in this phase, suggesting a different AlCr intermetallic, potentially $Al_{12}Mg_2Cr$. The presence of β-Al_3Mg_2 was again seen growing on the coarsened $Al_{13}Fe_4$ intermetallics, while small amounts of T-phase were seen growing along grain boundaries. No Al_6Mn was seen in these TEM lamella but might be seen for other powder particles of this alloy composition as suggested by Figure 1 as Al_6Mn is stable at room temperature in small amounts. It has been shown that for Al 5000 series alloys, natural aging of these phase at the grain boundaries increases stress corrosion cracking [23-25]. This is relevant when considering the shelf life of powder, particularly after thermal treatment, before use in consolidation processes, such as cold spray. Thermodynamic and kinetic modeling can be used to simulate and understand the natural aging behavior of this alloy. Figure 1c shows volume fraction of β-Al_3Mg_2 as a function of time at various temperatures. At room temperature (25°C), this phase slowly grows over the course of a month. With increasing temperature, the growth rapidly accelerates, until 45°C where growth is much faster, plateauing to maximum precipitation in a matter of days. These variations can affect the mechanical properties and repeatability of the additively manufactured parts. This model simulates conditions in a lab (highly controlled), or in a large warehouse (large temperature fluctuations), enabling a better understanding of the environmental impacts on the natural aging of β-Al_3Mg_2 in Al 5056.

In order to fully understand the phase transformations between the as-atomized and thermally treated conditions, hot-stage TEM will be performed in future work. Special note will be given to the natural aging seen in this alloy.

9.6 Conclusion

Understanding the types and transformations of secondary phases in these powders is important for predicting and understanding the mechanical and corrosion properties of the final additively manufactured parts in which they are used. Through the use of extensive TEM, STEM, and EDS, this work identified the phases present in as-atomized and thermally treated gas-atomized Al 5056 powders. Along with magnesium-segregation, β-Al_3Mg_2, Mg_2Si, and $Al_{13}Fe_4$ were identified in the as-atomized condition. Even though Al 5056 is not considered a heat-treatable alloy, literature has shown that a solution treatment and subsequent aging can increase the % elongation in these alloys. Given the high deformation experienced by powder particles during the cold spray process, high % elongation is desirable. Additionally, degassing powders prior to use in additive manufacturing process has been shown to improve the properties of the final consolidated part. Given these, a solution treatment of 530 °C for one hour was applied to the powders. After thermal treatment, the magnesium segregation and β-Al_3Mg_2 dissolved, and the $Al_{13}Fe_4$ and Mg_2Si coarsened. Additionally, after 2-14 days of natural aging, the β-Al_3Mg_2 precipitated again with a small AlCr phase. This speaks to the shelf-life of these powders once after thermal treatment and the importance of proper treatment and storage to maintain consistent results.

9.7 Acknowledgements

This work was funded by the United States Army Research Laboratory, grant #W911NF-15-2-0024.

This work was performed in part at the *Kostas Advanced Nano-Characterization Facility in Kostas Research Institute at Northeastern University* and at the *Center for Nanoscale Systems (CNS)*, a member of the National Nanotechnology Coordinated Infrastructure Network (NNCI), which is supported by the National Science Foundation under NSF award no. 1541959.

9.8 References

1. Vasudevan, Asuri K., and Roger D. Doherty, eds. *Aluminum Alloys--Contemporary Research and Applications: Contemporary Research and Applications*. Vol. 31. Elsevier, 2012, p. 85-95.
2. Davis, Joseph R. *Aluminum and aluminum alloys*. ASM international, 1993, p. 2.
3. Wessel, James K. *The handbook of advanced materials: enabling new designs*. John Wiley & Sons, 2004, p. 321-464.
4. Davis, Joseph R., ed. *Alloying: understanding the basics*. ASM international, 2001, p. 351-416.
5. V.K. Champagne, *The Cold Spray Materials Deposition Process: Fundamentals and Applications* (Cambridge, England: Woodhead Publishing Limited, 2007), p. 1-10.
6. Champagne, Victor, Aaron Nardi, and Danielle Cote. "MATERIALS CHARACTERIZATION OF ADVANCED COLD-SPRAY ALUMINUM ALLOYS." *International Journal of Powder Metallurgy* 51.4 (2015).
7. Yu, M., Li, W. Y., Suo, X. K., & Liao, H. L. (2013). Effects of0 gas temperature and ceramic particle content on microstructure and microhardness of cold sprayed SiCp/Al 5056 composite coatings. *Surface and Coatings Technology*, *220*, 102-106.
8. Wang, Y., Normand, B., Mary, N., Yu, M., & Liao, H. (2014). Microstructure and corrosion behavior of cold sprayed SiCp/Al 5056 composite coatings. *Surface and Coatings Technology*, *251*, 264-275.
9. Yu, M., Suo, X. K., Li, W. Y., Wang, Y. Y., & Liao, H. L. (2014). Microstructure, mechanical property and wear performance of cold sprayed Al5056/SiCp composite coatings: effect of reinforcement content. *Applied Surface Science*, *289*, 188-196.
10. V.K. Champagne, *The Cold Spray Materials Deposition Process: Fundamentals and Applications,* Repair of Magnesium Components by Cold Spray Techniques*,* (Cambridge, England: Woodhead Publishing Limited, 2007), p. 327-351.
11. Champagne, Victor K. "The repair of magnesium rotorcraft components by cold spray." *Journal of Failure Analysis and Prevention* 8.2 (2008): 164-175.
12. Rokni, M. R., et al. "Effects of preprocessing on multi-direction properties of aluminum alloy cold-spray deposits." *Journal of Thermal Spray Technology* 27.5 (2018): 818-826.
13. Champagne, Victor Kenneth, et al. "Joining of cast ZE41A Mg to wrought 6061 Al by the cold spray process and friction stir welding." *Journal of Thermal Spray Technology* 25.1-2 (2016): 143-159.
14. Mondolfo, Lucio F. *Aluminum alloys: structure and properties,* Commercial Alloys: Aluminum-Magnesium, Aluminum-Manganese Alloys, Elsevier, 2013, p. 806-841.
15. ASTM B316/B316M-15 Standard Specification for Aluminum and Aluminum-Alloy Rivet and Cold-Heading Wire and Rods, ASTM International, West Conshohocken, PA, 2015, https://doi.org/10.1520/B0316_B0316M-15

16. ASTM E1097-12(2017) Standard Guide for Determination of Various Elements by Direct Current Plasma Atomic Emission Spectrometry, West Conshohocken, PA, 2017, https://doi.org/10.1520/E1097-12R17
17. Walde, Caitlin, et al. "Characterizing the effect of thermal processing on feedstock Al alloy powder for additive manufacturing applications." *Journal of Materials Engineering and Performance* 28.2 (2019): 601-610.
18. Tsaknopoulos, Kyle, et al. "Gas-Atomized Al 6061 Powder: Phase Identification and Evolution During Thermal Treatment." *JOM* 71.1 (2019): 435-443.
19. Walde, Caitlin, et al. "The Microstructural Evolution of Rapidly Solidified Powder Aluminum 2024 During Thermal Processing." *Metallography, Microstructure, and Analysis*: 1-11.
20. Bedard, Benjamin A., et al. "Microstructure and micromechanical response in gas-atomized Al 6061 alloy powder and cold-sprayed splats." *Journal of Thermal Spray Technology* 27.8 (2018): 1563-1578.
21. Shabestari, S. G. (2004). The effect of iron and manganese on the formation of intermetallic compounds in aluminum–silicon alloys. *Materials Science and Engineering: A*, *383*(2), 289-298.
22. Yi, J. Z., Gao, Y. X., Lee, P. D., & Lindley, T. C. (2004). Effect of Fe-content on fatigue crack initiation and propagation in a cast aluminum–silicon alloy (A356–T6). *Materials Science and Engineering: A*, *386*(1-2), 396-407.
23. R. B. NIEDERBERGER, J. L BASIL, G. T. BEDFORD, Corrosion and Stress Corrosion of 5000-Series Al Alloys in Marine Environments, CORROSION. 1966;22(3):68-73. https://doi.org/10.5006/0010-9312-22.3.68
24. Cobb, A., Macha, E., Bartlett, J., & Xia, Y. (2017, February). Detecting sensitization in aluminum alloys using acoustic resonance and EMAT ultrasound. In *AIP Conference Proceedings* (Vol. 1806, No. 1, p. 050001). AIP Publishing. https://aip.scitation.org/doi/pdf/10.1063/1.4974595
25. Kramer, L., Phillippi, M., Tack, W. T., & Wong, C. (2012). Locally reversing sensitization in 5xxx aluminum plate. *Journal of materials engineering and performance*, *21*(6), 1025-1029.

10 Modeling Dissolution and Growth of Secondary Phases

DICTRA software can be used to model both the growth and dissolution of secondary phases within metallic alloy systems. The specific model used to achieve this is a moving boundary problem. Figure 1 demonstrates in infographic where two regions are composed of two adjacent phases, alpha and beta, where the migration of the boundary between the two is modeled, with specific interest in the velocity (v) of the interface. This model assumes that all substitutional elements have the same volume, interstitial elements have zero molar volumes, thermodynamic equilibrium holds locally at all phase interfaces, and there is no diffusion in secondary phase as no data is available in the Thermo-Calc mobility database. This model uses both the thermodynamic and mobility Thermo-Calc databases (TCAL4 and MOBAL3). Inputs for this model include system elements, phases, treatment temperature, regions, initial size of precipitate, width of the region, initial composition of phases, phase geometry, and simulation time. Many of these parameters are found using the experimental characterization discussed in Chapters 5-9.

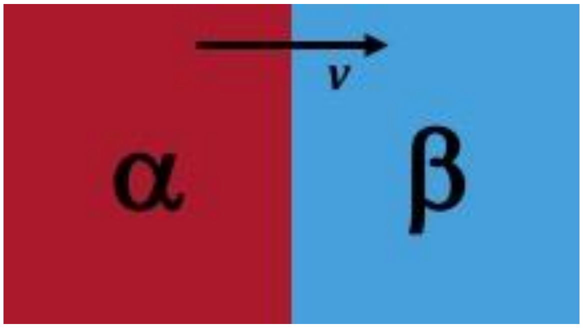

Figure 1. Diagram demonstrating the moving boundary model in DICTRA.

10.1 Al 6061 DICTRA Dissolution and Growth Results

Preliminary models have been computed for Al 6061 powder to further understand the phase transformations of the as-atomized powder particles after thermal treatment. As determined through the work in Chapters 6 and 7, the phases found in the as-atomized powder particles are Mg_2Si and $Al_{13}Fe_4$. This section will focus on the dissolution of Mg_2Si and the growth of $Al_{13}Fe_4$. The alpha phase from Figure 1 here is the FCC Aluminum matrix, and beta is the secondary phase, Mg_2Si or $Al_{13}Fe_4$. The velocity of the boundary will switch directions depending on if the phase will be growing or dissolving.

The results from this model are shown in Figures 2-4. Figure 2 shows the volume fraction of Mg_2Si in the 6061 matrix as a function of time for varying temperatures close to the 530°C used as the solutionization temperature in the experimental work. At the lower temperatures, 500-525°C, shown in Figure 2a, the Mg_2Si is expected to increase its volume fraction and then become stable after about 20 minutes. As the temperature increases to about 530°C, as seen in Figure 2b, the Mg_2Si will start to rapidly dissolve, which is comparable with what was seen experimentally in Chapter 6. Figure 3 demonstrates the volume fraction of $Al_{13}Fe_4$ as a function of time for the same varying temperature. Unlike the Mg_2Si, the $Al_{13}Fe_4$ is continually growing at all temperatures.

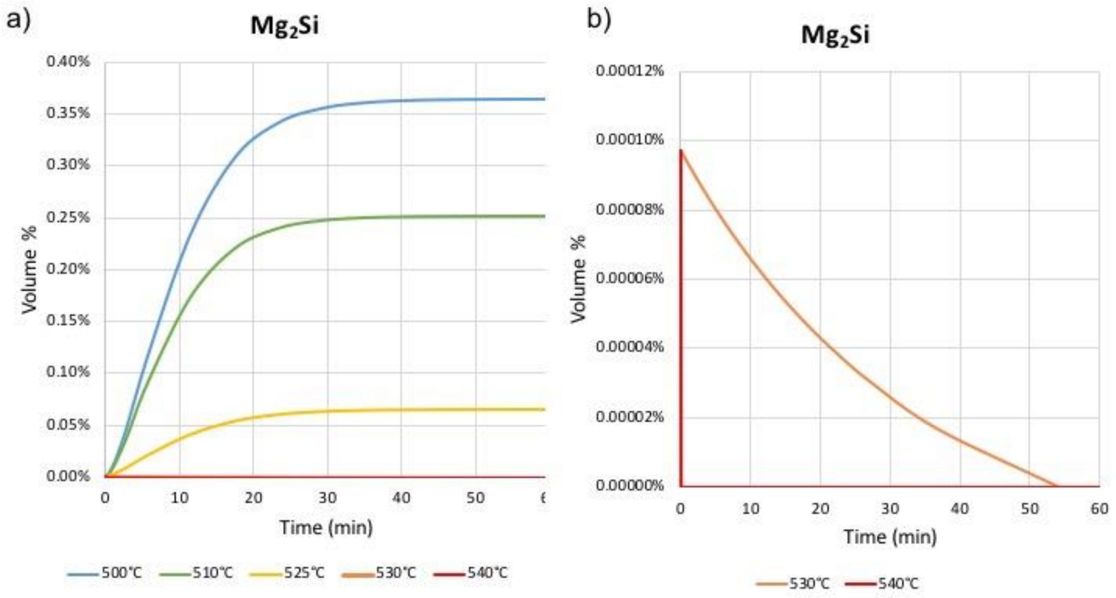

Figure 2. Volume fraction as a function of time for varying temperatures between 500℃ and 540℃ for a) Mg_2Si b) an increase magnification of 2a.

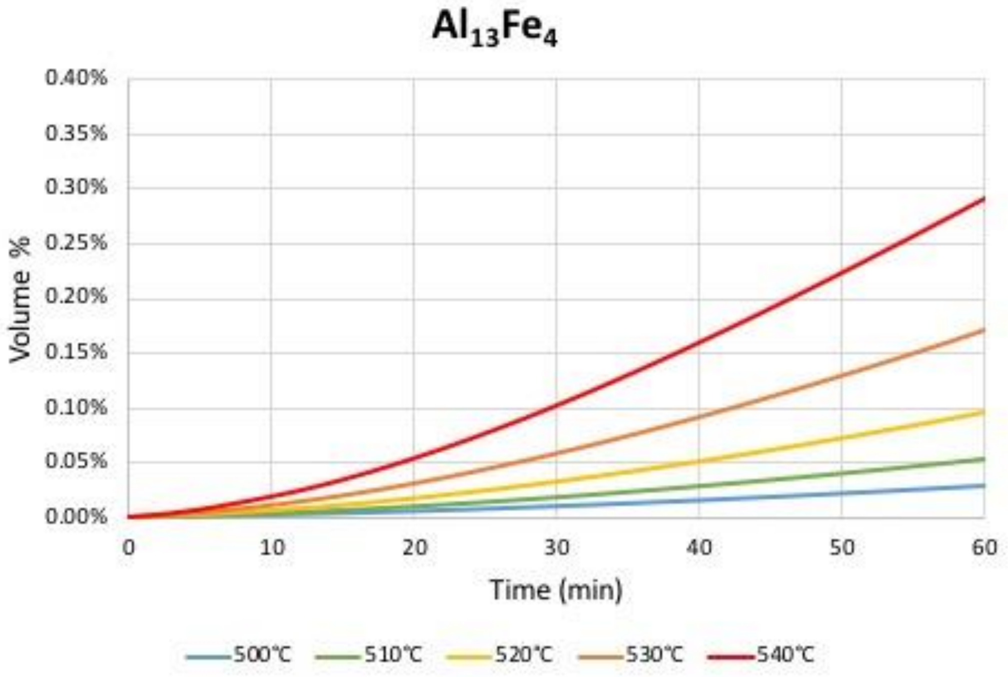

Figure 3. Volume fraction as a function of time for varying temperatures between 500℃ and 540℃ for $Al_{13}Fe_4$.

Figure 4 shows a similar trend for the phase diameter as function of temperature. The Mg_2Si grows and becomes stable at the lower temperatures, but dissolves above 530°C, while $Al_{13}Fe_4$ continues to increase in diameter as a function of time. These models will help to give insight into the internal microstructure of the powder particles during thermal treatment in the Al 6061 powder.

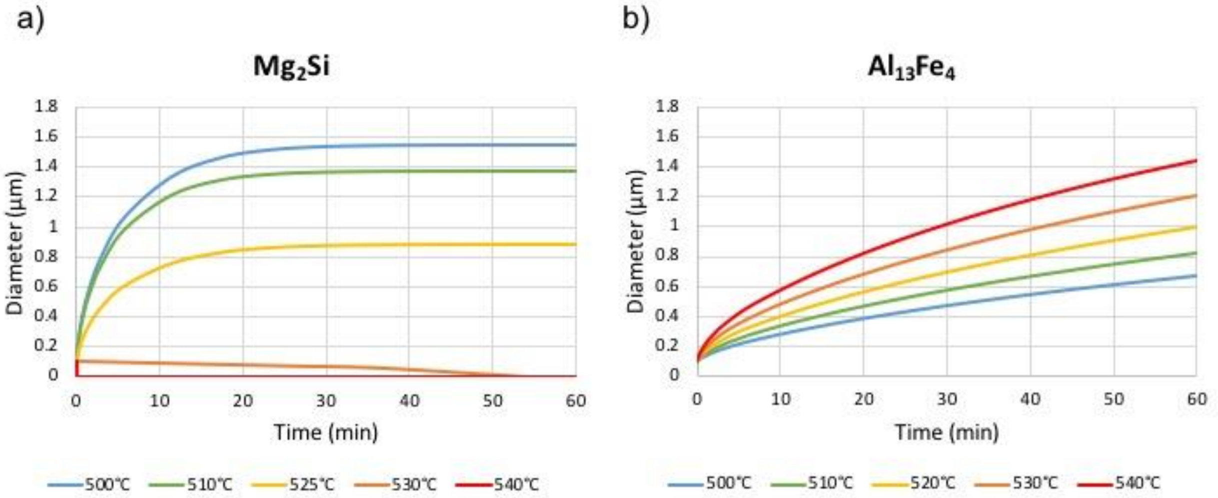

Figure 4. Average Diameter as a function of time for varying temperatures between 500℃ and 540℃ for a) Mg_2Si and b) $Al_{13}Fe_4$.

10.2 Al 5056 Dissolution and Growth Results

A preliminary hot stage TEM study was conducted using Al 5056 powder. In this study the sample was ramped up to 450°C at 1°C/second and held for 60 minutes before quenching. This experiment was conducted by group member Matt Gleason in partnership with collaborators at the University of Connecticut [1]. Figure 5a shows the microstructure of the Al 5056 powder prior to heating. There are two notable types of phases seen in this image, a light contrasting, and a dark contrasting phase. Given the phase identification completed in Chapter 9, these phases in the as-atomized powder have been identified as $Al_{13}Fe_4$ (light contrasting, numbers 1-4 in Figure 5a) and Al_3Mg_2 β (dark contrasting, A and B in Figure 5a). Figure 5b demonstrates the microstructure of the powder after heating at 450°C for 1 hour. The dark contrasting Al_3Mg_2 β has dissolved, while the light contrasting $Al_{13}Fe_4$ has coarsened, and also dissolved. Figure 6 gives a graphical representation of the mean radius of these secondary phases as a function of time during the 60 minute experiment. This data was extracted from the still images taken throughout the 60 minute experiment using image thresholding software to determine the mean radius of the phases. The data for the four $Al_{13}Fe_4$ phases are found in blue, while the Al_3Mg_2 β phases are found in orange. The red vertical line signifies the time at which the experiment was up to the final temperature 450°C; prior to this line, the sample was ramping up to temperature at 1°C/second. During the ramp, all secondary phases appear to be growing in size. This aligns with the thermodynamic models; at temperatures below 300°C we would expect Al_3Mg_2 β to grow according to the equilibrium diagram found in Figure 1 in Chapter 9. $Al_{13}Fe_4$ is expected to remain relatively constant at low temperature, and coarsen with increasing temperature. Figure 6 demonstrates both these trends. After reaching a critical temperature above 300°C (at about 5 minutes), the Al_3Mg_2 β begins to rapidly dissolve. The $Al_{13}Fe_4$ appears to be growing during the ramp, but for phases 1-3, the phase tapers to a steady size for the duration of the experiment. Phase 4 appears to have dissolved after 35 minutes. This is likely due to its small size, which caused it to dissolve and redistribute the elements to the other phases in the area. It is important to note that the image thresholding used to extract the data in Figure 6 can be an extremely subjective process, which accounts for the small highs and lows within the data. Additional issues include image quality, as the thresholding uses light and dark contrast, and user error. Additional work will be done to automate this thresholding process in the future for more accurate results.

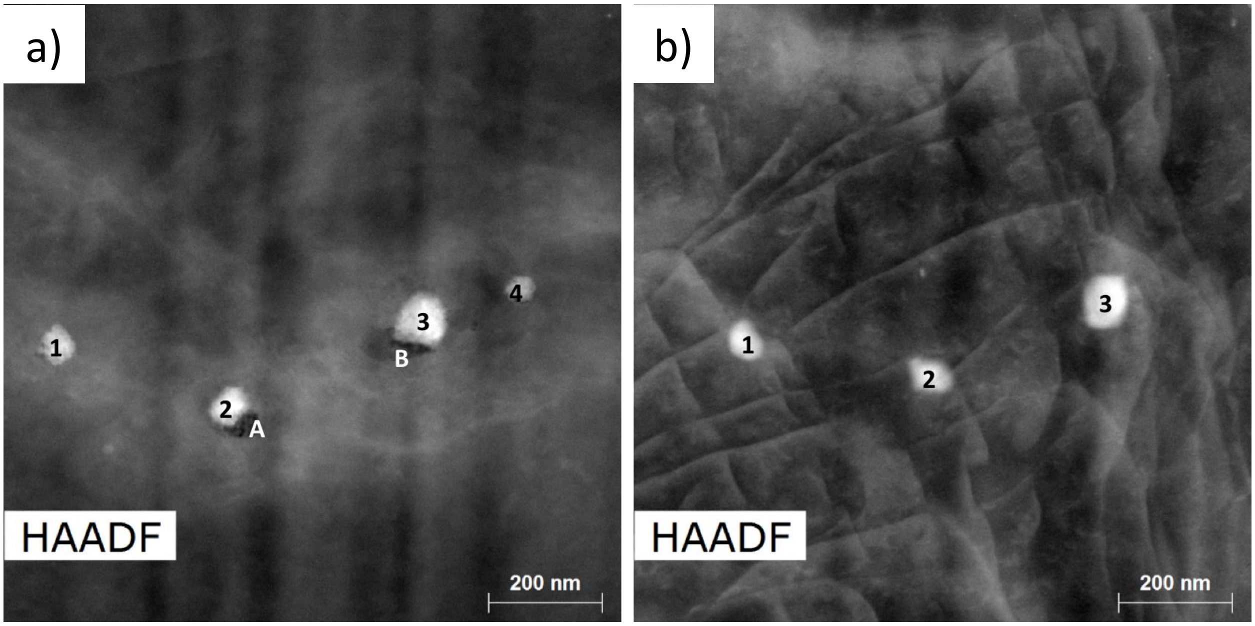

Figure 5. HAADF TEM micrographs of Al 5056 powder before (a) and after (b) thermal treatment at 450°C for 60 minutes. Secondary phases are numbered for comparison [1].

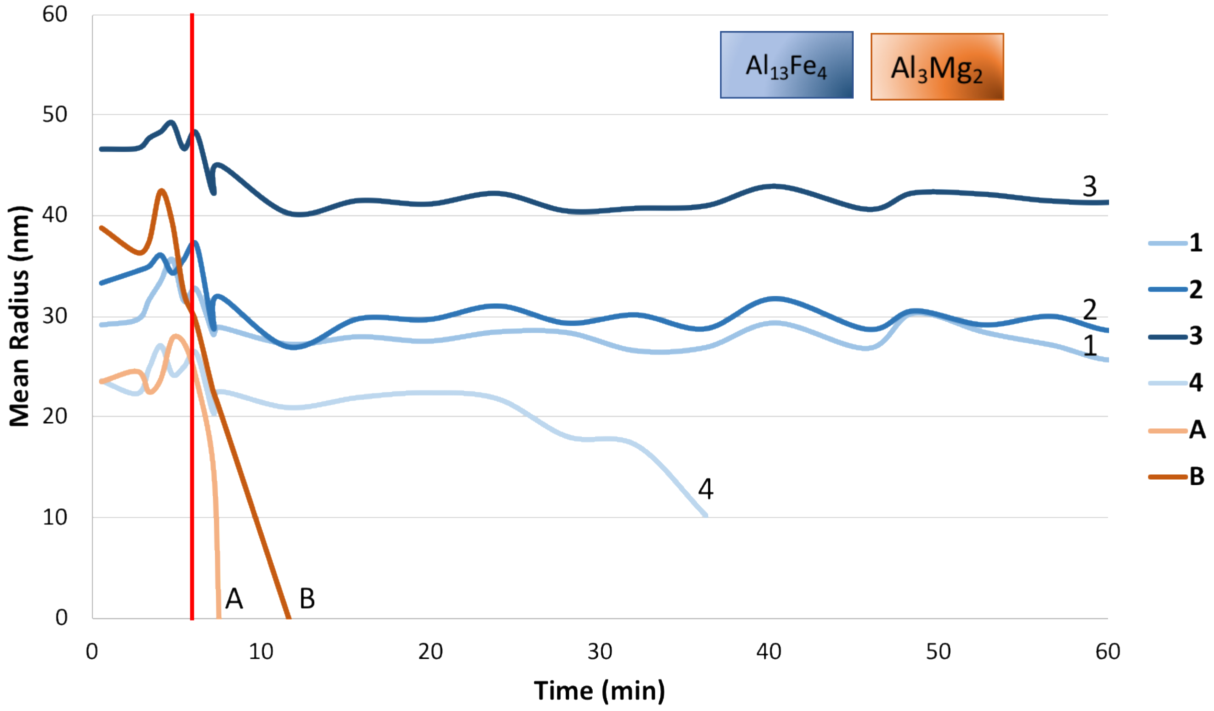

Figure 6. Mean radius vs time data for secondary phase particles in Al 5056 powder. Phases 1-4 in blue are $Al_{13}Fe_4$, and phases A and B in orange are Al_3Mg_2.

Given the data extracted from the hot stage TEM experiment, DICTRA can be used to help understand the phase transformations in the material. Figure 7 demonstrates the DICTRA output for both $Al_{13}Fe_4$ and Al_3Mg_2. For similar sized particles to those found in the as-atomized Al 5056 powder from the TEM experiment, a DICTRA model can be run at the same conditions; 450°C for 60 minutes. The trends found in these graphs are similar those seen in the experiment. The Al_3Mg_2 phases in Figure 7 dissolve almost instantaneously at 450°C which is depicted by the sharp drop down to zero at the beginning of the simulation, while the $Al_{13}Fe_4$ phases will continue to slowly coarsen throughout the length of the experiment.

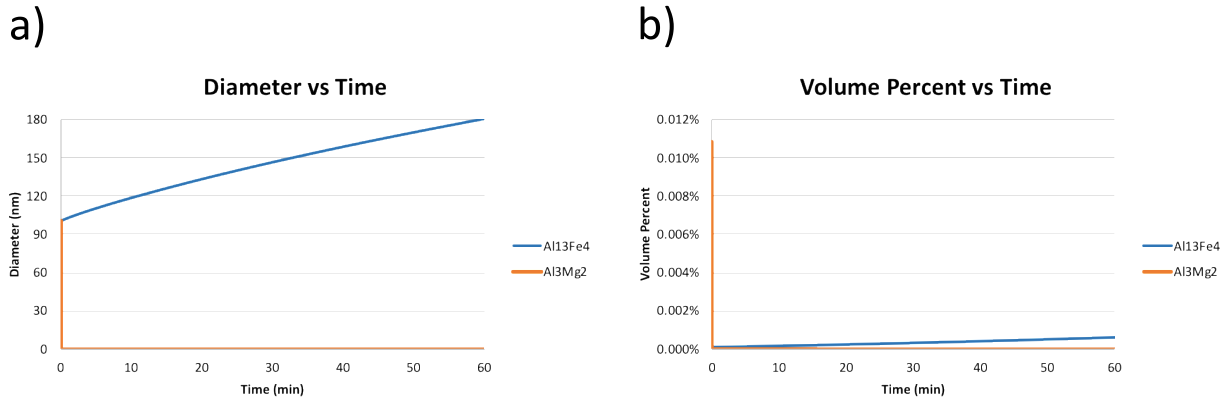

Figure 7. a) Diameter as a function of time, b) Volume Percent of phase as a function of time for both $Al_{13}Fe_4$ and Al_3Mg_2 phases calculated by DICTRA.

In addition to DICTRA dissolution models, the Thermo-Calc software can be used to create precipitation models using PRISMA. Figure 8 demonstrates similar trends to those found from the DICTRA simulations. The $Al_{13}Fe_4$ phases stay relatively constant in size and volume faction, with slight coarsening over time, while the Al_3Mg_2 shows rapid dissolution. While these two software use similar datasets and export similar results, they can be used to look at dissolution and growth at different scales. DICTRA is especially useful when modeling a single secondary phase of a particular size, while PRISMA can be used to similar many phases of a size distribution within an alloy. Both types of software used simultaneously can help to give a complete picture of the phase transformations in materials.

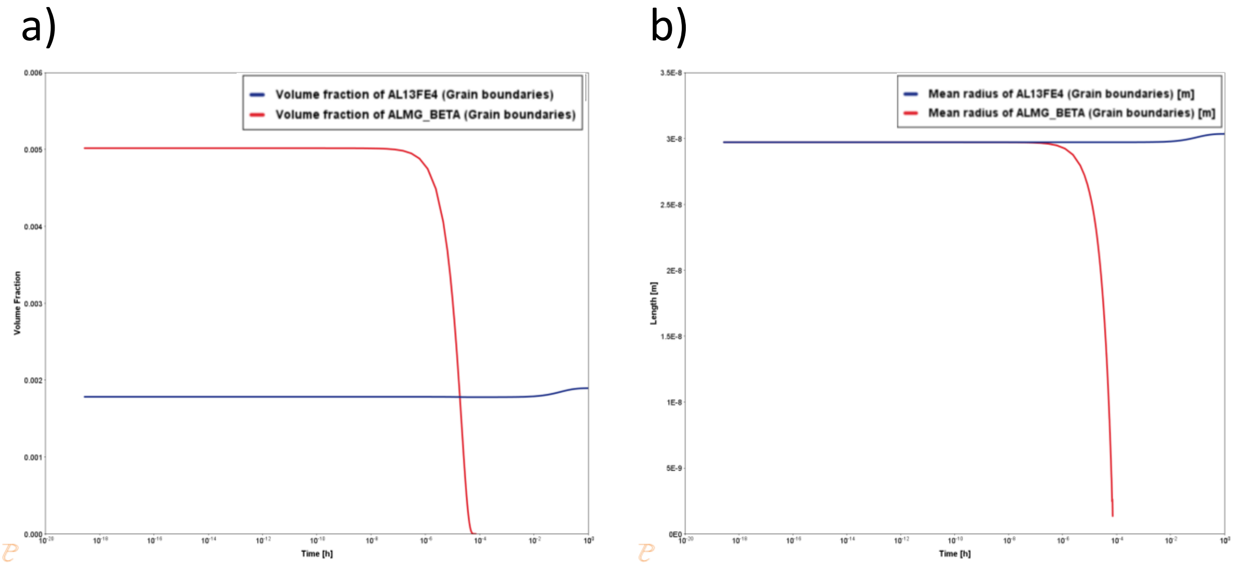

Figure 8. a) Volume fraction as a function of time b) length of phase as a function of time for $Al_{13}Fe_4$ and Al_3Mg_2 (Beta) both calculated using Thermo-Calc's PRISMA.

The models will be validated and calibrated using the experimental results in Chapters 5-9, and allow for use in new situations. Experimental characterization of powders is a very time-consuming process, but the need for lots of experimental work can be decrease by using models to describe thermal treatment processes without performing them. Further experimental work is needed for the calibration of these models, as will be described in the Future Work Chapter.

10.3 References

1. Vijayan, S., Bedard, B.A., Gleason, M.A. et al. J Mater Sci (2019). https://doi.org/10.1007/s10853-019-03562-0

11 Discussion

Chapters 4-10 demonstrate the work done to understand the effect of thermal treatment on internal powder microstructure. Although the homogenization models performed in Chapter 4.1 proved to be invalid for these powders, they led to a deeper investigation described in Chapter 4.2 for understanding the as-atomized powder microstructure. This set the framework for the phase identification described in Chapters 5-9. This identification of phases allowed for the use of the DICTRA models for dissolution and growth of secondary phases in the aluminum alloy powders. These models will ultimately help in the optimization of powder microstructure by understanding how the thermal treatment of these powders changes the internal microstructure without the need for extensive experimental characterization.

- Chemical Segregation in Al Powders
    - Metallic feedstock is used for many additive manufacturing processes, including the solid state additive manufacturing process, Cold Spray. In previous Cold Spray literature, some preliminary work had been done on understanding the internal microstructure of the metallic feedstock powder, specifically Aluminum powders. That work suggested the presence of chemical solute segregation at the grain boundaries of these aluminum alloy powders. This work will disprove the idea that there is chemical segregation within gas atomized Al powder particles. Initial segregation during the atomization process is turned to network phases at the grain boundaries during the rapid solidification process. Three alloys, Al 2024, Al 7075, and Al 6061 were studied to depict the presence of network type phases at the grain boundaries of these powder particles. Analysis was done using scanning electron microscope (SEM), transmission electron microscope (TEM), electron dispersive x-ray spectroscopy (EDS), and x-ray diffraction (XRD) to understand the presence of phases in these powders. The use of computational modeling aided in the understanding of the powder microstructure. Based on these models and experimental results, the presence of S-phase and Al_2Cu in 2024, and η and Al_7Cu_2Fe phases in 7075, and Mg2Si and an AlFe intermetallic in 6061 were found.
- Phase Identification in Al 2024 Powder
    - Gas-atomized metallic powders are commonly used in solid state deposition processes, such as Cold Spray and Additive Friction Stir. While their post-process consolidated properties are widely studied, there is little research on the properties of the powders before processing. Understanding the powder characteristics before use in additive manufacturing could lead to fine-tuning properties of additively manufactured materials. This research studied the effect of various thermal treatment processes on the characteristics and microstructural evolution of powder aluminum alloy 2024. Treatment times and temperatures were guided by thermodynamic modeling. Light microscopy, scanning electron microscopy, transmission electron microscopy, energy dispersive x-ray spectroscopy, electron backscatter diffraction, and differential scanning calorimetry were used to evaluate each condition. Thermodynamic

    models were used to predict the phase stability in these powders, and were calibrated using the experimental results to give a more complete understanding of the phase transformations during thermal processing.

- Phase Identification of Mg Phases in Al 6061 Powder
    - Metal additive manufacturing processes often use gas atomized powder as feedstock; these processes use different methods for consolidation. Depending on the consolidation temperature, secondary phases may be retained during processing, making it important to understand powder microstructure prior to consolidation. Commercial alloy compositions are typically used for these powders because they have been widely studied and qualified, however the microstructure of the powder form of these compositions has not been studied. This paper aims to understand the commercial Al 6061 powder: how the internal microstructure of the powder differs from wrought both in the as-manufactured and thermally treated conditions. A specific focus is put on the Mg-rich phases and their morphologies. This was accomplished through transmission electron microscopy (TEM), scanning transmission electron microscopy (STEM), and energy dispersive x-ray spectroscopy (EDS). Both size and morphology of the phases in the powder differ greatly from those in wrought.
- Phase Identification of Fe Phases in Al 6061 Powder
    - Gas atomized powders are frequently used in metal additive manufacturing processes (MAM). During consolidation, properties and microstructural features of the feedstock can be retained. Al 6061 is a heat treatable alloy that is commonly available in powder form. Features of interest being retained are the secondary phases that evolve during heat treatments. While heat treatments of 6061 have been widely studied in wrought form, little work has been done to study the process in powders. This work investigates the evolution of the Fe-containing precipitates in gas atomized Al 6061 powder through the use of transmission electron microscopy (TEM) and energy dispersive x-ray spectroscopy (EDS). The as-atomized powders contained $Al_{13}Fe_4$ at the boundaries. After thermal treatment at 530 °C for one hour, the $Al_{13}Fe_4$ dissolves and $Al_9Fe_2Si_2$ forms.
- Phase Transformations in Al 7075 Powder
    - Al 7075 is a heat treatable Al-Mg-Zn alloy widely used in the aerospace industry. Recently, it has found application as feedstock for metal additive manufacturing (MAM) techniques. It has been shown that wrought alloy compositions in powder form differ greatly in microstructure and properties from their conventional form. Given this, it is important to understand the internal microstructure of the powders prior to use in MAM processes.
    - This work studies the as-atomized condition of gas-atomized Al 7075 powders, as well as the effect of thermal treatments on the microstructure and secondary phases. Extensive electron microscopy revealed the presence of T-Phase, Al_7Cu_2Fe, and Mg_2Si in the as-atomized condition of this gas-atomized Al 7075 powder. Thermal treatments were performed at 465 °C and 480 °C with the goal of homogenizing the microstructure – dissolving T-phase while avoiding S-phase

growth, avoiding Al_7Cu_2Fe coarsening, and avoiding melting. In the samples treated at 465 °C, S-phase was unexpectedly present. In both 465 °C and 480 °C treatments, the T-phase was not fully dissolved after the 60 minute treatment. Guided by the thermodynamic modeling, these results indicate a shift in local equilibria in these powders.

- Phase Transformations in Al 5056 Powder
    - Aluminum 5056 is a work-hardenable alloy known for its corrosion resistance and has applications in additive manufacturing. Understanding the secondary phases in Al 5056 powders is important for understanding the properties of the final parts. Through extensive TEM, STEM, and EDS, magnesium segregation, β-Al_3Mg_2, Mg_2Si, and $Al_{13}Fe_4$ were identified in the as-atomized condition. After thermal treatment, the magnesium segregation and β-Al_3Mg_2 dissolved, while $Al_{13}Fe_4$ and Mg_2Si coarsened. Additionally, β-Al_3Mg_2 and an AlCr phase precipitated after natural aging. This speaks to the shelf-life of these powders and the importance of proper treatment and storage to maintain consistent results.
- Modeling Dissolution and Growth of Secondary Phases
    - Computational modeling can be used for gain insight into the phase transformations present in metallic systems during thermal processing. In this work, two aluminum powders Aluminum alloy 6061 and 5056 powders were used to study the phase transformations between the as-atomized condition and the thermally treated condition using a typical solutionization heat treatment. The diffusion module of the thermodynamic and kinetic software Thermo-Calc, called DICTRA can be used to model both the growth and dissolution of secondary phases within metallic alloy systems. Additionally, Thermo-Calc's PRISMA software can also be used to model the precipitation in the system. Using the identified phases in the alloy powder from previous work, the growth of the AlFe intermetallic $Al_{13}Fe_4$ and the dissolution of Mg_2Si were modeled to gain a greater understanding of the phase transformations as a function of thermal treatment in Al 6061 powder. Additionally, hot stage TEM was conducted in Al 5056 powder to understand phase transformations in the system. The data from this experiment was then used as a starting point for DICTRA models for the growth of $Al_{13}Fe_4$ and the dissolution of Al_3Mg_2 (Beta).

12 Future Work

Additional Hot-stage TEM will be used to unveil the phase transformations seen during thermal processing of the aluminum alloy powders. This technique will follow the thermal treatments used in the papers in Chapters 5-9 but allow for further understanding of the exact transformations during heating. This will be conducted for all 4 alloys, 2024, 7075, 6061, and 5056, starting with work already underway on 5056. The data extracted from these hot stage TEM videos will be employed in the diffusion module of the Thermo-Calc software, DICTRA, to calibrate the model described in Chapter 10. The Scheil solidification and Equilibrium diagrams will continue to be used as a guide to understand the phase stabilities to guide the hot-stage TEM experiments. Additional work will also be done on the process of extracting data from the hot stage TEM images. Image thresholding can be a very subjective process, so automation of this extraction would help to eliminate this subjectivity.

Additional work will be done using the DICTRA models calibrated with experimental work on the influence of furnace or fluidized bed temperature on the internal microstructure of the aluminum alloy powders. This work will be useful for understanding the scale up process. Current work has been done by thermally treating the aluminum powders using a DSC, which has exceptional temperature control, allowing thermal treatments to be accurate within a few °C. When thermal treatments are carried out in a furnace or fluidized bed, the temperature can fluctuate up to 100°C during treatment. This could potentially have major effects on the internal microstructure of the powder given the phase stabilities, and this internal effect could greatly influence the properties of the consolidated parts. Understanding this influence of temperature change will help to ensure that when the process is scaled up, the microstructure can still be controlled for the best consolidated cold spray properties.

13 Impact and Contribution

As mentioned in many chapters in the paper, little work has been done to understand the internal microstructure of metallic powder particles. Previously, this was due to the fact that the processes that used metallic feedstock powder, melted that powder, which seemed to deem the internal microstructure of the initial powder irrelevant. Since the creation of solid state additive processes, much work has focused on the process itself, and the final product outputs, but still little work has been done to understand the solid materials that directly correlate to the material properties of the final parts.

This work has begun to fill in the gaps of understanding feedstock powder microstructure for future correlation with properties of the consolidated additively manufactured parts. Since microstructural features are retained upon consolidation, this new feedstock understanding can help to optimize the feedstock through thermal treatments to obtain the best consolidated part properties.

The use of Thermo-Calc models and DICTRA has helped to gain additional insight into the phase transformations in these powders, which will help to reduce the number of experiments necessary to optimize powder microstructure and properties. Many thermal treatments can be selected and calculated using the experimentally calibrated models, and the final microstructure can be obtained.

This is pivotal for the use in the cold spray process, as ductile powders are needed in order to plastically deform to the substrate. This work gives insight into how to control the internal powder microstructure in order to create powders of that specification. This is drastically decrease trial and error for power thermal treatment in the cold spray industry and ensure that repairs and future part creation can happen in a much quicker manner.

The work with metallic feedstock powder for cold spray can also be extrapolated to other solid state additive manufacturing processes, such as Additive Friction Stir, or the many melting based additive manufacturing processes, including Powder Bed Fusion or Selective Laser Sintering. Since these processes also use metallic feedstock powder, this understanding of the powder microstructure can be used to make additional correlations to these processes. The microstructure will influence the final consolidated parts in solid state processes and in the melting processes since only partial melting is typically achieved. This would mean that many dispersoids phases such as the iron containing phases, or oxides present would not be melted during the process and would influence the final parts.

Overall, this work on understanding the internal microstructure in metallic powder feedstock will directly influence the use of cold spray techniques used by the Army and help to repair mechanical aerospace parts to decrease down time of vehicles, decrease cost or repair, and increase the safety overall of the soldiers in the field.